Spring 2023

Numerical Modeling of Flexible Structures in Open Ocean Environment

Alexander Knysh
University of New Hampshire, Durham

NUMERICAL MODELING OF FLEXIBLE STRUCTURES IN OPEN OCEAN ENVIRONMENT

by

ALEXANDER KNYSH

M.S. and B.S. in Theoretical and Applied Mechanics

Dnipro National University, Ukraine, 2017

DISSERTATION

Submitted to the University of New Hampshire

in Partial Fulfillment of

the Requirements for the Degree of

Doctor of Philosophy

in Mechanical Engineering

May, 2023

This dissertation was examined and approved in partial fulfillment of the requirements for the degree of Doctor of Philosophy in Mechanical Engineering by:

Dissertation Director, Igor Tsukrov
Professor of Mechanical and Ocean Engineering
University of New Hampshire

M. Robinson Swift
Professor Emeritus of Mechanical and Ocean Engineering
University of New Hampshire

David Fredriksson
Professor of Mechanical and Ocean Engineering
Director of the Center for Sustainable Seafood Systems
University of New Hampshire

Michael Chambers
Research Associate Professor
School of Marine Science and Ocean Engineering
Center for Sustainable Seafood Systems
New Hampshire Sea Grant

Andrew Drach
Doctor of Philosophy in Mechanical Engineering
Chief Executive Officer of Solwey Consulting

On 04/28/2023

Approval signatures are on file with the University of New Hampshire Graduate School.

Acknowledgements

I would like to express the deepest gratitude to my academic advisor and dissertation director Prof. Tsukrov for his patience and support during my graduate studies. The research presented in this dissertation would not have been possible without his professional guidance and expertise.

I am sincerely grateful to my committee members, M. Robinson Swift, David Fredriksson, Michael Chambers, and Andrew Drach, for their supervision and collaboration along my research path. Their attitude made my experience at the University of New Hampshire enjoyable and pleasant.

I want to thank my family and friends for their unconditional support in good and in bad times. I am truly blessed to have such wonderful people in my life.

The research presented in Chapter I was led by Prof. Swift and Prof. Chambers, and was supported by the Saltonstall Kennedy grant NA17NMF4270207 from National Oceanic and Atmospheric Administration. I thank Arron Jones and Erich Berghahn from New Hampshire Sea Grant for their assistance with collecting data from the mussel farm.

The research presented in Chapter II was led by Prof. Fredriksson and was funded by the United States National Science Foundation project 13355457, ARPA-E Interagency Agreement 89703018SAR000002, and ARPA-E project DE-AR0000917. I would like to express our sincere thanks to Prof. Fredriksson's former students at the United States Naval Academy along with the professional staff of the Hydromechanics Laboratory for acquiring physical model datasets.

The research presented in Chapter III was led by Dr. Drach and was funded by the United States Department of Energy's ARPA-E program, award DE-AR0000923. The funding was also obtained from the ARPA-E interagency agreement with the United States Naval Academy 89703018SAR000002 and project award DE-AR0000917 with the University of New England.

The research presented in Chapter IV was led by Dr. DeCew and was supported by the New Hampshire Innovation Research Center. Participation of Michael Osienski, Tom Sherwin, and Eric Rines from HALO Maritime Defense Systems in the field studies is greatly appreciated.

Table of contents

Abstract

The dissertation presents advancements in numerical modeling of offshore aquaculture and harbor protection structures in the open ocean environment. The advancements were implemented in the finite element software *Hydro-FE* that expands the Morison equation approach previously incorporated in *Aqua-FE* software developed at the University of New Hampshire.

The concept of equivalent dropper was introduced and validated on the example of a typical mussel longline design. Parametric studies for mussel dropper drag coefficients and bending stiffness contributions were performed for different environmental conditions.

To model kelp aggregates in macroalgae aquaculture, a corresponding numerical technique was developed. The technique proposes a modified Morison-type approach calibrated in full-scale physical tow tank experiments conducted at Hydromechanics Laboratory of the United States Naval Academy.

In addition to the numerical modeling techniques, an advanced methodology for multidimensional approximation of the current velocity fields around offshore installations was proposed. The methodology was applied to model a response of a kelp farm by utilizing tidal-driven acoustic Doppler current profiler measurements.

Finally, a numerical model of a floating protective barrier was built in the *Hydro-FE* software to evaluate its seaworthiness. The model was validated by comparison to measurements obtained in scaled physical wave tank tests and field deployments.

Introduction

Flexible marine structures are utilized in a variety of different industries including offshore aquaculture, marine renewable energy, oil and gas, harbor protection, etc. Aquaculture is of special interest in this context since it has been one of the fastest growing food industries in the world over the past decades (Gentry et al., 2017). To satisfy an increasing consumer demand in shellfish, seaweed, and other aquaculture products, the production needs to expand to more exposed sites that can safely maintain both ecological and economical approaches (Fairbanks, 2016). However, the expansion introduces a unique challenge of substantial variations and intensity of environmental conditions. The variations are especially important for large-scale extractive specie aquaculture installations, such as mussel longlines and kelp farms, due to considerable drag exerted on these structures in high-energy environments. The same challenge is observed in other ocean engineering applications, such as harbor protection installations, where environmental conditions can also significantly vary. Thus, enhanced, efficient, and reliable numerical modeling techniques are required to validate or design the components of these installations, and to accurately predict structural performance.

This dissertation presents advancements in numerical modeling of structures deployed in exposed ocean environments, particularly aquaculture and harbor protection installations. The advancements were incorporated and tested in the nonlinear, dynamic, finite element software *Hydro-FE* that expands the empirical Morison equation approach previously implemented in *Aqua-FE* software developed at the University of New Hampshire (Gosz et al., 1996; Tsukrov et al., 2000; Fredriksson et al., 2003). Hydro-FE is integrated as a set of user-defined subroutines into a commercial, general-purpose software Marc, and is used to calculate forces and the dynamic

response of structures in marine environments (Knysh et al., 2021; Knysh et al., 2022). The solver incorporates an updated Lagrangian formulation to account for large displacements, rotations and strains of structural elements. Unlike other fluid-structure interaction solvers, such as coupled finite element and smoothed particle methods (Jiang et al., 2017), Hydro-FE does not solve a fluid dynamics problem (also known as one-way coupling), so fluid flow alterations due to presence of structures are either neglected or investigated through a separate fluid dynamics analysis. The dissertation presents numerical modeling of typical marine structures and their components in Hydro-FE (Knysh et al., 2020; Knysh et al., 2021) with advanced hydrodynamic inputs (Knysh et al., 2022), and is divided into four chapters.

The first chapter is dedicated to numerical modeling of submerged mussel longlines (Danioux et al., 2000; Buck, 2007; Cheney et al., 2010; Buck and Langan, 2017) with mussel droppers attached to the longline and surrounded by protective sleeves. The purpose of this study was to evaluate several single longline and dropper sleeve designs, and to estimate the influence of the design modifications on the overall structural response. Finite element analysis was applied to predict the dynamic response of the mussel longlines to typical and extreme North Atlantic environmental conditions implemented using Airy wave theory (Dean and Dalrymple, 1991). The equivalent dropper model was developed and utilized to improve computational performance of finite element models. A set of parametric studies were performed to evaluate sensitivity of the results to the mussel droppers' drug coefficients and bending stiffness.

The second chapter presents numerical modeling of kelp aggregates densely grown on cultivation lines (Kim et al., 2015; Augyte et al., 2017). The objective of this study was to propose a finite element model representation of the compliant (Buck and Buchholz, 2005; Henry, 2014; Rominger and Nepf, 2014) and almost neutrally buoyant (Vettori and Nikora, 2017) aggregates for

applications in a hydrodynamic-structural, time-domain modeling of seaweed aquaculture systems. The proposed finite element model replicated the tow tank tests of the full-scale physical model of a kelp aggregate conducted at the United States Naval Academy (Fredriksson et al., 2020), and was built using measurements of kelp blade length and width, number of blades, and material mass density. The finite element model is based on the Morison-type equation with the hydrodynamic coefficients determined from the tow tests. The tow tests were replicated in the finite element simulations to verify the balance of hydrostatic, hydrodynamic, and internal forces for the aggregate.

The third chapter is focused on methodology for approximation of current velocity fields around large-scale aquaculture installations. The purpose of the study was to propose a smooth and accurate multidimensional approximation technique based on discrete current velocity data sets, such as acoustic Doppler current profiler measurements. The approach implies presenting the continuous current velocity function as a superposition of weighted radial basis functions extended by a linear polynomial (Holmström, 2008). To address potential overfitting issues (Smith et al., 1998), the thin plate regularization was applied in the method. The approximation was also constrained to fit the velocity values on the domain boundaries. The simulations of the kelp farm deployment at University of New England Wood Island site, Maine, USA, were performed for the proposed technique as well as for other current approximation techniques utilized in practice.

The fourth chapter describes numerical modeling of floating protection barriers used for protection of critical governmental, commercial, and private assets from water-borne intrusions. The objective of this study was to present a comprehensive approach to the prediction and evaluation of the floating barriers offshore performance on the example of a *Triton* barrier manufactured by HALO Maritime Defense Systems. The approach includes a combination of full-

scale field studies, scaled physical testing and numerical modeling. The four-month-long field deployment of the barrier was performed near the Isles of Shoals, New Hampshire, USA. The scaled physical testing was conducted in the University of New Hampshire wave tank utilizing techniques previously developed and validated for various offshore aquaculture installations (Fredriksson et al., 2000; DeCew et al., 2005; Wang et al., 2015). The numerical modeling was performed with the finite element software *Hydro-FE* extensively applied in the marine aquaculture field (DeCew et al., 2010; Wang et al., 2015; Knysh et al., 2020). Evaluation of seaworthiness of the barrier was conducted through comparisons between field deployment, physical tests, and corresponding numerical simulation results.

Chapter I

Numerical modeling of submerged mussel longlines with protective sleeves

This chapter was published as *Knysh, A., Tsukrov, I., Chambers, M., Swift, M.R., Sullivan, C. and Drach, A., 2020. Numerical modeling of submerged mussel longlines with protective sleeves. Aquacultural Engineering, 88, p.102027.*

My contribution to the paper was development of the equivalent dropper concept, and performing numerical modeling of the proposed mussel longlines designs. I conducted numerical sensitivity studies for drag coefficients and bending stiffness of the droppers. I also participated in the mechanical tests of the droppers with different protective sleeve types, and prepared the first draft of the manuscript for publication.

Abstract

Farmers growing mussels in offshore environments have turned to submerged longline farming as a relatively safe, reliable and profitable way to produce mussels in the exposed ocean environment. However, variations in the environmental conditions (strong currents and storms) and potential presence of predator species (e.g. eider ducks) require robust engineering approaches to design longline mussel farms and their components.

This paper describes application of a mechanistic fluid-structure interaction modeling software *Hydro-FE* to predict the dynamic response of several mooring/longline/dropper configurations subjected to typical and extreme environmental conditions of a North Atlantic mussel farming site. *Hydro-FE* is a software tool that expands and modernizes the approach previously implemented in the finite element program *Aqua-FE* developed at the University of New Hampshire to analyze flexible structures in marine environment. The numerical model takes into account smooth variation of the hydrodynamic forces around the free surface (continuous partial submergence), Reynolds number dependence of drag coefficients of mooring lines and includes contributions of predator-protection sleeves to the overall mechanical response of mussel droppers. The simulations provide estimates of anchor forces, mooring line tensions, and time-series data on the motion of the droppers. This information can be used in the design of mussel longlines to prevent anchor failure, rope breakage, line entanglement and mussel fall-off.

Keywords: mussel longline; finite element analysis; fluid-structure interaction; equivalent mussel dropper.

1. Introduction

The aquaculture industry has been continuously expanding to more and more exposed locations worldwide. In particular, mussel farming is becoming popular for nearshore and offshore sites in the United States, Canada and New Zealand. Despite the numerous environmental, economic and jurisdictional difficulties, submerged mussel longline farming turned out to be safe, reliable, profitable and sometimes the only possible way to produce mussels in large quantities

(Langan, 2013). Moreover, the submerged longline design (schematically illustrated in Fig. 1.1) is considered to be superior in terms of expanding to the open ocean environment (Danioux et al., 2000; Buck, 2007; Cheney et al., 2010; Buck and Langan, 2017).

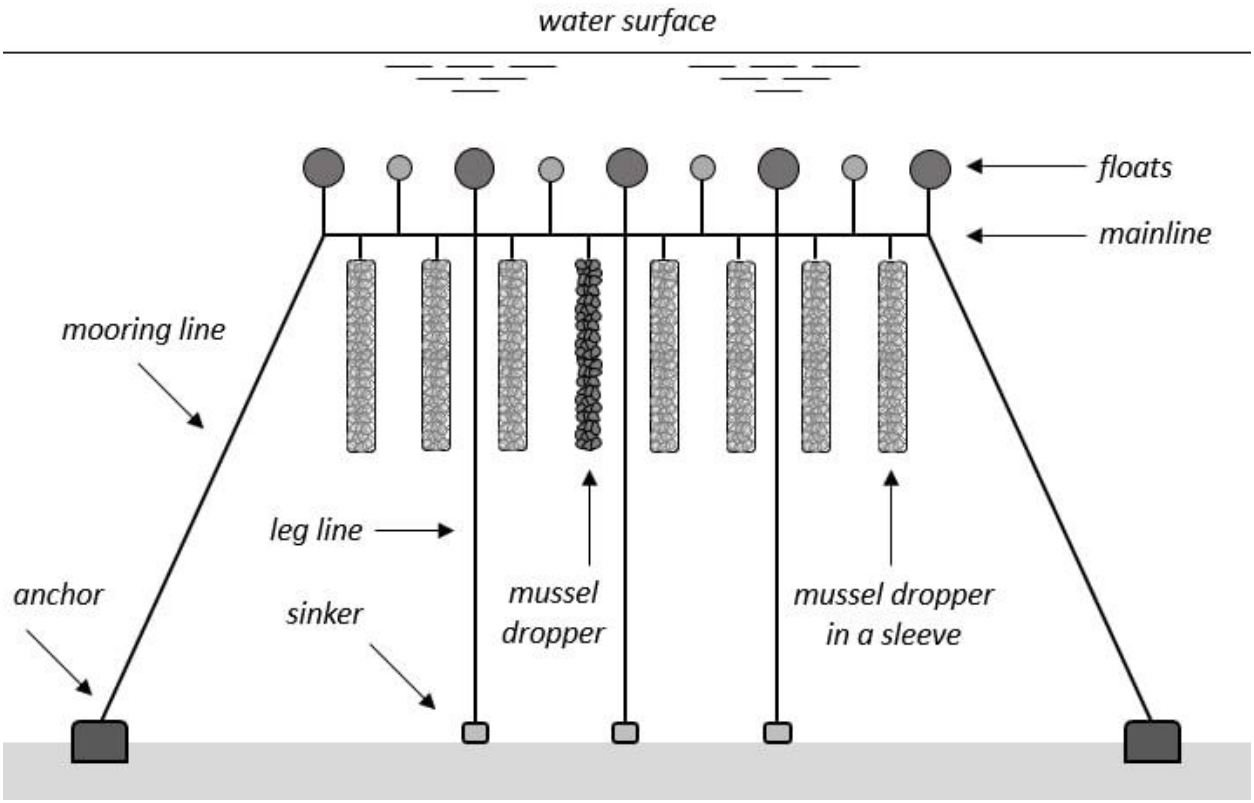

Figure 1.1. Profile view of an example of a fully submerged mussel longline with protective sleeves surrounding mussel droppers.

Mussel longlines have been investigated through field observations, scaled physical testing and numerical modeling. There are several valuable observational studies that describe multiday monitoring of the hydrodynamics, loading and motion of mussel longlines in the exposed environment (Stevens et al., 2007; Lin et al., 2016; Gagnon and Bergeron, 2017). Scaled physical experiments in a tank are also important to understand the fluid drag behavior of mussel crop lines

as well as implications of such effects as mussel bio-pumping (Plew et al., 2009; Landmann et al., 2019). Dynamic models of mussel longlines represented by an assemblage of lumped masses connected by springs have been successfully utilized in Raman-Nair and Colbourne, 2003; Raman-Nair et al., 2008. Note that the hydrodynamic behavior and structural performance of mussel longlines with protective sleeves are similar to other longline culture systems, such as oysters or scallops, with lantern nets. The examples of numerical and physical modeling of such systems are provided in López et al., 2017; Zhao et al., 2019, with a comprehensive literature review on the topic found in Zhao et al., 2019.

In this paper, finite element analysis in applied to evaluate a set of simple one-line designs of submerged mussel growing installation. There are several finite element modeling software packages available to analyze flexible aquaculture structures in marine environment. Commercially available programs, *OrcaFlex* and *ProteusDS*, provide robust user interface and strong validation background for various ocean engineering applications. The finite element software package *AquaSim* was developed specifically for net modeling and aquaculture applications (Berstad et al., 2012; Berstad and Heimstad, 2019). The fish cage aquaculture farm modeling programs developed at Dalian University of Technology (Li et al., 2006; Zhao et al., 2007, 2015), SINTEF Fisheries and Aquaculture (Reite et al., 2014; Tsarau and Kristiansen, 2019) and Pukyong National University (Lee et al., 2008, 2015) are based on a lumped-mass representation and a direct dynamic modeling approach.

The software package used in the present paper, *Hydro-FE*, is based on the well-validated *Aqua-FE* software developed at the University of New Hampshire (Gosz et al., 1996; Tsukrov et al., 2000; Fredriksson et al., 2003). The purpose of this study is to evaluate several simple longline and dropper sleeve designs, and to estimate the influence of the design modifications on the overall

structural response. Environmental conditions include current and waves which are implemented using Airy wave theory (Dean and Dalrymple, 1991). Hydrodynamic forcing on mooring lines is calculated with Reynolds number dependent drag coefficients (Choo and Casarella, 1971; DeCew et al., 2010). The equivalent dropper model is developed and utilized to improve computational performance. A set of parametric studies is performed to evaluate sensitivity of the results to the mussel droppers' drug coefficients and bending stiffness.

The rest of the paper is organized as follows. Section 2 describes the designs of the considered mussel farms and the properties of the droppers as defined by their mussel protection sleeves. The concept of an equivalent mussel dropper used in the numerical modeling is introduced in Section 3. The section also includes description of the finite element models of all four considered designs. Section 4 provides the environmental conditions of the mussel farming site and the available data on the dropper drag coefficients. The results of numerical simulations including the parametric studies for drag coefficient and bending stiffness contributions are presented in Section 5.

2. Mussel farm design

2.1 Mussel longlines

Most modern mussel longline farms consist of rows of vertical droppers hanging from mainlines which are supported by a set of floats and fixed by mooring lines (Drapeau et al., 2006; Buck, 2007; Karayücel et al., 2015). Sometimes, vertical legs with sinkers and floats are also added for dynamic stability (Gagnon and Bergeron, 2017). The dropper itself consists of a polyester core rope with an outer layer of fibrous material that is conducive to mussel spat collection and

settlement. The mussels attach to the fibrous material as larvae and then attach to the inner core rope as they grow. The mussels are sometimes enclosed into a meshed sleeve to protect them from various predators, such as diving eider ducks. These sleeves can affect the mussel growth and the resulting mechanical properties of the droppers.

In this study, the performance of a fully submerged longline with 80 droppers uniformly distributed along the mainline (as shown in Fig. 1.2) was investigated by direct numerical modeling. This particular configuration was utilized by Peter Flanigan and Vincent Prien from Isles of Shoals Mariculture, off the coast of Rye, New Hampshire, USA. The mainline was maintained in an approximately horizontal position by appropriately distributing $325\ N$ floats each (the number of floats varied from 21 to 53 depending on the droppers' linear density and mooring design). The longline was deployed in $33\ m$ depth, $11\ m$ below water surface. The length of the mainline was $73\ m$; the droppers were $3\ m$ long; the distance between the anchors was $152\ m$. More information on geometric and mechanical properties of the components is provided in Section 3.3.

Preliminary simulations showed that the design illustrated in Fig. 1.2 experienced excessive motion in extreme storm conditions as described in Section 5. In an attempt to better control the system dynamics, three modifications of the original 2-point mooring design were considered, as presented in Table 1.1. The first modification of the initial structure, "4-point mooring", has 2 anchors at each end (4 in all). Each anchor pair is spread out on the bottom along a line perpendicular to the mainline. The anchors are located $24\ m$ apart at the same distance of $152\ m$ from the opposite pair of anchors. The mooring lines converge to the end of the mainline forming an inverted "V". The second modification, "4-point mooring with weights" or "4-point mooring

[W]", includes an extra 38 kg ballast weight attached to the lower end of each dropper as well as an additional row of floats to compensate for it. Finally, the third modification, "4-point mooring with vertical legs" or "4-point mooring [VL]", is constrained with 3 additional leg lines: one is at the middle and two others are 20 m away from the corresponding ends of the mainline. A more detailed description of these modifications, including mechanical and geometrical properties of the components, is provided in Section 3.3.

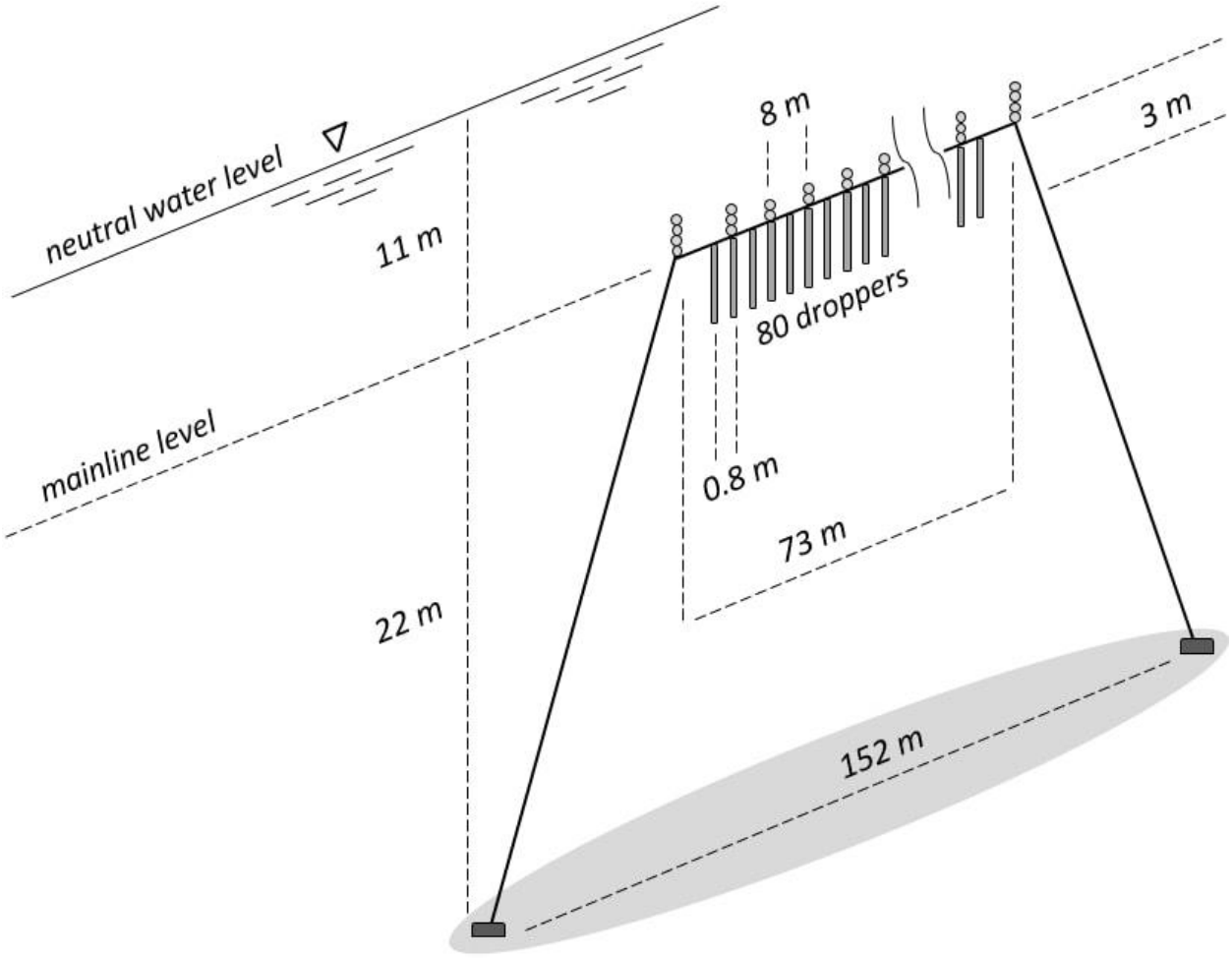

Figure 1.2. Isometric view of the mussel longline with two mooring lines.

Table 1.1. Variations of the longline design considered in this paper.

Design	Mooring lines	Vertical Leg lines	Additional weight
2-point mooring	2	0	No
4-point mooring	4	0	No
4-point mooring [W]	4	0	Yes
4-point mooring [VL]	4	3	No

2.2 Properties of mussel droppers with three types of protective sleeves

A research project initiated by National Oceanic and Atmospheric Administration and local mussel farming industry in 2017 aims to grow the offshore mussel industry in the Gulf of Maine by developing longline systems that can survive biological (eider predation) and physical (high wave energy) constrains. Its objectives are to evaluate new protective technologies and strategies that will allow to grow mussels without constriction and prevent diving ducks from preying upon shellfish during their seasonal migrations, and to transfer protective shellfish methods and relevant business planning information to new and existing farmers in New England.

Protective sleeves are not commonly used in the mussel longline farming but can protect shellfish droppers from various predators. Typical sleeves are made of plastic and installed in such a way as to fully cover the mussel droppers. Three types of protective sleeves made of low-density polyethylene and manufactured by Industrial Netting, USA have been tested with regards to their performance for mussel growing applications. They included NG 8060 Standard Duty yellow, NG3070 Vexar Work Grade blue and NG2090 Vexar Superduty green sleeves. The sleeves vary in

their rigidity and cell size. In the text to follow, mussel droppers with these sleeve types are referred to as *green*, *blue* and *yellow*, respectively. As an example, the structure of *green* dropper can be seen in Fig. 1.3c. There are also sleeves manufactured by Intramas Group, Spain that are currently in use but were not tested in this paper.

Measurements of the mechanical and geometric properties of the mussel droppers in these sleeves were taken on July 3, 2018 at the University of New Hampshire nearshore multi-trophic aquaculture site in the mouth of the Piscataqua River in New Castle, New Hampshire, USA, see Fig. 1.3a. The *green* dropper was first seeded in March 2017 with a secondary seeding occurring in October 2017, and the *blue* and *yellow* droppers were only seeded in October 2017. The protective meshes were also applied to the droppers at different times. The green and blue meshes were applied in November 2017, and the yellow mesh was applied in February 2018.

Presence of the protective sleeves and the different seeding dates affected the overall diameter, density and bending stiffness of each mussel dropper. The diameter for each dropper type was recorded as the average of three measurements $d_h = \frac{1}{3}\left(d_h^{(1)} + d_h^{(2)} + d_h^{(3)}\right)$. The linear density was calculated from the weight W of the suspended portion of the dropper l_w in the air $\omega_{air} = \frac{W}{g l_w}$. The bending stiffness was determined using a cantilever beam model by freely suspending a portion of a dropper ($l_b = 0.33\ m$) from a horizontal support, see Fig. 1.3b. The deflection δ of the free end due to self-weight was measured. Then, using the strength of materials formula for a cantilever beam under a uniformly distributed loading (Bansal, 2010), the dropper's bending stiffness EI was found as

$$EI = \frac{\omega_{air}\ g\ l_w^4}{8\ \delta} \tag{1.1}$$

where g is the gravity constant. It was determined that the bending stiffness of the *yellow* dropper was $0.79\ N \cdot m^2$, while the *blue* and *green* ones had negligible bending stiffness. The results of all measurements are summarized in Table 1.2.

Table 1.2. Field measurements and calculated parameters of droppers.

Sleeve type	**Twine thickness t $[cm]$**	**Mesh cell width r $[cm]$**	**Mesh cell height h $[cm]$**	**Diameter of dropper d_h $[m]$**	**Linear density ω_{air} $[kg/m]$**	**Bending stiffness EI $[N \cdot m^2]$**
Yellow	0.10	1.54	2.85	0.13	7.53	0.79
Blue	0.11	1.49	2.80	0.13	9.00	*negligible*
Green	0.13	1.42	2.71	0.25	17.71	*negligible*

Measurements conducted on July 3, 2018 correspond to the intermediate state of the mussel growing cycle. Previous studies reported the average values of a dropper diameter varying from $0.12\ m$ to $0.2\ m$ (Plew et al., 2005; Stevens et al., 2007; Cranford et al., 2014; Gagnon and Bergeron, 2017), depending on the environmental conditions, farm design, and mussel species. As mussels grow, the average diameter and weight of the dropper can increase by approximately 5-10% every 40 days of growth (Lauzon-Guay et al., 2006; Gagnon and Bergeron, 2017). Fig. 1.3c produced during the mussel farm inspection on May 9, 2019 illustrates the state of the *green* dropper when the sleeve is completely filled with mussels. Note that for numerical simulations presented in this paper, the geometrical and mechanical properties measured on July 3, 2018 are used. As the culture grows and the properties change, it has to be reflected in the input data of the model.

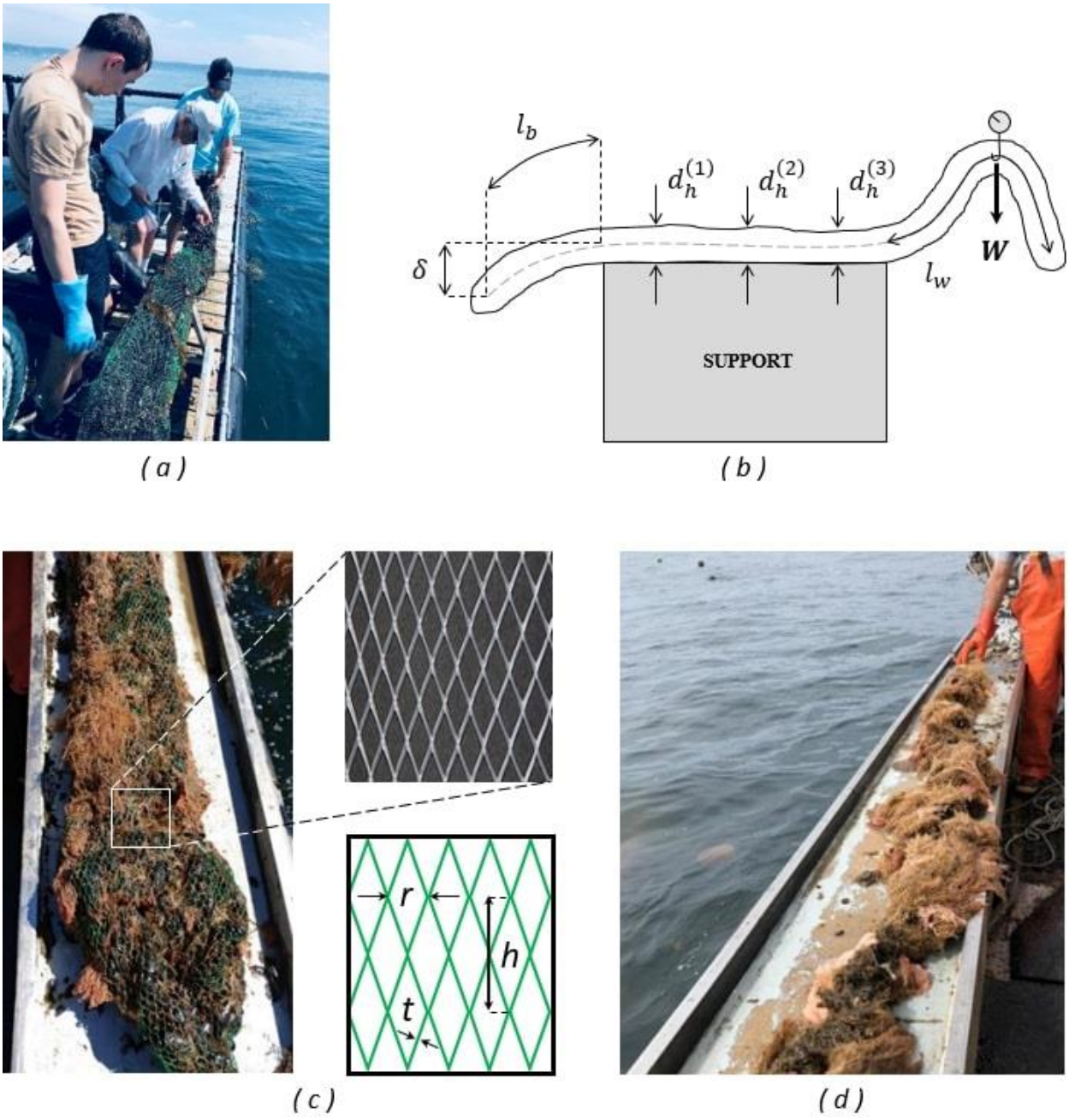

Figure 1.3. Inspection and measurements of the droppers' density and bending stiffness: *(a)* field measurements on July 3, 2018; *(b)* schematics of the measurements on July 3, 2018; *(c)* farm inspection on May 9, 2019 – mussels in *green* dropper; (d) farm inspection on July 24, 2019 – the control dropper without sleeve void of mussels and overgrown with tubularia.

During the regular farm inspections, it was observed that the presence of predator-protection sleeves provides surface area for biofouling organisms to attach. However, with the filter feeding mussels near the sleeve, biofouling attachment was minimized as shown in Fig. 1.3c compared to unprotected control droppers in Fig. 1.3d. The control dropper without the sleeve was void of mussels and overgrown with tubularia. Much less biofouling was observed on the *green* dropper filled with mussels (Fig. 1.3c). It appears that the filter feeders inside the net were able to consume the free floating hydroid larvae before they even settle. This situation is different from the lantern nets where large areas of the exposed netting material provide more surface for the tubularia to attach.

3. Concept of an equivalent dropper

The finite element discretization required for numerical modeling of longline farms with a large number of mussel droppers can lead to an excessive number of finite elements, resulting in unreasonable simulation time and costs. To simplify the numerical models without significant loss of accuracy, the concept of an "equivalent dropper" representing several actual droppers was utilized. This approach mimics the concept of "consistent net elements" described in Tsukrov et al., 2002. The equivalent dropper should have the same weight, buoyancy and hydrodynamic performance as several actual droppers. In this section, the required geometric and physical parameters of an actual mussel dropper are identified, and then an approach to selecting the equivalent dropper values is proposed. Note that since water permeates the dropper, the buoyancy force acting on the dropper of length L it will not be equal to $\pi\rho_w L d_h^2/4$, where ρ_w is the water

density and d_h is the diameter obtained from the measurements. To properly account for this effect, two separate diameters are introduced: the "hydrodynamic" diameter d_h, which is obtained from the measurements and used for estimating hydrodynamic forces, and the "structural" diameter d_s, which is calculated to represent the dropper's axial stiffness, mass and buoyancy.

3.1 Modeling of the actual mussel dropper

The simplest possible approach is to consider a dropper as a homogeneous flexible cylinder. In this case, its diameter and density can be determined from direct measurements (Fig. 1.3). For example, our field measurements of the *yellow* dropper resulted in a linear density in the air of $\omega_{air} = 7.53\ kg/m$ and an outer diameter of $d_h = 0.13\ m$.

However, mussel droppers are porous, so that the outer diameter d_h will not represent the amount of water displaced by the dropper. Thus, it cannot be used to evaluate buoyancy and inertia of the dropper in the water. One additional measurement is needed. If the linear density of the dropper measured in air is ω_{air} and the linear density of the submerged dropper is ω_{subm}, the buoyancy correction coefficient k can be introduced as $\omega_{subm} = k\ \omega_{air}$. Recent studies show that the buoyancy correction coefficient for a dropper with blue mussels is around 0.25 (Dewhurst, 2016). Then, based on Archimedes' principle, the average density of the dropper material is defined by:

$$\rho_d = \frac{\rho_w}{1-k} \tag{1.2}$$

In this case, the mass of the dropper will be $\rho_d V_{dropper} = \rho_d(\pi\ L\ d_s^2)/4$ which results in the following estimate of the structural diameter:

$$d_s = \sqrt{\frac{4\,\omega_{air}}{\pi\,\rho_d}} \tag{1.3}$$

where d_s can be used to calculate the overall weight and buoyancy of the dropper, while d_h is used for hydrodynamic forces. The abovementioned distinction is implemented in *Hydro-FE* by introducing a buoyancy adjustment multiplier $k_b = d_s^2/d_h^2$ as a ratio of nominal and actual volumes of the mussels in the dropper.

3.2 Equivalent mussel dropper

Consider one equivalent mussel dropper which represents N actual ones, and has the same average density ρ_d and length L. To keep the total droppers' mass, the linear density of the equivalent dropper should be $\widetilde{\omega}_{air} = N\omega_{air}$. Applying (1.3) to the equivalent dropper, the equivalent structural diameter becomes

$$\tilde{d}_s = \sqrt{\frac{4\,\widetilde{\omega}_{air}}{\pi\,\rho_d}} = \sqrt{N}\,d_s \tag{1.4}$$

The hydrodynamic diameter of an equivalent dropper, $\tilde{d}_h$, is chosen to represent the total drag and inertia forces exerted on N actual droppers. In order to calculate this force, the Morison equation approach (Morison et al., 1950), expanded to the case of a moving cylinder (Goodman and Breslin, 1976) is used. Consider a submerged equivalent dropper of diameter $\tilde{d}_h$ arbitrarily moving in the water (Fig. 1.4) and subdivided into differential sections dL. There are two vectors associated with each of those sections: the local fluid velocity vector $\boldsymbol{u}$ and the body velocity vector $\boldsymbol{v}$. Both of these vectors can be projected on tangential (parallel to the cylinder axis) and normal

(perpendicular to the cylinder axis) directions. Then, the normal projection of the force exerted on a differential section dL is

$$d\widetilde{\boldsymbol{F}}_n = \rho_w \frac{\partial \boldsymbol{u}_n}{\partial t} d\tilde{V} + C_a \rho_w \left(\frac{\partial \boldsymbol{u}_n}{\partial t} - \frac{\partial \boldsymbol{v}_n}{\partial t} \right) d\tilde{V} + \frac{1}{2} C_d \rho_w |\boldsymbol{u}_n - \boldsymbol{v}_n| (\boldsymbol{u}_n - \boldsymbol{v}_n) d\tilde{A} \tag{1.5}$$

where $\boldsymbol{u}_n$ and $\boldsymbol{v}_n$ are the normal projections of fluid and body velocities associated with section dL, C_a is the added mass coefficient, C_d is the normal drag coefficient, $d\tilde{V}$ and $d\tilde{A}$ are the equivalent differential volume and the normal projected area of section dL. The tangential component of the drag force is taken in the form:

$$d\widetilde{\boldsymbol{F}}_t = \frac{\pi}{2} C_t \rho_w |\boldsymbol{u}_t - \boldsymbol{v}_t| (\boldsymbol{u}_t - \boldsymbol{v}_t) d\tilde{A} \tag{1.6}$$

where C_t is the tangential drag coefficient, $\boldsymbol{u}_t$ and $\boldsymbol{v}_t$ are the tangential projections of fluid and body velocities associated with section dL. The differential volume and the normal projected area are calculated as

$$\begin{gathered} d\tilde{V} = \tilde{S} dL = \frac{1}{4} \pi \tilde{d}_h^2 dL \\ d\tilde{A} = \tilde{d}_h dL \end{gathered} \tag{1.7}$$

Formulas (1.5) and (1.6) show that the normal component of the total hydrodynamic force acting on the equivalent dropper depends on both the equivalent volume and the equivalent projected area, while the tangential component depends on the entire side area $\pi d\tilde{A}$. It is not possible to pick such a value of $\tilde{d}_h$ that $\widetilde{\boldsymbol{F}}_n = N\boldsymbol{F}_n$ and $\widetilde{\boldsymbol{F}}_t = N\boldsymbol{F}_t$ since $d\tilde{V}$ and $d\tilde{A}$ depend on the equivalent diameter quadratically and linearly, respectively. The described contradiction is resolved by determining $\tilde{d}_h$ from the equality of the equivalent and actual droppers' volumes

$d\tilde{V} = NdV$, and then introducing the drag adjustment multiplier k_d, that equalizes the equivalent and actual projected areas $k_d d\tilde{A} = NdA$:

$$\tilde{d}_h = \sqrt{N} d_h$$
$$k_d = \sqrt{N} \tag{1.8}$$

The drag adjustment multiplier k_d is implemented as a parameter in *Hydro-FE* software. Note that the buoyancy adjustment multiplier for the equivalent dropper expressed similarly as for the actual dropper $k_b = \tilde{d}_s^2 / \tilde{d}_h^2$.

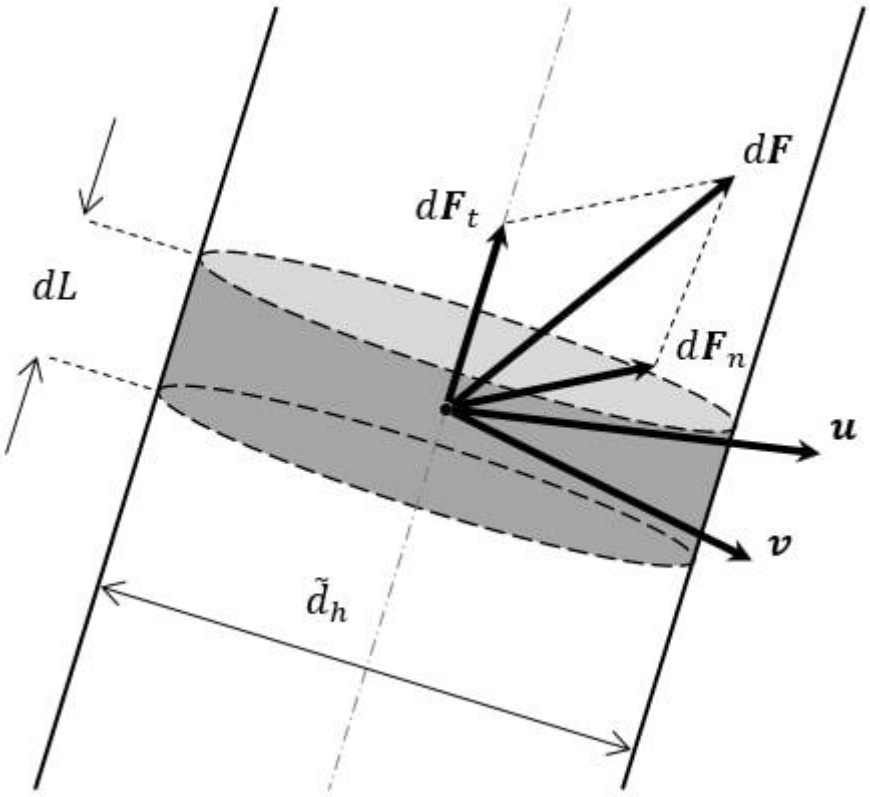

Figure 1.4. Moving equivalent dropper in a time-dependent water flow; direction t is along the cylinder, plane n is perpendicular to it.

The bending stiffness of the equivalent dropper is prescribed to have the same horizontal deflection Δ of the lower end as for the actual dropper when fixed at the upper end and subjected to the same horizontal current, see Fig. 1.5. This deflection is proportional to the distributed loading, exerted on the dropper by the fluid, which is proportional to the projected area of the dropper since the first two terms in right-hand side of (1.5) are zeroes. With the actual and equivalent areas being related as $d\tilde{A} = \sqrt{N}dA$, we obtain:

$$\widetilde{EI} = \sqrt{N}\, EI \tag{1.9}$$

The concept of the equivalent dropper approach is validated in Section 5.1.

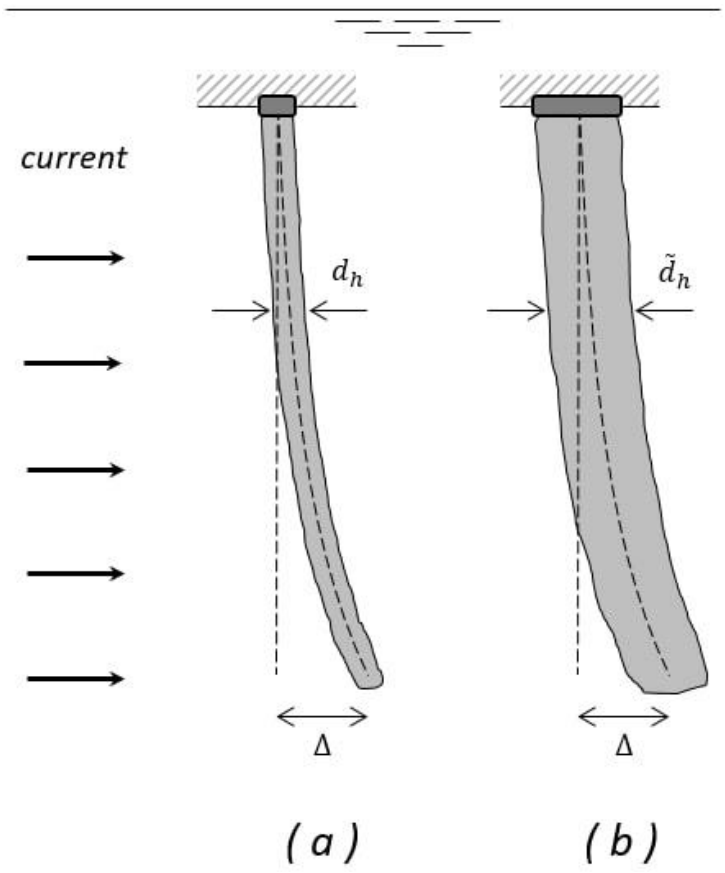

Figure 1.5. Deflection of *(a)* actual and *(b)* equivalent dropper under a uniform current loading.

3.3 Finite element models of mussel longlines

In this study, the longline system is numerically investigated via finite element simulations. Finite element models were built for all design variations presented in Table 1.1. However, direct modeling of 80 droppers would make the finite element model computationally inefficient due to a high number of finite elements associated with the droppers. For this reason, every 10 droppers in the longline models are represented by an equivalent one, according to the equivalent dropper concept described in Section 3.2. There are four structural components present in the designs: ropes, equivalent droppers, floats and weights (for the weighted configuration only). The mechanical and geometric properties of these components are provided in Table 1.3. Note that the bending stiffness of the droppers is found from the experiments described in Section 2 independently from the axial Young's modulus presented in Table 1.3. The values of the Young's modulus for floats and weights have been selected to be much higher than other structural components as they are stiffer and don't significantly influence the overall dynamic response.

In the considered designs, the number of float elements depends on the dropper type because *yellow*, *blue* and *green* droppers have different mass and, as a result, require specific number of floats to be properly supported (one float is always represented by one finite element). The designs also differ in the number of elements related to the rope and weight (Table 1.4).

Schematics of the finite element models are shown in Fig. 1.6. Going from design *(a)* to design *(b1)* adds 2 additional mooring lines or 40 elements; from *(b1)* to *(b2)* – adds 8 weights, 9 floats and 9 ropes to connect floats or 26 elements; from *(b2)* to *(c)* – adds 3 legs, removes 2 floats and 8 weights or additional 45 elements in total.

Table 1.3. Mechanical and geometric properties the mussel longline structural components used in the finite element model.

Structural component	**Density** $[kg/m^3]$	**Young's modulus** $[GPa]$	**Diameter** $[m]$	**Element type**
Rope	930	0.69	0.025	2-node, 3-d, truss
Equivalent dropper *yellow / blue / green*	1366	0.1	*0.26 / 0.29 / 0.40*	2-node, 3-d, *beam / truss / truss*
Float	37	1	0.32	2-node, 3-d, truss
Weight	8050	100	0.17	2-node, 3-d, truss

Table 1.4. Number of finite elements used for each structural component of the mussel longline designs

Structural component	**2-point mooring**	**4-point mooring**	**4-point mooring [W]**	**4-point mooring [VL]**
Rope	154	194	203	258
Equivalent dropper	80	80	80	80
Float *yellow / blue / green*	*21 / 24 / 44*	*21 / 24 / 44*	*30 / 33 / 53*	*28 / 31 / 51*
Weight	-	-	8	-
Total number of elements	*255 / 258 / 278*	*295 / 298 / 318*	*321 / 324 / 344*	*366 / 369 / 389*

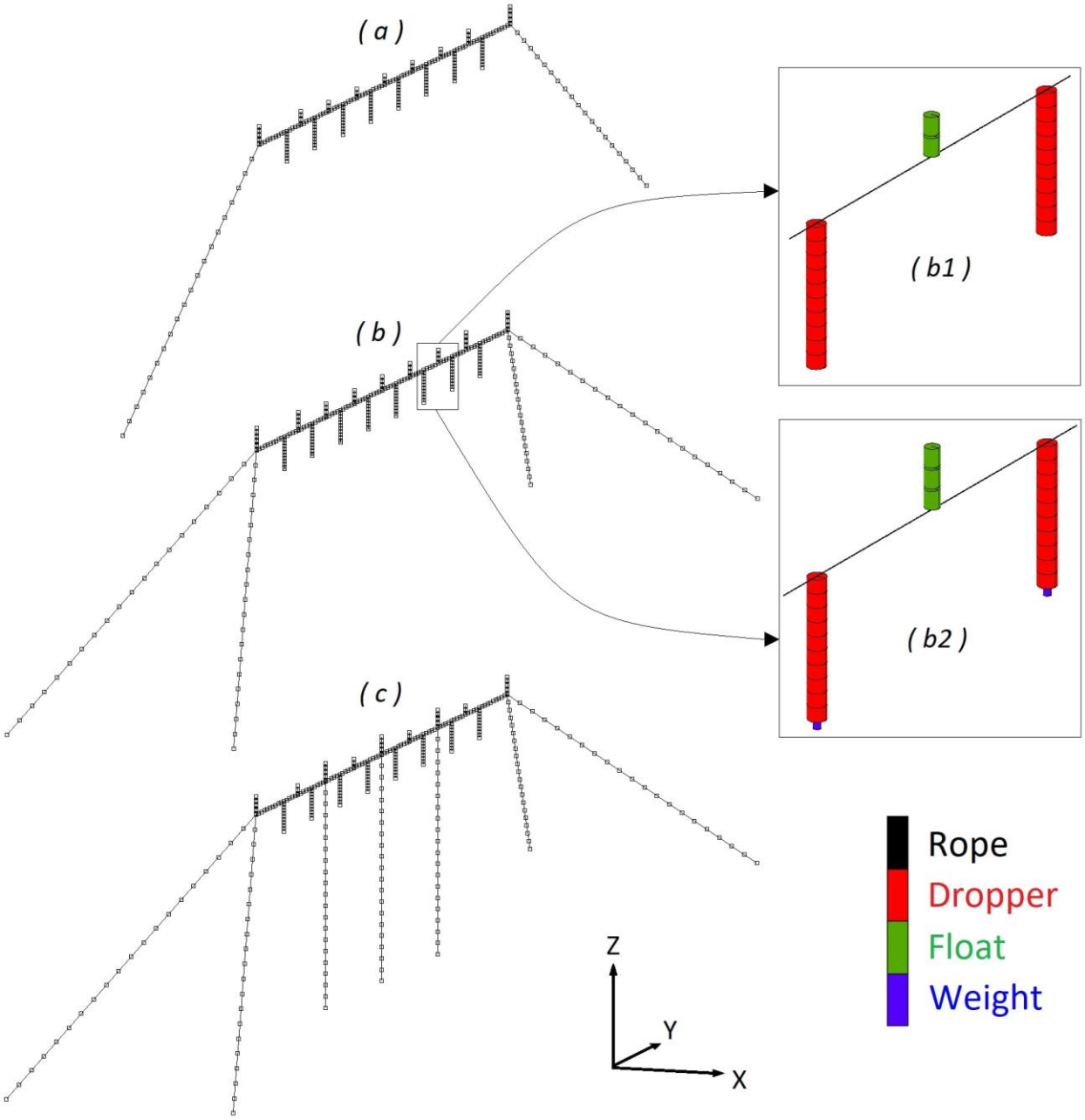

Figure 1.6. Finite element models of longlines with equivalent droppers:
(a) 2-point mooring design; *(b, b1)* 4-point mooring design;
(b, b2) 4-point mooring [W] design; *(c)* 4-point mooring [VL] design.

4. Environmental conditions and drag coefficients

4.1 Environmental conditions

There are two representative North Atlantic mussel farming site weather conditions considered in the study: fair weather and storm. Both of them are characterized by a current velocity and monochromatic wave properties shown in Table 1.5. Note that the wave length L was found using the dispersion equation of linear wave theory (Dean and Dalrymple, 1991)

$$\sigma^2 = gk\ tanh(kh) \tag{1.10}$$

where $\sigma = 2\pi/T$ is the wave frequency, $k = 2\pi/L$ is the wave number, T is the wave period, h is the depth of water. The current velocity and wave propagation vectors were assumed to be collinear. In this study, random waves were not considered. The case of monochromatic waves collinear with the current and perpendicular to the longline was the extreme case chosen because the difference in hydrodynamic behavior of different designs is more pronounced for such a loadcase.

Table 1.5. Current and wave properties of characteristic environmental conditions.

Weather	**Current velocity** $[m/s]$	**Wave height** $[m]$	**Wave period** $[s]$	**Wave length** $[m]$
Fair	0.15	1	4	25
Storm	0.15	5	8.8	114.9

4.2 Drag coefficients

In most of the published numerical studies, mussel droppers are modeled as rigid or flexible cylinders, see, for example (Raman-Nair and Colbourne, 2003; Plew, 2005; Cranford et al., 2014). Hydrodynamic forces on these cylinders are usually described by the Morison equation (1.5) with the values of normal drag and added mass coefficients taken either from experimental data or based on the assumption of a smooth cylinder (Hoerner, 1965). Sometimes, normal drag coefficients of mussel droppers are assumed to be similar to ultra-rough cylinders with $C_{dn} = 1.7$ (Plew et al., 2005; Stevens et al., 2008).

A more rigorous investigation of the drag was conducted with artificial mussel crop rope and provided an estimate of $C_{dn} = 1.3$ for Reynolds number from 1×10^4 to 7×10^4 (Plew et al., 2009). These values were used, for example, in a submersible mussel raft dynamics research (Dewhurst, 2016). Recent experiments with live mussel droppers (Landmann et al., 2019) resulted in mean normal drag coefficients of $1.16 - 3.03$ for Reynolds numbers from 2×10^4 to 1.1×10^5. The authors of that publication observed that the drag coefficients increase with decrease of Reynolds number. The results of the abovementioned studies are summarized in Table 6. Note that no significant variations in the added mass and tangential drag coefficients of mussel dropper have been reported. To the best of the authors' knowledge, these properties of a mussel dropper are relatively unexplored and require further investigation.

Our numerical studies show that predictions for mooring line tensions and the overall longline dynamics are not very sensitive to the exact choice of the normal and tangential drag coefficients, if they are taken within a reasonable range of values, see Section 5.2. The results reported in

Section 5 correspond to the Reynolds number of 4×10^4 and greater. The values $C_{dn} = 1.3$, $C_{dt} = 0.1$, $C_a = 1$ were adopted unless otherwise specified.

Table 1.6. Reported values of normal drag C_{dn} and tangential drag C_{dt} coefficients for a mussel dropper. Added mass coefficient is denoted as C_a.

Source	C_{dn}	C_{dt}	C_a
Raman-Nair and Colbourne, 2003	1.5	-	-
Plew, 2005	1.1	-	1
Raman-Nair et al., 2008	1.2	0.1	-
Stevens et al., 2008	1.7	-	-
Plew et al., 2009	1.3	-	-
Dewhurst, 2016	1.3	-	1
Gagnon and Bergeron, 2017	1.1	0.08	-
Landmann et al., 2019	1.16-3.03	-	0.25-1.25

5. Performance of submerged mussel longline in a high-energy environment

5.1 Equivalent dropper concept validation

In order to validate the equivalent dropper approach in terms of the dynamic (tension, reaction force) and kinematic (displacement, velocity, acceleration) responses, the numerically predicted behavior of the initial 2-point mooring configuration with 80 actual *yellow* droppers (Fig. 1.7a) was compared to 8 equivalent ones (Fig. 1.7b) subjected to the same fair weather condition, so each equivalent dropper represents hydrostatic and hydrodynamic forces acting on 10 equivalent droppers, see Section 3.

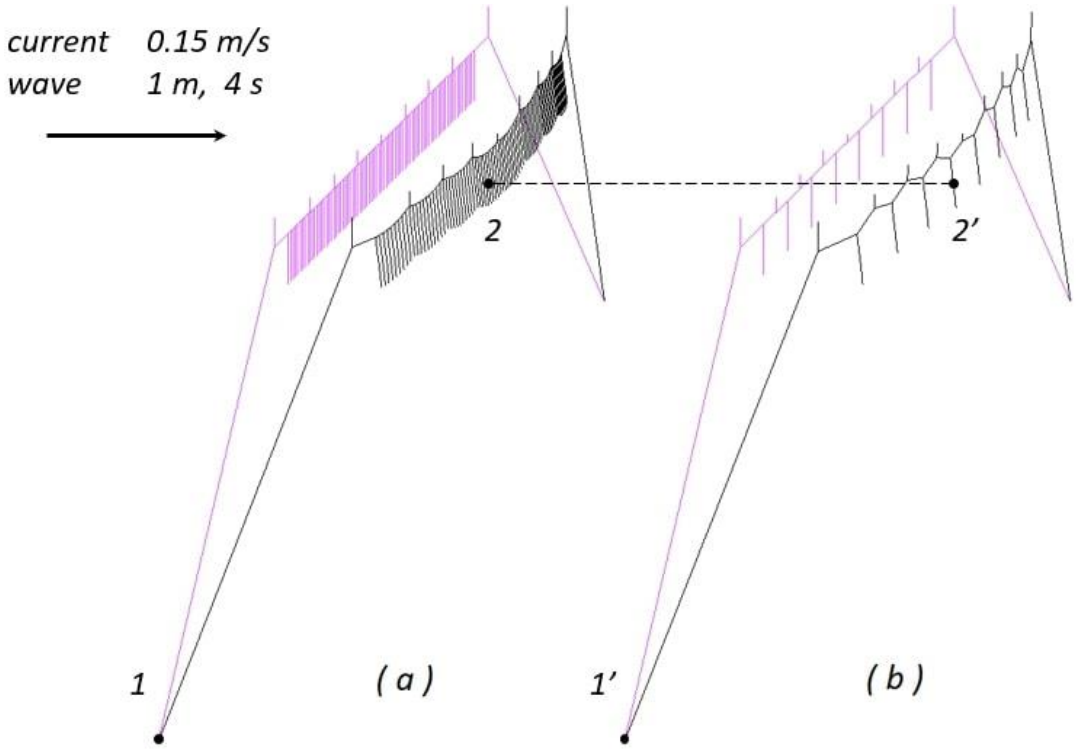

Figure 1.7. Initial and deformed state of the 2-point longline design under the fair environmental condition with: *(a)* actual *yellow* droppers; *(b)* equivalent *yellow* droppers. The deformed state corresponds to the maximum deflection from the initial position. Points *1* and *1'* are the mooring line attachments. Points *2* and *2'* are at the middle of the 4th dropper.

Table 1.7 presents maximum mooring line tension T at points *1* and 1', horizontal displacement d_x, absolute value of velocity v and absolute value of acceleration a at points 2 and 2', where locations *1, 1', 2* and *2'* are provided in Fig. 7. Numerical simulations show good agreement between actual and equivalent finite element models (Fig. 1.8) with less than 5% difference in maximum values (Table 1.7). The maximum values of T, d_x, v and a have a special interest for ocean engineers since they usually serve as a general criterion for reliability, durability and performance of a longline mussel farm structure (Raman-Nair and Colbourne, 2003; Raman-Nair et al., 2008). For this particular configuration, the equivalent dropper approach provides more

than 3.5 times speed-up of numerical calculation when performed with *Intel® Core™ i7-3770, 3.40 GHz* processor on 2 cores.

Table 1.7. Maximum values of tension, displacement, velocity and acceleration of actual and equivalent longline models.

Dropper type	$\boldsymbol{T}$ $[\boldsymbol{kN}]$	$\boldsymbol{d_x}$ $[\boldsymbol{m}]$	$\boldsymbol{v}$ $[\boldsymbol{m/s}]$	$\boldsymbol{a}$ $[\boldsymbol{m/s^2}]$
Actual dropper	2.44	7.22	0.061	0.093
Equivalent dropper	2.48	7.16	0.060	0.097
Difference	1.9 %	0.8 %	1.6 %	4.3 %

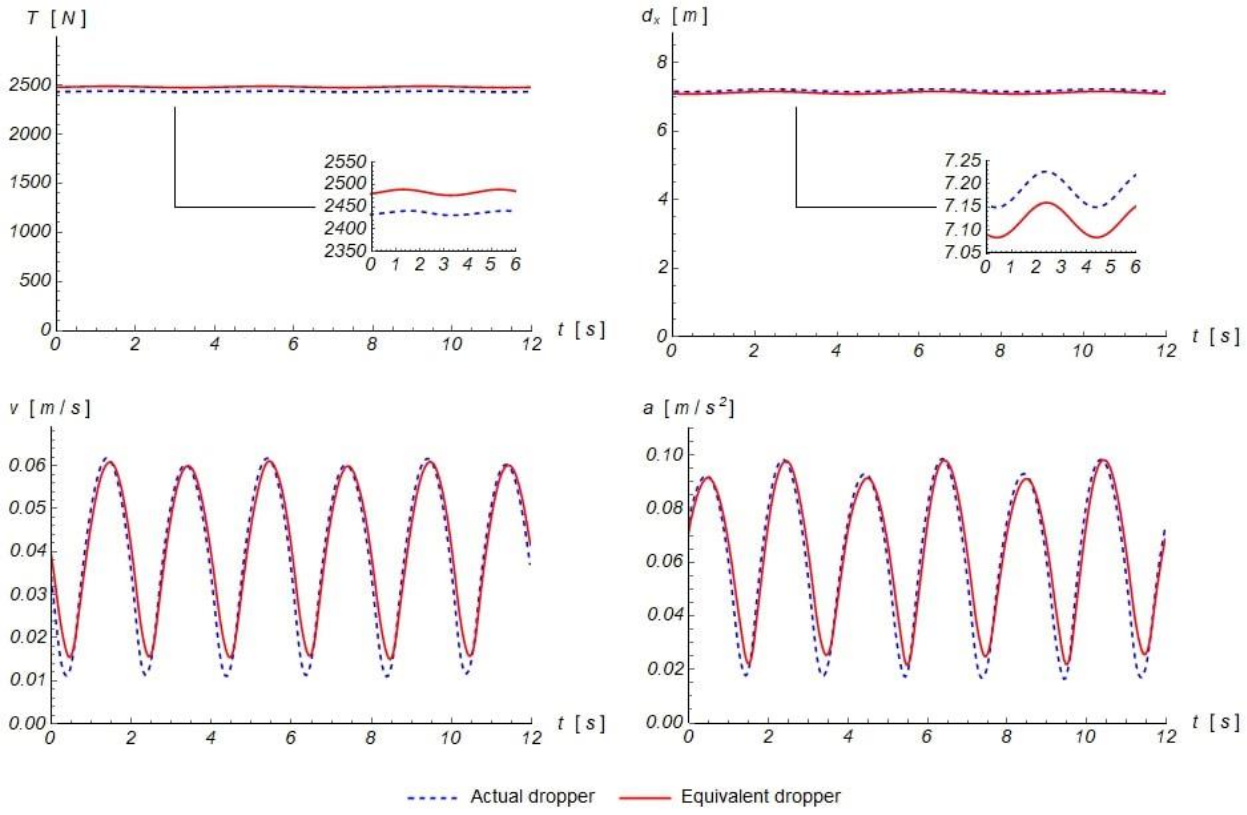

Figure 1.8. Comparison between actual and equivalent longline model response in fair weather. T is the mooring tension, and displacements d_x, velocities v and acceleration a are provided for the midpoint of the 4th dropper.

5.2 Parametric studies for drag coefficient and bending stiffness contribution.

In this section, the sensitivity of the numerical predictions to the exact choice of the dropper drag coefficient and bending stiffness is investigated. The 4-point mooring design with *yellow* droppers under the storm conditions was selected for the parametric study. Since most of the reported normal drag coefficients are $1.1 \leq C_{dn} \leq 1.7$, there were four models chosen for the study based on the dropper's C_{dn} and the element type: $C_{dn} = 1.1$ with truss elements; $C_{dn} = 1.1$ with beam elements; $C_{dn} = 1.7$ with truss elements; $C_{dn} = 1.7$ with beam elements. These cases were compared with each other and with the benchmark $C_{dn} = 1.3$ with beam element case.

Fig. 1.9 provides mooring tension at anchor point 1' and kinematic response point 2', where the location of points is shown in Fig. 1.8b. It can be seen in Table 1.8 that the maximum deviation from the parameters chosen in the performance study ($C_{dn} = 1.3$ with beam elements) does not exceed 7.6% in terms of highest tension, 5.5% in displacement, 1.3% in velocity and 1.7% in acceleration. This parametric study shows that the combined effect of perturbing the drag coefficient by ± 30% and switching on and off the effect of bending stiffness in the model are bound by well-defined narrow intervals in all of the considered quantities of interest. For all practical intents and purposes, these bounds are within the expected variations of the experimental measurements, and thus these parameters can be fixed in the midrange value and their variations deemed statistically insignificant to the variations in the predicted results.

Table 1.8. Maximum values of tension, displacement, velocity and acceleration for truss and beam models with different dropper drag coefficients.

Drag coefficient, element type	$\boldsymbol{T}$ $\boldsymbol{[kN]}$	$\boldsymbol{d_x}$ $\boldsymbol{[m]}$	$\boldsymbol{v}$ $\boldsymbol{[m/s]}$	$\boldsymbol{a}$ $\boldsymbol{[m/s^2]}$
$C_D = 1.1$, truss elements	3.80	9.57	1.45	1.01
$C_D = 1.1$, beam elements	3.98	9.53	1.43	1.03
$C_D = 1.7$, truss elements	4.27	10.60	1.46	1.00
$C_D = 1.7$, beam elements	4.46	10.54	1.45	0.99
Maximum deviation from $C_D = 1.3$, beam elements	7.6%	5.5%	1.3%	1.7%

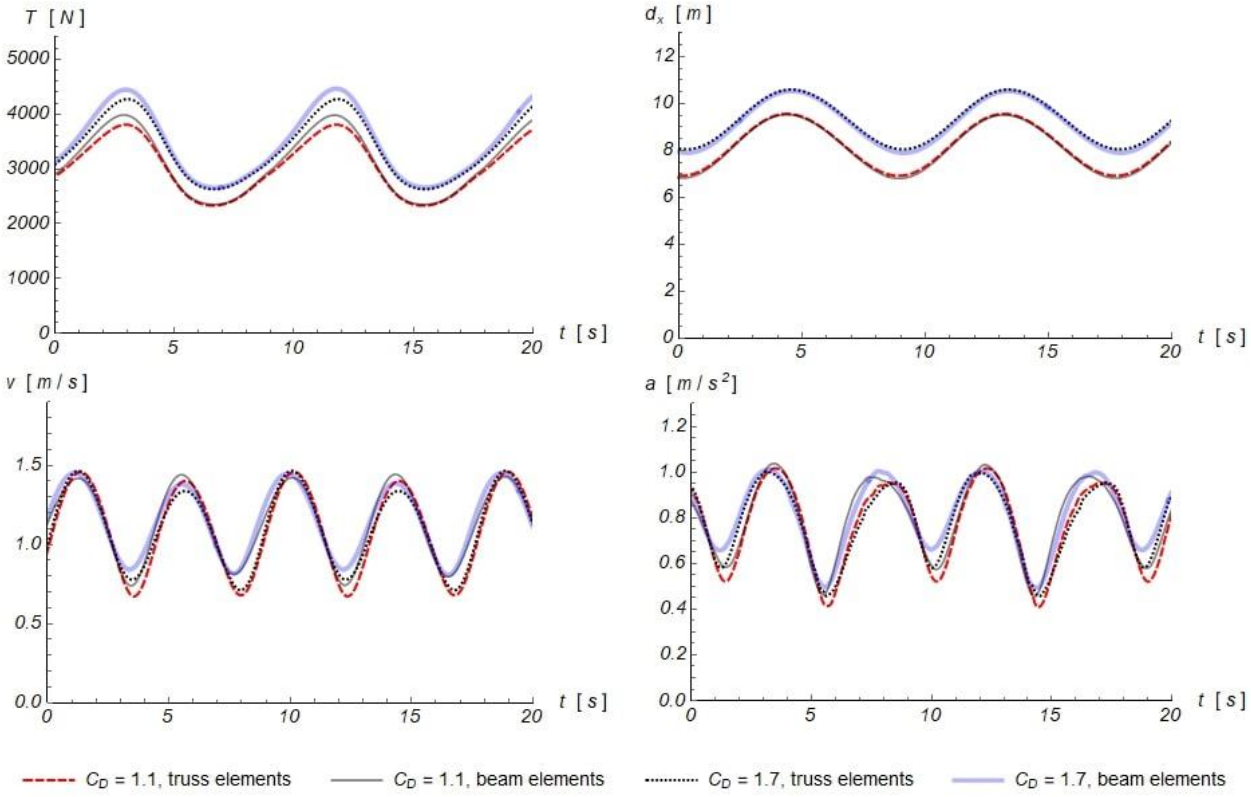

Figure 1.9. Drag coefficient and bending stiffness parametric study results in storm conditions. T is the mooring tension, and displacements d_x, velocities v and acceleration a are provided for the midpoint of the 4th dropper.

5.3 Performance of mussel longline in fair and stormy weather

Four longline designs were considered, including the initial 2-anchor system (Fig. 1.6a), the modified 4-anchor system (Fig. 1.6b and b1), the 4-anchor system with around 10% of the dropper weight added to the lower end of each dropper (Fig. 1.6b and b2), and the 4-anchor system with three intermediate vertical anchor legs (Fig. 1.6c), as described in Sections 2.1 and 3.3. Each of these designs was numerically simulated in fair and storm environments with three different sleeve types, namely *yellow*, *blue* and *green* (Table 1.2). The collinear wave and current directions parallel to the seafloor and perpendicular to the mainline were chosen for these simulations since they had been found to cause an excessive structure motion in the original design. As output data, a maximum tension of the mooring line T at point *1* and maximum horizontal displacement d_x, velocity v, acceleration a, horizontal projection of relative velocity v_{rx}, vertical projection of relative velocity v_{rz} and vertical projection of acceleration a_z at points *2, 3, 4, 5* were chosen, see Fig. 1.10. All of the predicted results are summarized in Table A.1 and A.2, see Appendix A.

Fig. 1.11 presents results of the numerical simulations organized as a ratio of the maximum observed value of the mooring tension, horizontal displacement, dropper velocity, acceleration and vertical acceleration for a specific design to the corresponding value for basic 2-point mooring line configuration. Comparisons indicate that changing the basic 2-point mooring system (the present standard for field deployment) to the 4-point mooring system greatly reduces displacement (by 50-65%, depending on dropper type), but mooring tension, velocity and acceleration are usually the same or increase. Adding weight to the ends of the droppers, however, generally decreases mooring tension, velocity and acceleration with the vertical projection of acceleration reduced by 20-35%. Adding additional vertical legs with fixed anchoring decreases mooring tension and

displacement by 20-30%, but velocity and acceleration are 1.66-1.79 times higher (Fig. 1.11). From the standpoint of mussel retention, only adding weight seems to have substantial beneficial effect. Extra model runs included the use of a circular heave plate attached to the bottom of each dropper to provide additional vertical drag and added mass, but numerical simulations did not show any advantage for such design. Also, the increase of a storm wave height from $5\ m$ to $9\ m$ resulted in increase of the motion response by about 30% for all considered configurations.

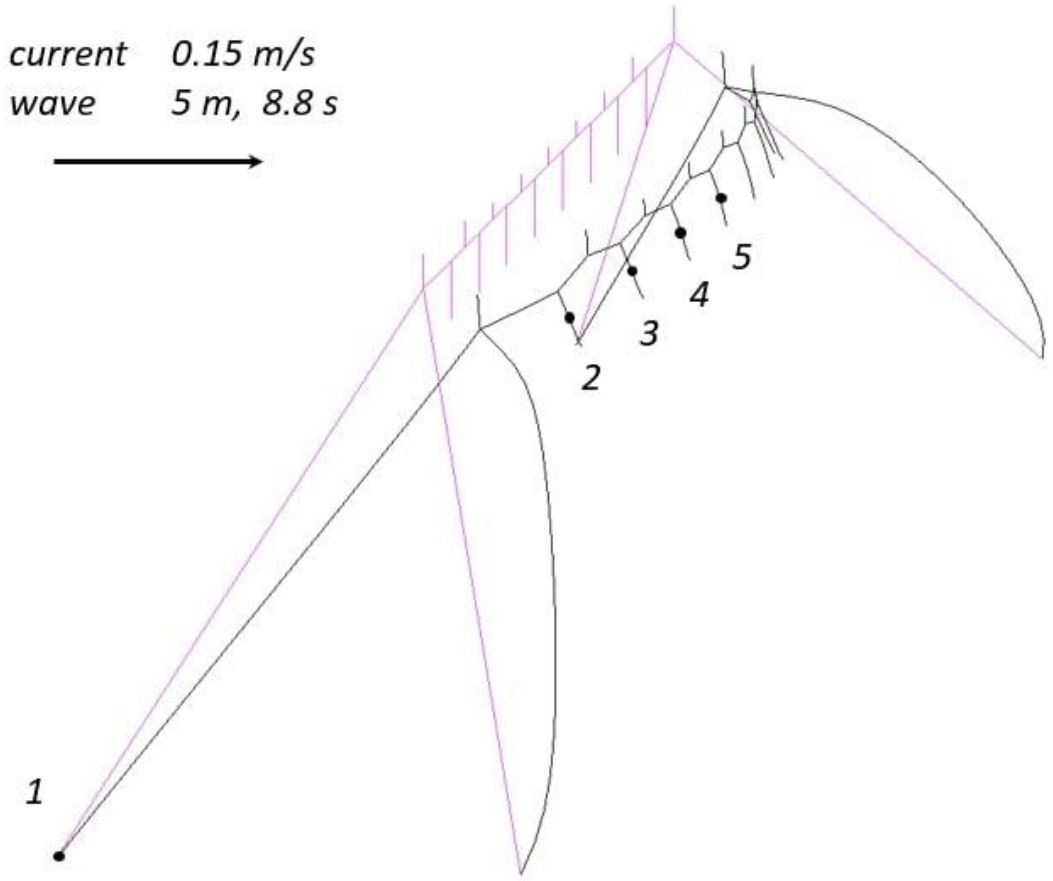

Figure 1.10. The 4-point mooring longline with *blue* droppers in storm conditions. Both current and wave are normal to the mainline. Tension is measured at mooring line attachment point *1*, while displacements, velocities and accelerations are monitored at points *2, 3, 4, 5*.

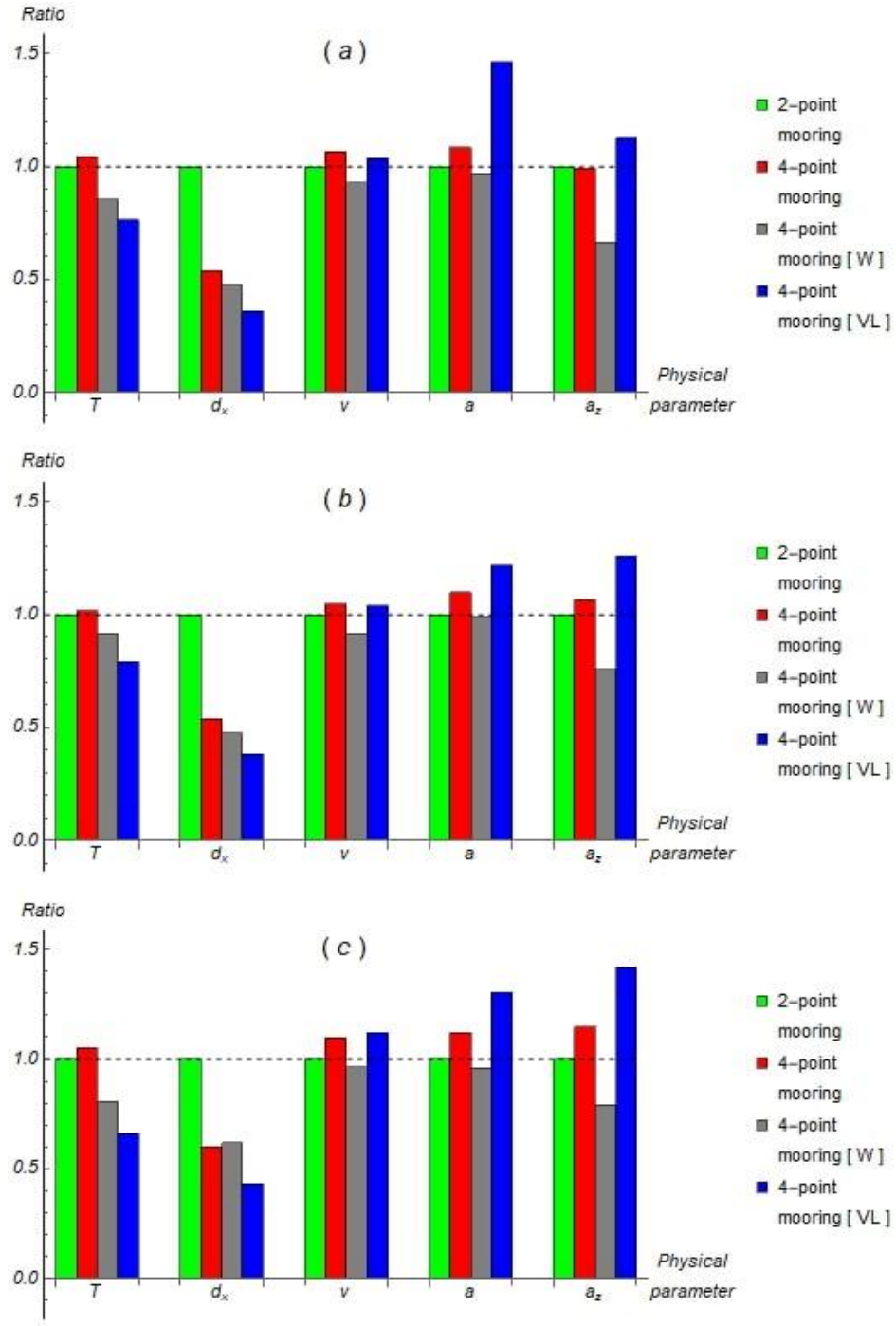

Figure 1.11. Ratio of the system response parameters to the corresponding values for the 2-point mooring design. Relative peak values of mooring tension T, horizontal displacement d_x, velocity v, acceleration a and its vertical projection a_z of four considered designs with *(a) yellow*, *(b) blue* and *(c) green* droppers. Mooring tension is the maximum predicted near the fixed anchors. Displacement, velocity and acceleration are maximum values predicted for droppers. The x-direction is in the direction of wave and current, and the z-direction

Fig. 1.12 provides results of the simulations as a ratio of the maximum predicted value of the system response parameters for a specific dropper type to the corresponding values for weighted 4-point mooring line configuration with the *yellow* dropper. Comparison of different protective sleeve designs shows that their performance is directly correlated with the linear density and diameter, as determined by their mussel content. Utilization of the Vexar Superduty green sleeve resulted in much higher linear density of the dropper requiring more compensating floats and producing significantly higher mooring line tensions and horizontal mainline displacements for both fair and stormy conditions, see Fig. 1.12. Note that in the case of fair weather, the absolute values of velocities and accelerations are very low, so small differences can lead to significant jumps in ratios. For example, the absolute values of vertical acceleration for *blue* and *green* dropper are $0.02\ m/s^2$ and $0.01\ m/s^2$, and this small difference is shown as 2 times reductions in Fig. 1.12a.

The simulation results presented in this section can be compared with other investigations of similar configurations. The offshore observations of a $189\ m$ long fully submerged mussel longline with 12 legs at $20-24\ m$ depth open ocean site (Gagnon and Bergeron, 2017) show that the ratio between the $0.6\ kN$ maximum tension and the $0.25\ kN$ pretension of mooring lines is around 2.4 (with maximum current velocity of $0.24\ m/s$, wave height of $3.5\ m$ and wave length of $96\ m$), while our 2-point mooring longline model with the *blue* droppers of the same diameter predicts a ratio of $3.65\ kN\ /\ 2.5\ kN = 1.46$ in storm conditions. However, for the rest of 4-point mooring models with $1.5\ kN$ pretension this ratio is somewhat higher, up to 2.47. Furthermore, their open ocean site observations report the maximum droppers' vertical acceleration $0.3\ m/s^2$, which is less than half the acceleration predicted in our numerical simulations for stormy weather.

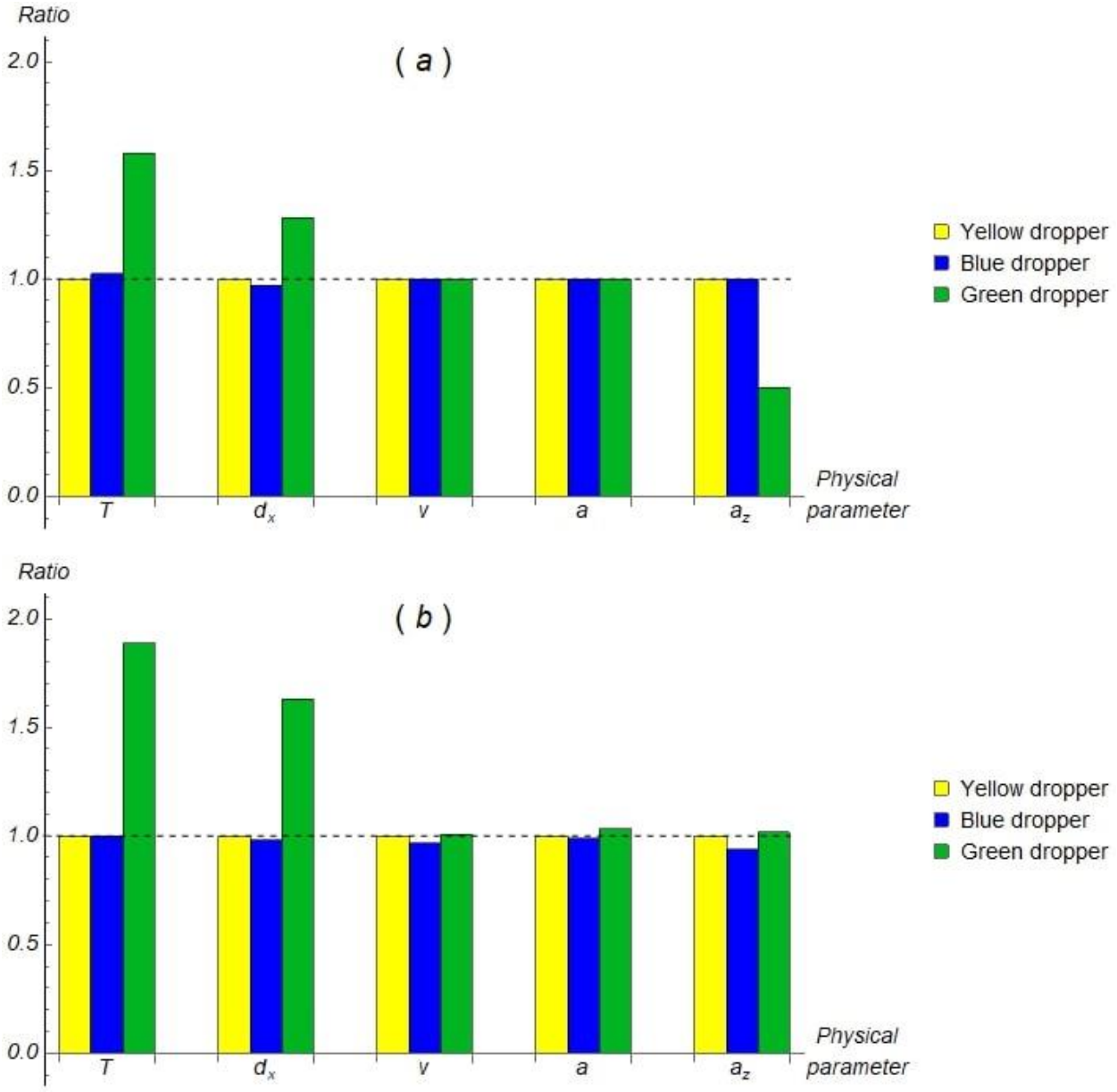

Figure 1.12. Ratio of the system response parameters to the corresponding values for the 4-point mooring [W] design with *yellow* dropper. Relative peak values of mooring tension T, horizontal displacement d_x, velocity v, acceleration a and its vertical projection a_z for four considered designs in *(a)* fair and *(b)* stormy weather. Mooring tension is the maximum predicted near the fixed anchors. Displacement, velocity and acceleration are maximum values predicted for droppers. The x-direction is in the direction of wave and current, and the z-direction is upwards.

This discrepancy is caused by the difference in wave height, length and water depth, as well as design features, such as the number of additional legs, distribution of floats and droppers, etc. Nevertheless, a maximum inclination of $31°$ predicted by the numerical simulation in the present work is comparable to the maximum inclination of $24°$ from the observations.

Another offshore observation of a $150\ m$ long partially submerged mussel longline (Stevens et al., 2007) recorded maximum mooring line tensions from $6.0\ kN$ to $7.7\ kN$ and a maximum dropper acceleration of around $4.5\ m/s^2$ under a $0.16\ m/s$ tidal current in $11\ m$ water depth. It can be seen that their values are of a different order from ours, since the droppers are much closer to the water surface and, as a result, experience higher fluid velocities and accelerations.

At the same time, the numerical dynamic analysis of a $200\ m$ fully submerged mussel longline system presented in Raman-Nair et al., 2008 resulted in a wave-induced ($3\ m$ wave height, $8.5\ s$ wave period and $99.6\ m$ wave length) average mooring line tension of $1.25\ kN$ and a maximum tension of $2.25\ kN$. Although those tensions are of the same order as the ones presented in this paper, they are still around 35% lower due to an absence of the current, slightly different wave properties, different longline design and the wave propagation direction at $65.5°$ to the mainline.

6. Conclusions

Hydrodynamic modeling software *Hydro-FE* is demonstrated to be an efficient finite element numerical tool to predict structural response of flexible aquaculture installations subjected to offshore environmental loading conditions. It was used in the present study to evaluate the dynamic performance of several simple submerged longline designs with different mussel droppers under

the fair and stormy weather typical for the considered North Atlantic mussel farming site. The loading from waves was implemented using the linear Airy wave theory. The Reynolds number dependent drag coefficients were incorporated in the hydrodynamic forcing formulas. The equivalent dropper concept was proposed and verified to provide a good proxy model with statistically insignificant variations (under 5%) in all of the considered quantities of interest when compared to the predictions of the full model. This led to significant computational 3.5 times speed-up and improved performance of simulations.

Field measurements taken at the University of New Hampshire nearshore multi-trophic aquaculture site show that mechanical properties of mussel droppers are different for different sleeves and vary in diameter, mass and bending stiffness. Numerical simulations indicate that the effect of bending stiffness on the overall structural response of the considered mussel droppers is negligible. In addition, variations of the dropper normal drag coefficients in the reported range of values from 1.1 to 1.7 result in insignificant deviations (when compared to the margin of error of experimental measurements) from the predictions obtained for the commonly used value of 1.3: 7.6% in mooring tensions, 5.5% in the middle dropper displacements and 1.7% in its accelerations. Combination of field measurements and numerical simulations has been used to evaluate the effect of various protective sleeves and structural designs on the performance of longline mussel farms. Comparisons show that adding 2 additional mooring lines to the basic 2-point mooring systems reduces horizontal displacement by 50-65%, depending on dropper type. Also, the weights attached to the ends of the droppers generally decrease their velocities and accelerations with the vertical projection of acceleration reduced by 20-35%. Additional vertical legs with fixed anchoring decrease mooring tensions and droppers' horizontal displacements by 20-30%, but

velocities and accelerations are 1.66-1.79 times higher than in weighted configuration. From the standpoint of mussel retention, adding 2 mooring lines and weight seem to have some beneficial effects.

Although mussel farms are typically large operations with multiple longlines, this study was focused on modeling of the single mussel longline response for different environmental conditions. It is expected that the approach will be applicable to larger farms if modifications of environmental conditions, such as current shadowing and spatial variations in currents and waves are taken into account.

Overall, it has been demonstrated that the proposed model with the equivalent droppers provide a robust and computationally efficient engineering tool with strong predictive capability which was verified through the parametric studies and validated via the comparison to the existing field measurements. Thus, adoption of this tool by researchers and practitioners can enable model-based engineering flows for designing optimal mussel farming systems with well-defined hydrodynamic response characteristics in the operational and storm conditions. We anticipate that this can yield improved accuracy in the predictions of the service life and reduced costs of the components required to build these systems.

Chapter II

Numerical modeling of kelp aggregates based on hydrodynamic characteristics determined from full-scale towing experiments

This chapter is prepared for submission to *Aquacultural Engineering* journal as *Knysh, A., Fredriksson, D., Drach, A., Dewhurst, T., Tsukrov, I. Numerical modeling of kelp aggregates based on hydrodynamic characteristics determined from full-scale towing experiments.*

My contribution to the paper was development and calibration of the equivalent finite element formulation using the full-scale tow experiments of kelp aggregate conducted in Hydromechanics Laboratory at the United States Naval Academy. I also participated in preparation of the manuscript for publication.

Abstract

The objective of this study is to propose a finite element model representation of densely grown kelp for applications in a hydrodynamic-structural, time-domain modeling of seaweed aquaculture systems. The finite element model replicates the tow tank tests of the full-scale physical model of the aggregate kelp line conducted at United States Naval Academy (Fredriksson

et al., 2020). It was built using measurements of kelp blade length and width, number of blades, and material mass density. The finite element model is based on the Morison-type equation with the hydrodynamic coefficients determined from the tow tests. The assessment of these hydrodynamic coefficients was performed using empirical results from tow tests using a *1 m*, full-scale physical model. The tow tests were then replicated in finite element simulations (*Hydro-FE* software) to verify the balance of hydrostatic, hydrodynamic, and internal forces for the aggregate.

1. Introduction

The growth of marine aquaculture depends upon the development of reliable ocean engineering design techniques incorporating numerical modeling as an important component. Hydrodynamic-structural modeling procedures of aquaculture systems are well-defined for finfish systems comprised of net type structures (Klebert et al., 2013). Applications to shellfish aquaculture structures also exist (Wang et al., 2015; Dewhurst, 2016; Dewhurst et al., 2019; Pribadi et al., 2019; Knysh et al., 2020). Most of these modeling techniques require the use of empirical datasets to characterize the hydrodynamics of the aquaculture components with a primary focus on drag forcing. Empirical datasets for a variety of net structures for finfish aquaculture have been developed (Swift et al., 2006; Zhan et al., 2006; Tsukrov et al., 2011; Kristiansen and Faltinsen, 2012; Gansel et al., 2015). Datasets for shellfish aquaculture components include results from physical model experiments such as Landmann et al., 2019 for mussel droppers, and Fredriksson et al., 2010 for oyster trays. Xu et al., 2020 used computational fluid dynamic (CFD) approaches to assess steady drag characteristics for mussels.

Hydrodynamic-structural modeling of macroalgae farming systems of *Laminariales* (kelps) present unique challenges since these kelps grow densely (Kim et al., 2015; Augyte et al., 2017), are compliant (Buck and Buchholz, 2005; Henry, 2014; Rominger and Nepf, 2014), and are often close to being neutrally buoyant (Vettori and Nikora, 2017). To address these challenges, Fredriksson et al., 2020 examined the steady flow hydrodynamics of a full-scale physical model representing *1 m* aggregate of *Saccharina latissima* grown on an ocean-deployed farm in a series of tow tank experiments. The results of the tow tank experiments were processed considering the cross-flow principle (Hoerner, 1965) yielding normal and tangential drag force datasets for aligned and perpendicular tow orientations as a function of horizontal speed. This approach was taken since it fits into typical time-domain modeling schemes, many of which are referenced in Knysh et al., 2020, that incorporate a form of the Morison Equation (Morison et al., 1950; Goodman and Breslin, 1976) to calculate instantaneous drag values in unsteady flows.

The objective of this paper is to propose a technique to model densely grown, farmed kelp lines in a time-domain software called *Hydro-FE* (see Tsukrov et al., 2003; Fredriksson et al., 2007; Knysh et al., 2020 for description of *Hydro-FE* and its original version *Aqua-FE*) utilizing the experimental drag force measurements of Fredriksson et al., 2020. Simulations were performed to verify the balance of forces in the tow tests of the physical model with *5* towing speeds in both aligned and perpendicular orientations.

2. Tow tank tests on a full-scale kelp aggregate model

The full-scale kelp aggregate model is described in Fredriksson et al., 2020. A set of tow tank experiments were conducted at the United States Naval Academy with a full-scale physical model

representing a *1 m* section of kelp aggregate (Fig. 2.1). Biomass properties of the physical model were based on nominal characteristics from samples harvested from a horizontal, near surface kelp line at a protected site in Saco Bay, Maine, USA in 2016. Specific geometric and material properties were estimated from a combination of wild samples obtained locally and cultured samples from a nearby farm. The model was constructed with *178* strips of low-density polyethylene (LDPE) plastic each having a length of *3 m*, nominal width of *0.0741 m* and thickness of *0.000213 m*. The flexural rigidity EI of the individual LDPE strips was measured in the cantilever beam type test and was equal to $2.19\times10^{-5}\ N\text{-}m^2$, where E is the Young's modulus of the material and I is the second moment of area of the strip cross-section. For the strip cross-section, I was calculated to be $5.95\times10^{-14}\ m^4$ which results in E of *367 MPa* and is consistent with published values of LDPE. Choosing *178* strips per meter to represent the number of kelp blades for the aggregate model was a balance between what could fit on the mount and the number of plants found growing in-situ. Augyte et al., 2017 reported that "skinny" kelp can grow up to *330* plants per meter. At the Saco Bay site, it was found from sampling during the 2018 harvest that up to *49* blades grew on *10 cm* sections of grow line.

While the physical model did not have the same number of strips per meter, the mass of the aggregate was reproduced in the model by attaching washers to each piece of LDPE to achieve *16.11 kg*, consistent with estimates from the 2016 kelp harvest in Saco Bay. By matching growth yield and maximizing the number of strips per meter of the model with washers, the resulting aggregate mass density was determined to be $1379\ kg/m^3$. While this value was consistent with the limited samples used in the Fredriksson et al., 2020 study, it has since been found to be larger than the more recent measured harvest value of $1052\ kg/m^3$ as described in St-Gelais et al., 2022.

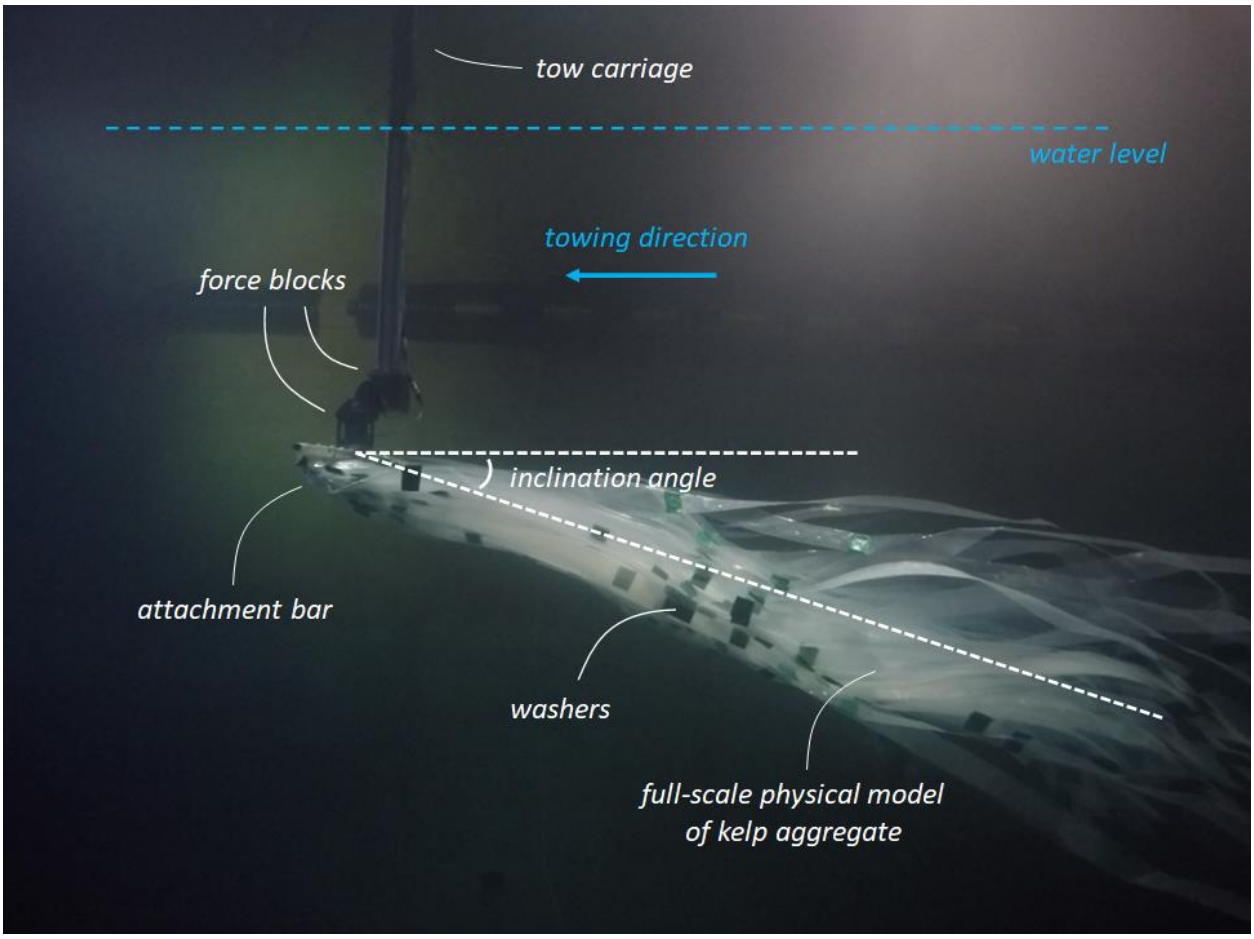

Fig. 2.1. Full-scale physical model of the kelp aggregate during one of the tow tank tests at the United States Naval Academy.

During the tank tests, the kelp aggregate model was towed along the *166 m* × *7.9 m* × *4.9 m* tank facility in the Hydromechanics Laboratory at the United States Naval Academy. Both mounted-kelp and the mounted-tare setups (with and without kelp model attached, respectively) were towed with the *1 m* attachment bar at orientations aligned and perpendicular to the towing direction. The setups were attached to the tow carriage with vertical struts and force blocks to measure both horizontal and vertical forces (Fig. 2.2). See Fredriksson et al., 2010 for the complete description of the force blocks characteristics and calibration.

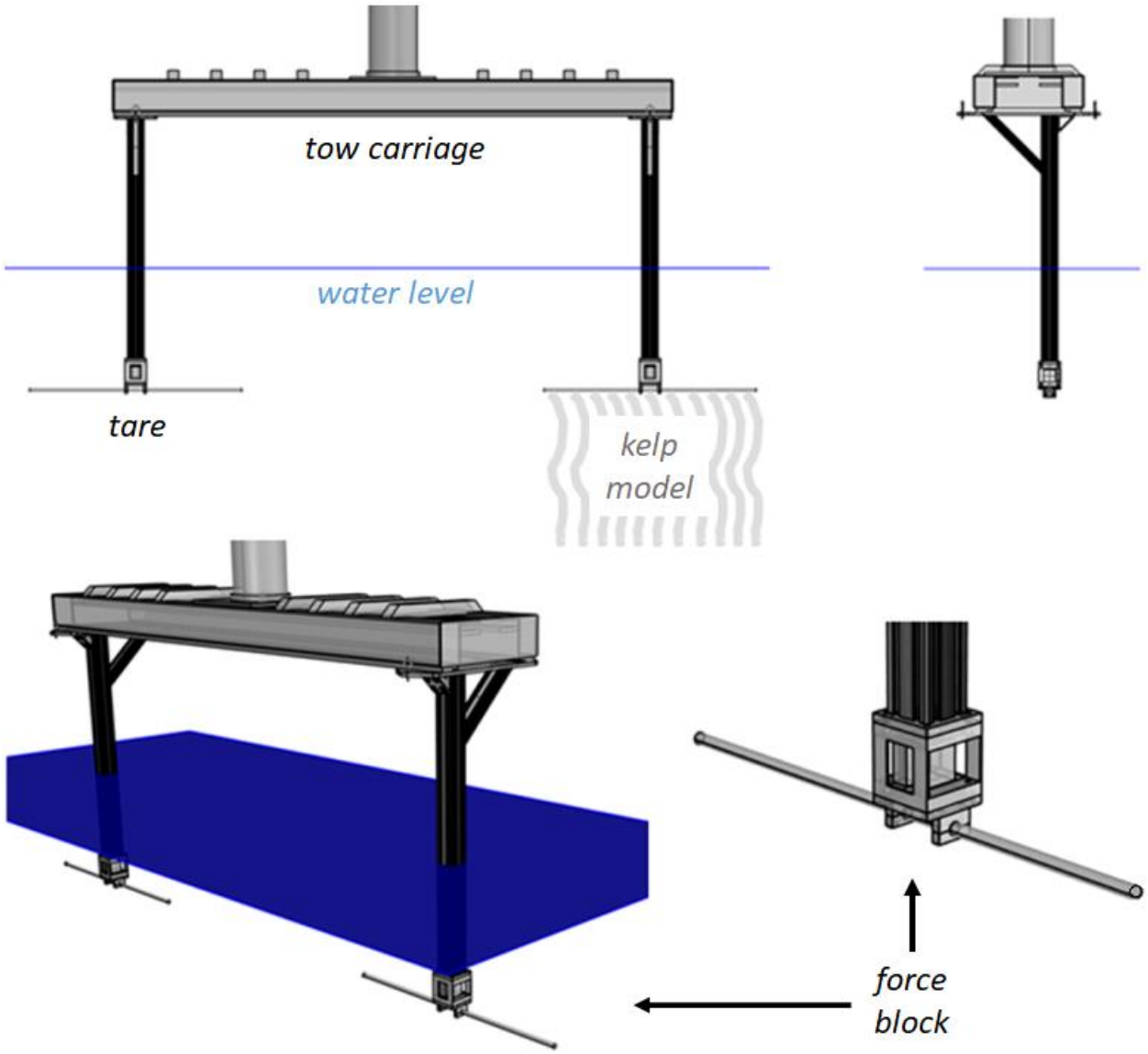

Fig. 2.2. The experimental setup: tow carriage, tare, force block and kelp aggregate model. Only horizontal block is shown in the figure (Source: Fredriksson et al., 2010).

A total of *15* tow tests were conducted in two towing orientations, *7* in aligned and *8* in perpendicular. Each test included towing with 5 different speeds of *0.25, 0.50, 0.75, 1.00* and *1.25 m/s*. Towing velocities, kelp inclination angles, and reaction forces at the force block were

measured during the tow tank tests. A typical set of measurements of the towing velocities in the aligned and perpendicular orientations is shown in Fig. 2.3. To deal with the noise on the measurements, the *median filter* with a neighbor range of *20* was applied to smooth them out for further numerical modeling inputs.

The drag forces measured by the force block are presented in Section 4. It can be seen that it takes at least *10 s* to reach the steady state conditions in terms of the horizontal drag measurements at each towing speed. Thus, only the mean of drag measurements from the last *5 s* of each towing speed mode were considered. These values were then averaged for all tow tests and used for further numerical modeling effort. The averaged kelp horizontal drag forces R_x and inclination angles θ (Fig. 2.4) at each towing speed are given in Table 2.1. Note, that the horizontal drag presented in Table 2.1 was calculated as the difference between drag of mounted-kelp and mounted-tare models.

Table 2.1. Inclination angles and horizontal drag forces averaged over the tow tests.

Towing speed	**Aligned orientation**		**Perpendicular orientation**	
v , [*m/s*]	θ , [°]	R_x , [*N*]	θ , [°]	R_x , [*N*]
0.25	*25.1*	*32.79*	*24.4*	*35.61*
0.50	*14.1*	*40.49*	*13.8*	*42.09*
0.75	*10.1*	*51.24*	*8.3*	*52.23*
1.00	*8.3*	*64.41*	*7.8*	*72.90*
1.25	*6.5*	*82.48*	*5.7*	*103.33*

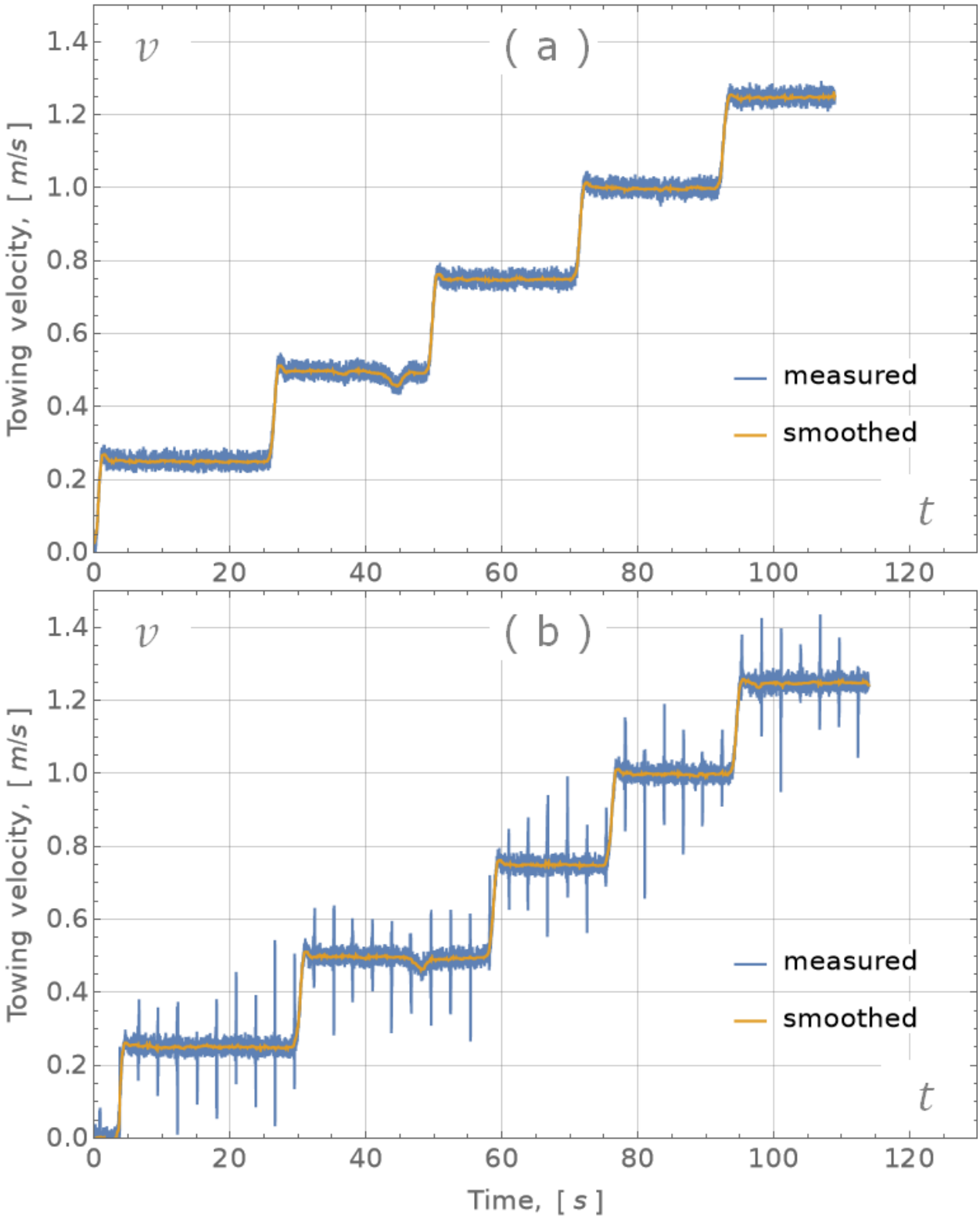

Fig. 2.3. Representative (a) aligned and (b) perpendicular towing velocity measurements.

3. Hydrodynamic coefficients from the full-scale model

3.1 Morison equation

The time-domain modeling approach is implemented in a nonlinear, dynamic, finite element software *Hydro-FE* that is integrated as a set of user-defined subroutines into a commercial, general-purpose program Marc. It is used to calculate forces and the dynamic response of flexible structures in marine environments and was recently described in Knysh et al., 2021 and Knysh et al., 2022. The solver incorporates an updated Lagrangian formulation to account for large displacements, rotations and strains of structural elements. Time-integration of the governing equations is performed using an implicit (single step Houbolt) scheme with the Newton-Raphson method embedded at each time step to obtain the solution of the nonlinear equations of motion. The formulation for the kelp modeling approach is similar to that of the consistent net-elements (Tsukrov et al., 2003) and the equivalent dropper-elements (Knysh et al., 2020). The hydrodynamic forces acting on the kelp-element in the presence of waves and currents can be expressed with a Morison equation approach (Morison et al., 1950) that was initially developed for cylindrical-shaped bodies and later expanded to the case of moving cylinders (Goodman and Breslin, 1976):

$$d\boldsymbol{F}_n = \rho_w \frac{\partial \boldsymbol{u}_n}{\partial t} dV + C_a \rho_w \left(\frac{\partial \boldsymbol{u}_n}{\partial t} - \frac{\partial \boldsymbol{v}_n}{\partial t} \right) dV + \frac{1}{2} C_n \rho_w |\boldsymbol{u}_n - \boldsymbol{v}_n| (\boldsymbol{u}_n - \boldsymbol{v}_n) dA$$
$$d\boldsymbol{F}_t = \frac{\pi}{2} C_t \rho_w |\boldsymbol{u}_t - \boldsymbol{v}_t| (\boldsymbol{u}_t - \boldsymbol{v}_t) dA \tag{2.1}$$

where $d\boldsymbol{F}_n$ is the differential normal (perpendicular to the kelp-element axis) and $d\boldsymbol{F}_t$ is the differential tangential (parallel to the kelp-element axis) projections of drag force associated with a differential section length dL of the kelp submerged in water of density ρ_w. The differential

projected area dA and differential volume dV are associated with to the section dL. Local fluid velocity $\boldsymbol{u}$ and body velocity $\boldsymbol{v}$ vectors are both projected on the normal ($\boldsymbol{u}_n$ and $\boldsymbol{v}_n$) and tangential ($\boldsymbol{u}_t$ and $\boldsymbol{v}_t$) directions. The empirical normal drag, tangential drag, and added mass coefficients are denoted as C_n, C_t, and C_a, respectively.

3.2 Numerical modeling of kelp aggregate

The kelp aggregate model (kelp-element) presented in this section utilizes a modified Morison approach as well as kelp physical model properties described in Fredriksson et al., 2020 and presented in Section 2 of this paper for the readers' convenience. The key idea is to present the whole aggregate as a single equivalent cylindrical kelp-element (similarly to the equivalent dropper element presented in Knysh et al., 2020) since utilizing discrete finite elements to reproduce each kelp blade is computationally expensive. The hydrostatic, hydrodynamic, and inertia properties are selected to match those measured during the physical tow tests. We consider the steady-state condition of the kelp aggregate at the arbitrary towing velocity as shown in Fig. 2.4.

It is assumed that the axis of the kelp-element is straight and the normal and tangential drag forces are uniformly distributed along the kelp aggregate. Thus, the resulting drag forces can be applied at the middle of the aggregate, so that the expressions for normal and tangential projections of the total drag force, F_n and F_t, and towing velocity, v_n and v_t, are derived as follows:

$$
\begin{aligned}
F_n &= (W - B)\cos\theta \\
F_t &= R_x \sin\theta + (R_x \tan\theta - W + B)\sin\theta \\
v_n &= v \sin\theta \\
v_t &= v \cos\theta
\end{aligned}
\tag{2.2}
$$

where W is the total weight of the kelp, B is the total buoyancy, R_x is the horizontal drag, and θ is the inclination angle that correspond to the considered towing velocity v. The weight and buoyancy of the kelp model element are calculated from its total mass and density presented in Section 2, while the horizontal drag and inclination angles are listed in Table 2.1. Equations (2.2) are used to calculate the pairs of the load and velocity projections (F_n, v_n) and (F_t, v_t) for all considered aligned and perpendicular towing experiments (shown as data points in Fig. 2.5).

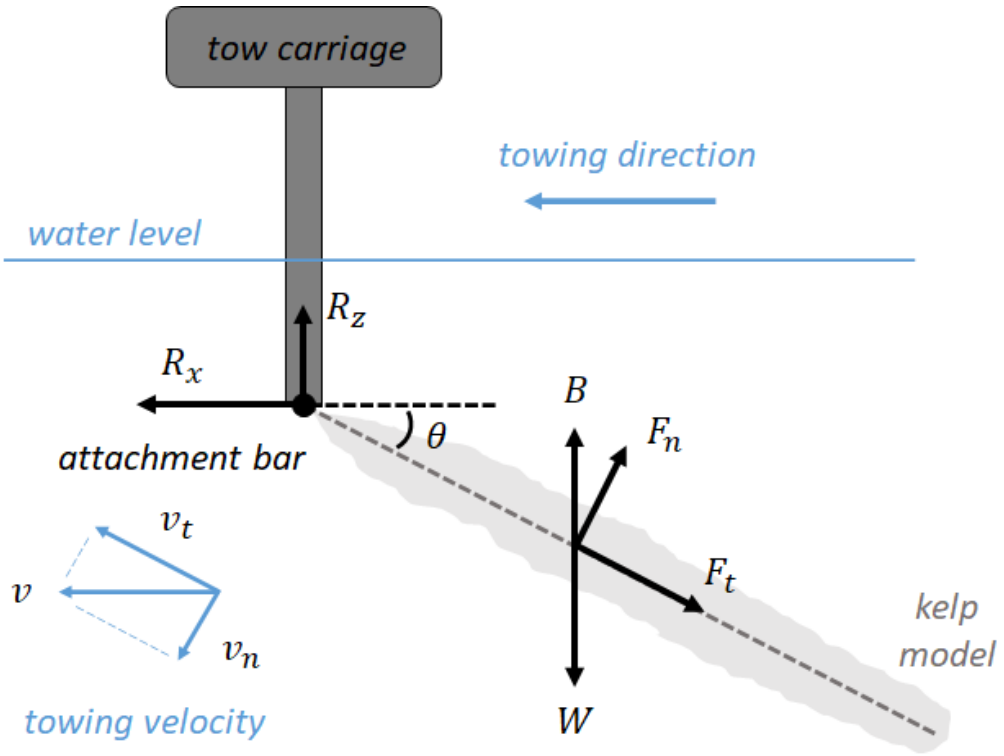

Fig. 2.4. Schematics of the kelp aggregate model during a steady-state portion of the towing test.

The standard Morison equation (2.1) assumes quadratic dependence of drag forces F_n and F_t on the velocities v_n and v_t. This dependence is not observed for the heterogeneous and highly deformable kelp aggregate. For this reason, we propose a modified Morison-type formulation with the variable powers of normal α and tangential β velocity projections in the drag terms:

$$d\boldsymbol{F}_n = \rho_w \frac{\partial \boldsymbol{u}_n}{\partial t} dV + C_a \rho_w \left(\frac{\partial \boldsymbol{u}_n}{\partial t} - \frac{\partial \boldsymbol{v}_n}{\partial t} \right) dV + \frac{1}{2} C_n \rho_w |\boldsymbol{u}_n - \boldsymbol{v}_n|^{\alpha-1} (\boldsymbol{u}_n - \boldsymbol{v}_n) dA$$
$$d\boldsymbol{F}_t = \frac{\pi}{2} C_t \rho_w |\boldsymbol{u}_t - \boldsymbol{v}_t|^{\beta-1} (\boldsymbol{u}_t - \boldsymbol{v}_t) dA \tag{2.3}$$

so the drag force projections corresponding to the steady-state portion of experiments are

$$F_n = \frac{1}{2} C_n \rho_w v_n^{\alpha} A$$
$$F_t = \frac{\pi}{2} C_t \rho_w v_t^{\beta} A \tag{2.4}$$

where A is the projected area. Even though the inertial components of (2.3) in the steady-state conditions are equal to zero due to the absence of accelerations, the volume of the equivalent cylindrical structure should still be equal to the total volume V of the physical kelp model. The same logic is valid for buoyancy B and weight W of the kelp-element. Thus, it is assumed that the length, mass density, and total volume of the equivalent kelp-element is equal to those of the physical kelp model, which leads to the total volume of $V = m/\rho$ with the projected area of $A = \sqrt{4VL/\pi}$, where m is the total mass of the kelp aggregate model, ρ is the density of the kelp aggregate model, L is the kelp strip width (see the values in Section 2). Note that the total mass and density of the aggregate model includes washers attached to the kelp strips.

The nonlinear least squares method was applied to select the parameters C_n, C_t, α and β in (2.4) that fit the experimental data. The selected parameters are presented in Table 2.2, while the

corresponding approximations are depicted with dashed lines in Fig. 2.5. It can be seen that the normal drag data points are located very tight on the plots reflecting the fact that the normal drag force component does not significantly change with the increase of towing velocity due to the increase of inclination angles. It can also be observed that there is a difference between the measurement and the proposed approximation of the tangential force component at the lowest towing velocity for perpendicular orientation. Such a discrepancy at individual points is to be expected as a trade-off between model simplicity (only two additional parameters of α and β were introduced) and its accuracy. Note that in the representations (2.3) and (2.4), drag coefficients C_n and C_t are not unitless, and they are provided in SI system in Table 2.2.

Table 2.2. Parameters of modified Morison equation for aligned and perpendicular orientations.

Orientation / Parameter	C_n	C_t	α	β
Aligned	*0.7162*	*0.1862*	*0.2825*	*0.9520*
Perpendicular	*0.6498*	*0.2214*	*0.2241*	*1.1668*

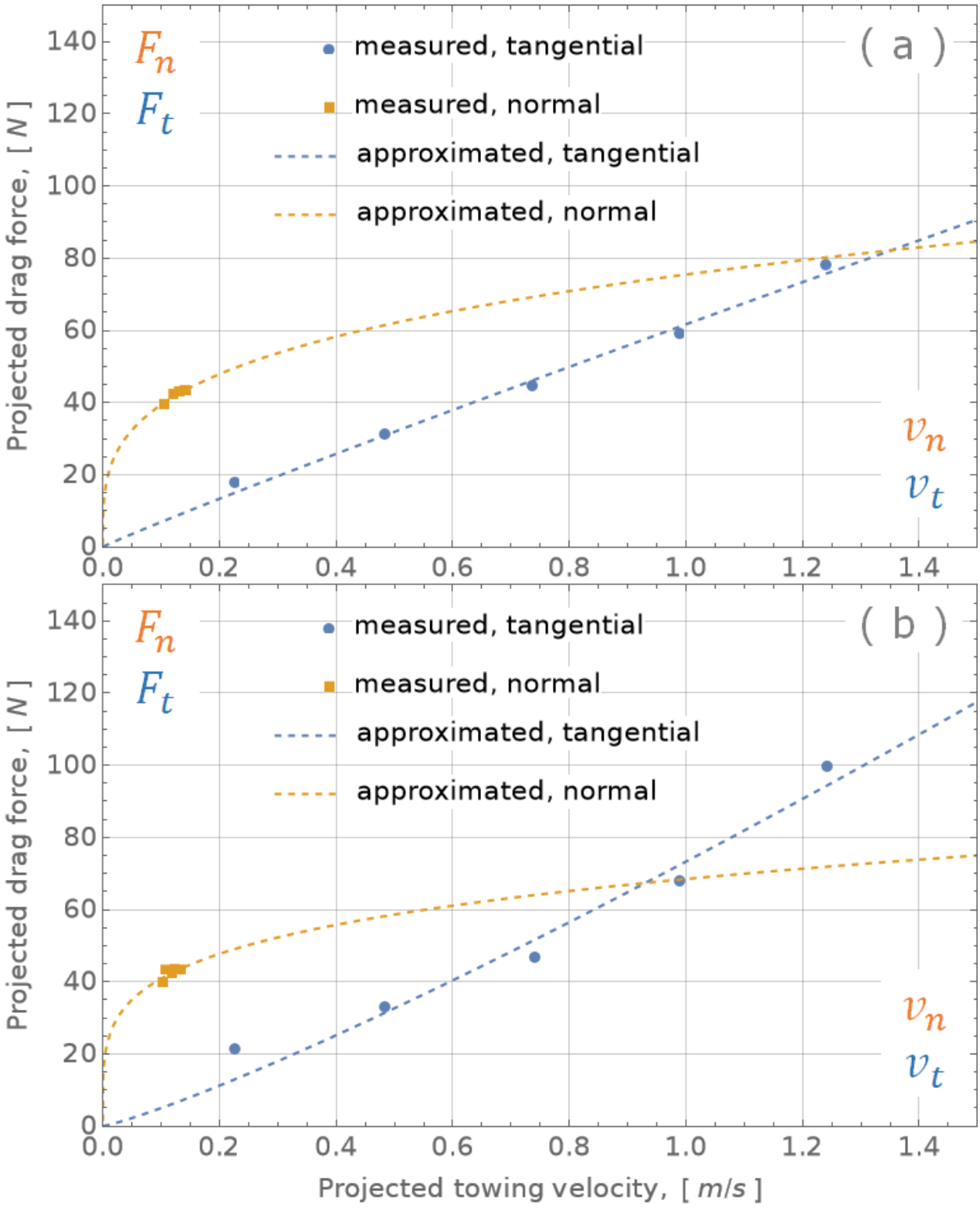

Fig. 2.5. Normal and tangential drag force measurements with the corresponding approximations for (a) aligned and (b) perpendicular kelp aggregate orientations.

4. Numerical model and simulation results

The key idea for numerical modeling of dense kelp aggregates is to substitute them with special finite elements (kelp-elements) having the same hydrodynamic and hydrostatic properties as observed in the full-scale tow experiments. Depending on the importance of the bending stiffness, both truss and beam elements can be used. Table 2.3 presents the choice of parameters for *2-node 3D truss* element representing its length, cross-sectional area, mass density, and Young's modulus.

Table 3. Properties of the kelp-element model for the kelp aggregate used in the full-scale tow tests.

Element type	*2-node 3D truss*
Cross-section type	*circular*
Number of elements	*30*
Element length	*0.1 m*
Cross-sectional area	*0.003891 m^2*
Mass density	*1379 kg/m^3*
Young's modulus	*367 MPa*

To validate the proposed finite element model, the tow experiments conducted in Hydromechanics Laboratory of the United States Naval Academy were simulated in *Hydro-FE* software. The smoothed towing velocity measurements observed in the tests (Fig. 2.3) were first integrated over time and then assigned to a top node of the finite element model in the form of prescribed displacements. The modified Morison equation formulation (2.3) was implemented in *Hydro-FE* to calculate the hydrodynamic forces exerted on the elements. Note that several

additional parametric studies were conducted. Changing the added mass coefficient C_a (from *1* to *2, 5, 10, 50, 100*) and the number of elements (from *30* to *60, 120*) did not demonstrate any noticeable differences in kelp-element dynamics.

Horizontal drag force comparisons between the tow tank measurements and finite element simulations for aligned and perpendicular towing tests are shown in Fig. 2.6 (the tests correspond to the representative velocities shown in Fig. 2.3). It can be seen that, in general, the simulations reproduce the tow test measurements. However, there are several distinctions. First, the drag output in numerical simulations has less noise than in the experimental tow drag force measurements. Second, the numerical models converge to steady-state condition faster for all towing velocities. These effects partially occur due to the smoothed velocity input used in the numerical simulations since the simulations with the unfiltered velocity data produced a more substantial noise and a longer convergence time. Third, the actual tow tests demonstrated higher drag force peaks when shifting from one towing velocity mode to another. This phenomenon could be attributed to the local nonlinear hydrodynamic effects that are not considered in the Morison approach since the changes in finite element model inertia, such as increasing added mass coefficient C_a, had negligible impact on the force peaks.

Horizontal drag forces and inclination angles averaged over all tow tests, as well as the result of the corresponding numerical simulations for each towing velocity, are presented in Fig. 2.7, 2.8. The proposed numerical model captures the physical aggregate response with the mean differences in terms of inclination angles (over all *5* towing velocities) of *3%* and *7%* for aligned and perpendicular orientations, respectively. The mean horizontal drag force difference for aligned and perpendicular orientation are *3%* and *10%*.

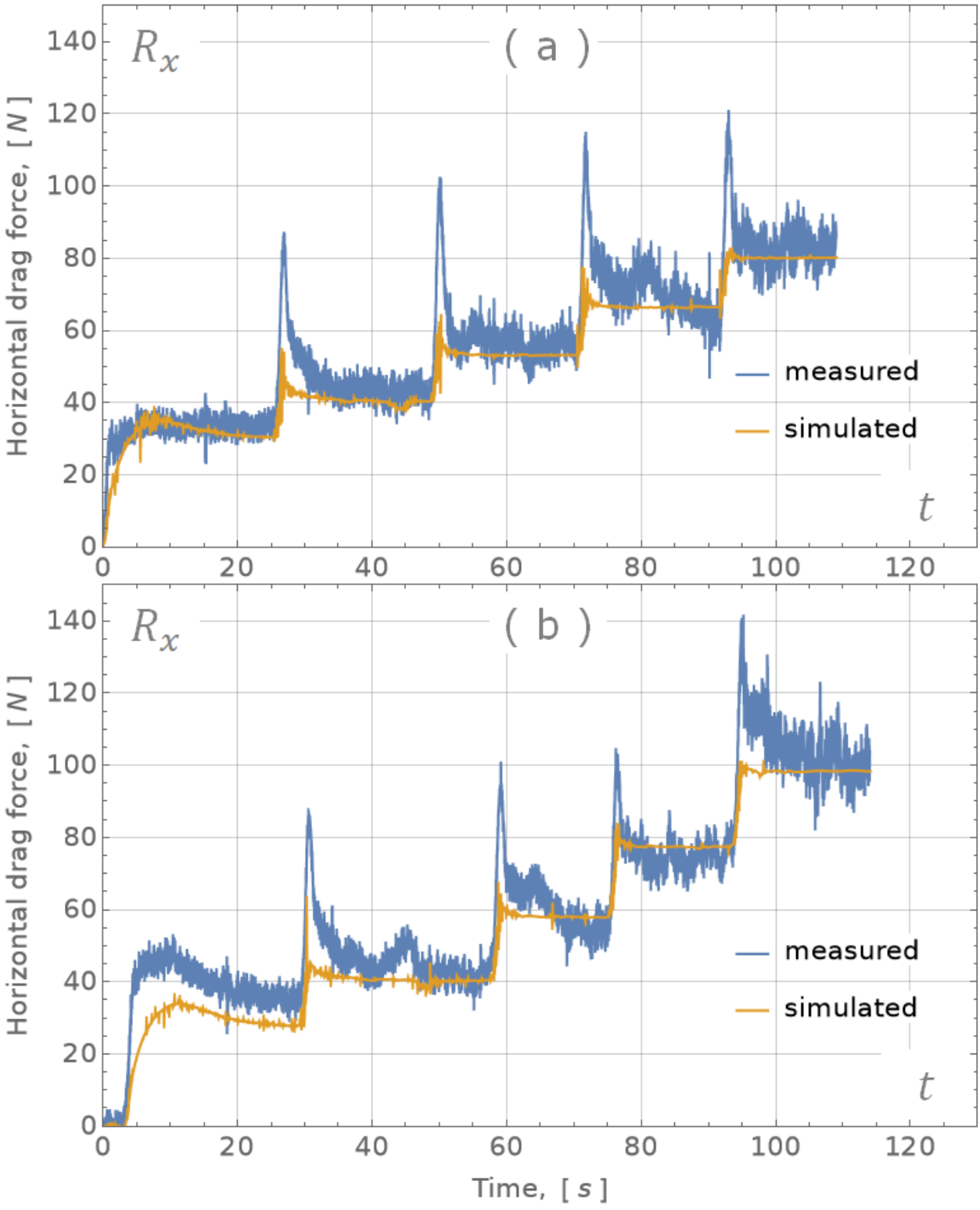

Fig. 2.6. Measured and simulated horizontal drag force for representative (a) aligned and (b) perpendicular kelp aggregate tests.

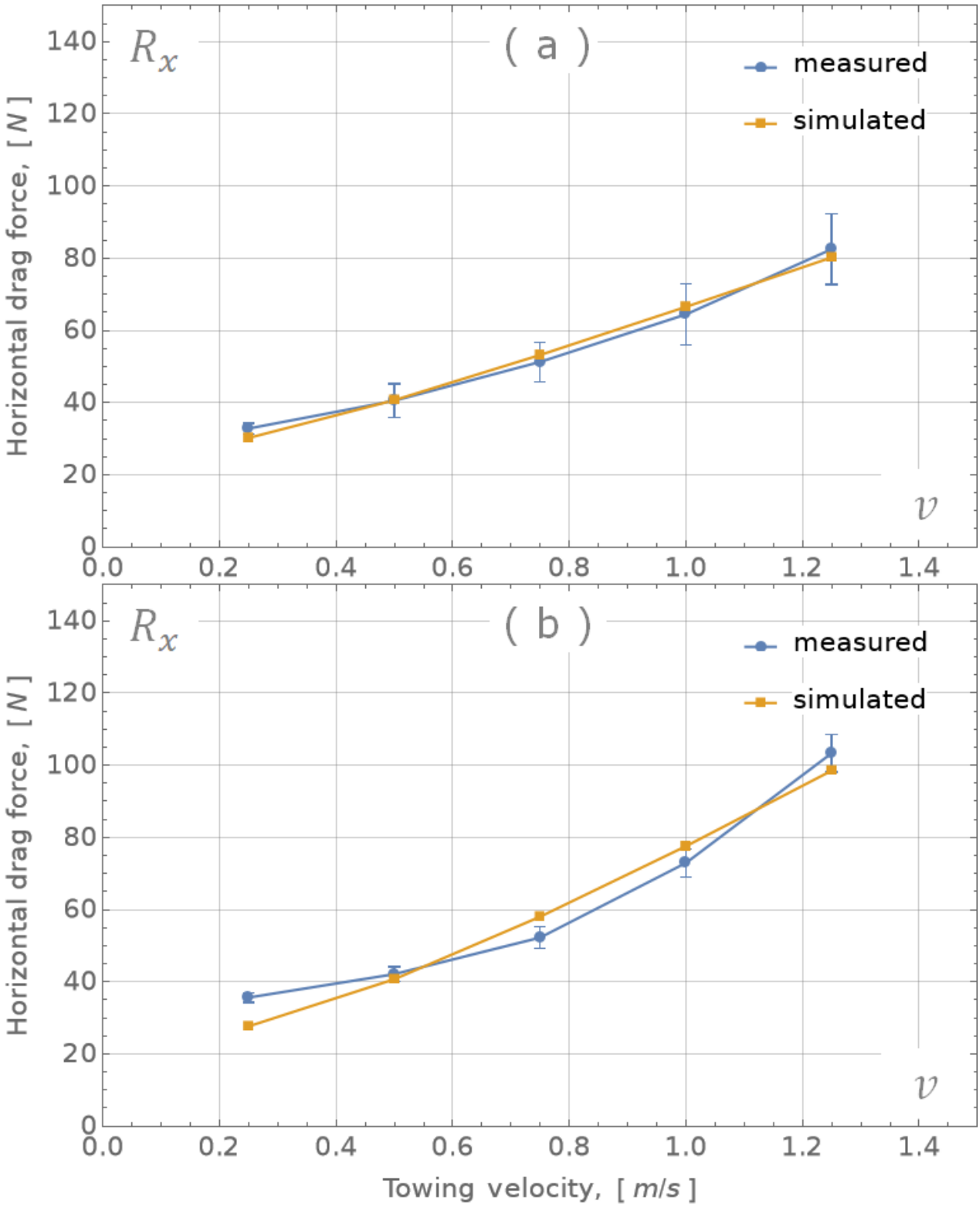

Fig. 2.7. Measured and simulated horizontal drag forces for (a) aligned and (b) perpendicular kelp aggregate tests. The 99% confidence intervals for the measured drag force are presented.

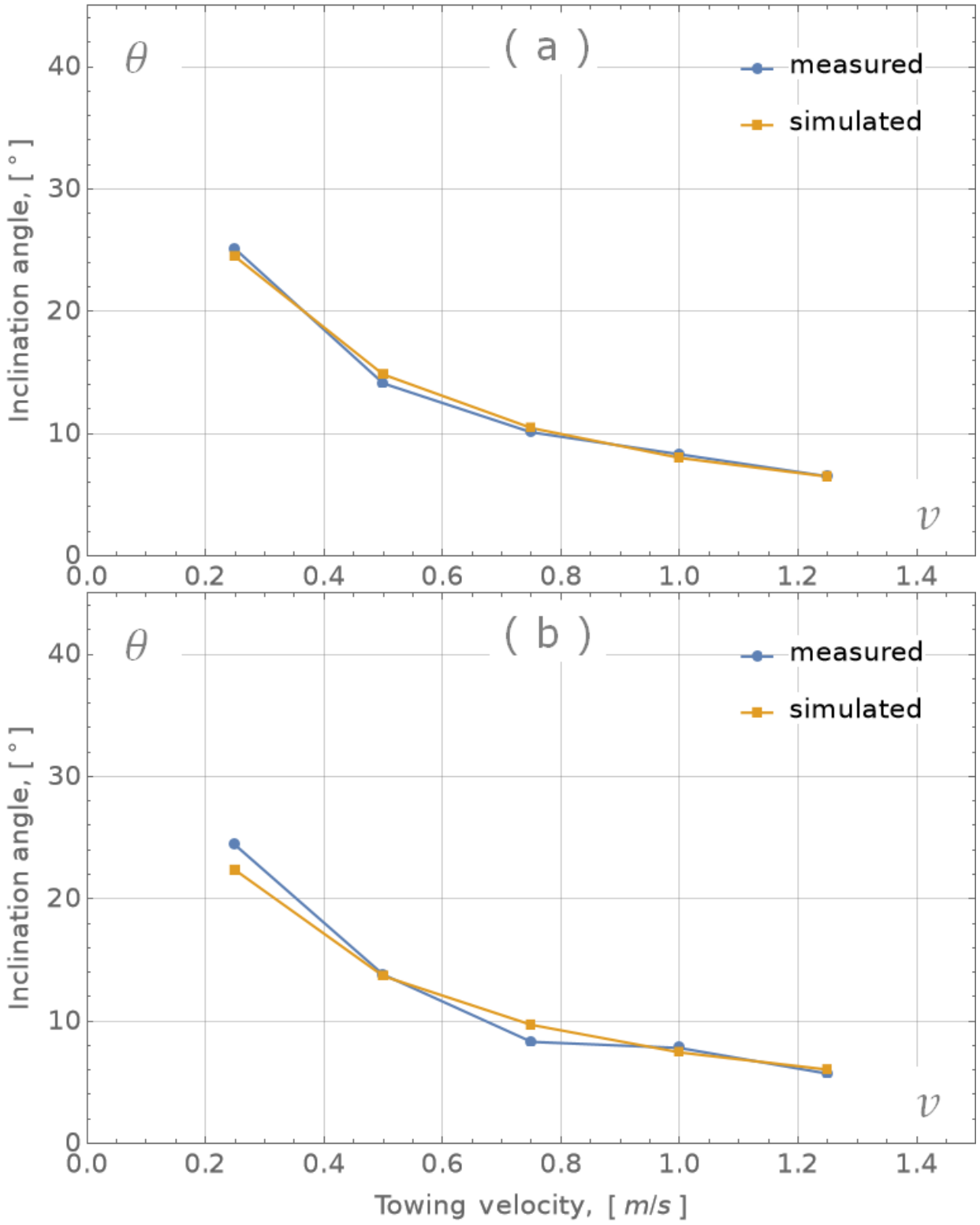

Fig. 2.8. Measured and simulated inclination angles for (a) aligned and (b) perpendicular kelp aggregate tests.

The *10%* difference in horizontal drag force in perpendicular orientation is mostly due to the drag discrepancy of about *25%* for the lowest towing velocity test, while the rest of the tests produce discrepancy of about *6%*. This is caused by the simplicity of drag approximation model (2.3) discussed in Section 3.2.

Note that inclination angles of about *22-25°* for the lowest towing velocity of *0.25 m/s* and about *5-7°* for the highest towing velocity of *1.25 m/s* were observed in all tow tests and simulations (*65-68°* and *83-85°* from the vertical axis, respectively).

5. Conclusions

Numerical modeling of macroalgae farms presents unique challenges associated with kelp compliance, dense growth, and kelp being close to neutrally buoyant. In this paper, a finite element representation of densely grown kelp for dynamic structural simulations of aquaculture systems is proposed. Kelp arrangements of the systems are subdivided into finite number of kelp aggregates that are then presented as equivalent kelp-elements, similar to the consistent net-elements designed for fishing nets or equivalent dropper-elements designed for mussel longlines. The kelp-element approach replicates the hydrostatic, hydrodynamic, and structural properties of the aggregate, while improving computational performance for large-scale system simulations.

The approach utilizes modified Morison-type equations where drag coefficients are adjusted to better represent hydrodynamic response of the aggregate subjected to environmental loadings. The kelp-element technique is implemented in *Hydro-FE* software and calibrated with the tow tests of full-scale physical kelp aggregate model conducted in the Hydromechanics Laboratory at the United States Naval Academy. The model represented *Saccharina latissima* kelp aggregate

response to towing velocities from *0.25 m/s* to *1.25 m/s* in orientations aligned and perpendicular to the tow direction.

It is shown that the proposed kelp-element numerical model is capable of capturing the physical kelp aggregate response observed in the tow tank tests. The mean differences in inclination angles over all towing velocities in aligned and perpendicular orientations are of *3%* and *7%*, respectively, while the corresponding differences in terms of the horizontal drag force are of *3%* and *10%*. It is also shown that the model performance is not sensitive to a particular choice of the added mass coefficient and does not require significant mesh refinement. Thus, the proposed numerical technique can be used in combination with the measured kelp species properties to model large-scale macroalgae aquaculture systems with sufficient accuracy.

Chapter III

Methodology for multidimensional approximation of current velocity fields around offshore aquaculture installations

This chapter was published as *Knysh, A., Drach, A., Fredriksson, D., Dewhurst, T. and Tsukrov, I., 2022. Methodology for multidimensional approximation of current velocity fields around offshore aquaculture installations. Aquacultural Engineering, 99, p.102284.*

My contribution to the paper was development and implementation of the multidimensional current velocity approximation technique in *Hydro-FE* software. I processed acoustic Doppler current profiler data sets to be used as input for the simulations of kelp longline dynamic response. I also prepared the first draft of the manuscript for publication.

Abstract

Consistent growth of the marine aquaculture industry over the past decades calls for potential deployments of large-scale aquaculture structures to produce finfish, shellfish and macroalgae in varying inshore and offshore environments. Numerical simulations for engineering design applications become more challenging with increase of scale since current velocity fields are no

longer uniform, complicating accurate hydrodynamic load calculations. Horizontal and vertical velocity profiles in this case are spatially (depth and particular location within the deployment site) and temporary (date and time) dependent. Thus, proper representation of the current velocity field in numerical models becomes crucial for accurate predictions of structural performance of aquaculture installations.

In this paper, an advanced multidimensional approximation method based on discrete current velocity data is formulated. The approach implies presenting the continuous current velocity function as a superposition of weighted radial basis functions extended by a linear polynomial. To address overfitting issues, the thin plate regularization is applied in the method. The approximation is then constrained in order to fit the velocity values on the domain boundaries. The method is implemented in finite element software *Hydro-FE* and its performance is compared to other approximation methods on the example of a kelp grow line deployed at the Wood Island research site, Maine, USA. It was found that the difference between regular (mean or linearly interpolated) velocity profiles and the velocity profiles approximated with the radial basis function method can reach up to 34-38% in terms of grow line mooring tensions, and 6-18% in terms of grow line displacement.

1. Introduction

Aquaculture is one of the fastest growing industries and the fastest growing food sectors in the world due to increasing consumer demand in seafood, kelp and other aquaculture products (Gentry et al., 2017). To satisfy this demand, sustainable production needs to expands to inshore and offshore sites around the world that can be safely exploit/maintained from ecological and

economical points of view (Fairbanks, 2016). Large-scale aquaculture deployments such as fish farms with multiple net pens, shellfish or kelp farm structures has garnered considerable attention from researchers in this context (Asche et al., 2018).

As economics of scale show profitability, adequate numerical estimate of structural performance becomes a crucial factor for successful deployment, especially in high tidal currents and potential storm events. Thus, numerous studies have been conducted providing numerical predictions based on the appropriate field data sets. For instance, numerical modeling of the Broad Cove fish farm located in Maine, USA, was performed in finite element software *Aqua-FE* using current velocity measured by several current meters kept about *4 m* below the water surface (Fredriksson et al., 2007). Similar investigations have also been conducted in Europe, where response of a large circular sea cages near the Faroe Islands was modeled in *FhSim* software developed by SINTEF Fisheries and Aquaculture, Norway (Klebert et al., 2015; Winthereig-Rasmussen et al., 2016). Volume change of one of the cages as well as forces applied on it were estimated through computational fluid dynamics analysis with current profiles recorded by acoustic doppler current profiler (ADCP) placed outside and inside of the cage. Another example is modeling of typical mussel longline system with the backbone that supports long V-shaped mussel collector lines. The behavior of the longline located near Belgian North Sea was simulated with lumped-mass open-source code *MoorDyn* and compared with the commercially available *OrcaFlex* software (Pribadi et al., 2019). Currents were implemented as a uniform velocity field over the whole simulation domain. Numerical studies performed with other specialized software, such as *DUT-FlexSim* (Zhao et al., 2015; Bi et al., 2020), *SimuTrawl* (Nguyen and Winger, 2016; Thierry et al., 2019), etc., also assumed uniform velocity profiles.

While most of the existing numerical studies assume that incident horizontal and vertical velocity profiles are the same within the entire simulation domain, this is not necessarily true for most of the large-scale applications. For this reason, some ocean engineering software products implement advanced options to input velocity fields. *OrcaFlex* introduces vertical and horizontal current variations given as a magnitude with dimensionless multiplicative factor, external function that depends on spatial/time variables or interpolated data set. The user-defined data set can be interpolated with one of three methods: linear, cubic spline, cubic Bessel. *ProteusDS* allows user to initialize uniform and linear shear current profiles, power law current profile commonly used in tidal channels, custom current profile that depends on time and depth only, and three-dimensional spatially varying current profile where intermediate velocity values are obtained with three-dimensional interpolation scheme. In terms of the current velocity field accuracy, these and other software packages are limited to interpolation of user-defined current velocity data. Even though it is suitable for some applications, single- and multidimensional interpolations can fail to produce adequate interpolant due to overfitting (Smith et al., 1998).

In this paper an advanced approach to compose a smooth and accurate multidimensional approximation of the current velocity field is proposed, where the velocity function is taken as a superposition of weighted radial basis function extended by linear polynomial. The method is described in details in Section 2. Current data acquisition for the approximation method are discussed in Section 3. The section also describes acquisition of the actual current velocity field data on the example of acoustic wave and current profilers at the University of New England (UNE) Wood Island research site, Maine, USA. Sections 4 is dedicated to simulations of a *Sacchrina latissisma* kelp farm deployed at the site with the finite element software *Hydro-FE*. The simulations are performed for the method proposed in this paper as well as for other current

approximation techniques. Results are then discussed and compared in terms of kelp mooring tensions and grow line displacements. Conclusions are presented in Section 5.

2. Approximation of current velocity field using radial basis functions

Large-scale aquaculture installations often occupy substantial offshore sites where current velocities can vary considerably, depending on location and depth within the site, and changing with time. Therefore, the velocity data (usually provided in the form of scattered data points, as discussed in Section 3) must be approximated in space and time to make predictions on performance of the installations in spatially and temporally changing environmental conditions. By proper approximation, it is assumed such current velocity fields that are sufficiently smooth and accurate for meaningful numerical predictions.

The approximation method proposed in this paper is based on the concept of the radial basis function (RBF) interpolation (Majdisova and Skala, 2017) and has several advantages in approximating of current velocity fields. First, RBF interpolation is easily formulated, generalized and implemented for the input data of almost any dimension. Second, stability and good convergence properties of the method have been observed even in high-dimensional problems. Finally, RBF interpolation is a mesh-free method and is suitable for irregular spatial grid, meaning the points in the domain do not need to lie on a structured grid (Wendland, 2005).

2.1 Radial basis function interpolation

With the RBF interpolation method, the current velocity field $f(\mathbf{x})$ is obtained from n scattered data points such that $f(\mathbf{x}_i) = f_i,\ i = 1, \dots, n$, where $\mathbf{x}$ is the d-dimensional coordinate of the arbitrary point, $\mathbf{x}_i = (x_{i1}, x_{i2}, \dots, x_{id})$ is the coordinate of the scattered point i, and f_i is the value of current velocity at the point i. The number of dimensions d can include up to three spatial and one time variables, while the scalar function f is one of three current velocity projections on a spatial coordinate axes. The RBF interpolant, $f(\mathbf{x})$, is presented as a weighted sum of radial basis functions φ and often extended by a low-degree polynomial of vector of variables $\mathbf{x}$ to improve fitting accuracy and extrapolation away from the data points (Holmström, 2008). Utilizing a linear polynomial, the representation of $f(\mathbf{x})$ becomes:

$$f(\mathbf{x}) = \sum_{i=1}^{n} a_i \varphi(\|\mathbf{x} - \mathbf{x}_i\|_2) + \mathbf{b}^{\mathrm{T}}\mathbf{x} + c \tag{3.1}$$

where $\|\cdot\|_2$ is the Euclidian norm or the length of a vector. Weights $a_1, a_2, \dots, a_n$, vector of coefficients $\mathbf{b} = (b_1, b_2, \dots, b_d)^{\mathrm{T}}$ and the constant c are unknown, but can be found from the system of linear equations (SLE)

$$\begin{pmatrix} \varphi_{11} & \varphi_{21} & \cdots & \varphi_{n1} & x_{11} & x_{12} & \cdots & x_{1d} & 1 \\ \varphi_{12} & \varphi_{22} & \cdots & \varphi_{n2} & x_{21} & x_{22} & \cdots & x_{2d} & 1 \\ \vdots & \vdots & \ddots & \vdots & \vdots & \vdots & \ddots & \vdots & \vdots \\ \varphi_{1n} & \varphi_{2n} & \cdots & \varphi_{nn} & x_{n1} & x_{n2} & \cdots & x_{nd} & 1 \\ x_{11} & x_{21} & \cdots & x_{n1} & 0 & 0 & \cdots & 0 & 0 \\ x_{12} & x_{22} & \cdots & x_{n2} & 0 & 0 & \cdots & 0 & 0 \\ \vdots & \vdots & \ddots & \vdots & \vdots & \vdots & \ddots & \vdots & \vdots \\ x_{1d} & x_{2d} & \cdots & x_{nd} & 0 & 0 & \cdots & 0 & 0 \\ 1 & 1 & \cdots & 1 & 0 & 0 & \cdots & 0 & 0 \end{pmatrix} \begin{pmatrix} a_1 \\ a_2 \\ \vdots \\ a_n \\ b_1 \\ b_2 \\ \vdots \\ b_d \\ c \end{pmatrix} = \begin{pmatrix} f_1 \\ f_2 \\ \vdots \\ f_n \\ 0 \\ 0 \\ \vdots \\ 0 \\ 0 \end{pmatrix} \tag{3.2}$$

written in the symbolic matrix notations as

$$\mathbf{\Phi w} = \mathbf{F} \tag{3.3}$$

where $\varphi_{lm} = \varphi_{ml} = \varphi(\|\mathbf{x}_l - \mathbf{x}_m\|_2)$. Known conditions $f(\mathbf{x}_i) = f_i,\ i = 1, \dots, n$, represent the first n equations of the system, while last $d + 1$ equations are additional constraints on weights. Solving SLE (3.3) results in components of vector $\mathbf{w} = \mathbf{\Phi}^{-1}\boldsymbol{F}$ such that the interpolating function passes through all data points f_i. However, this RBF interpolation can lead to data overfitting. Fig. 3.1 shows an example of a typical overfitting of power-law-like function $p(x) = 7x^{1/7}$ on regular data grids. This particular function was selected because it is often used by oceanographers to characterize average tidal velocity profiles (Lewis et al., 2017). The thin plate basis $\varphi(r) = r^2 \log r$ was chosen in this case, but numerical experiments showed that changing basis to cubic, multiquadric and Gaussian forms do not resolve the overfitting issue, justifying the development of another approach.

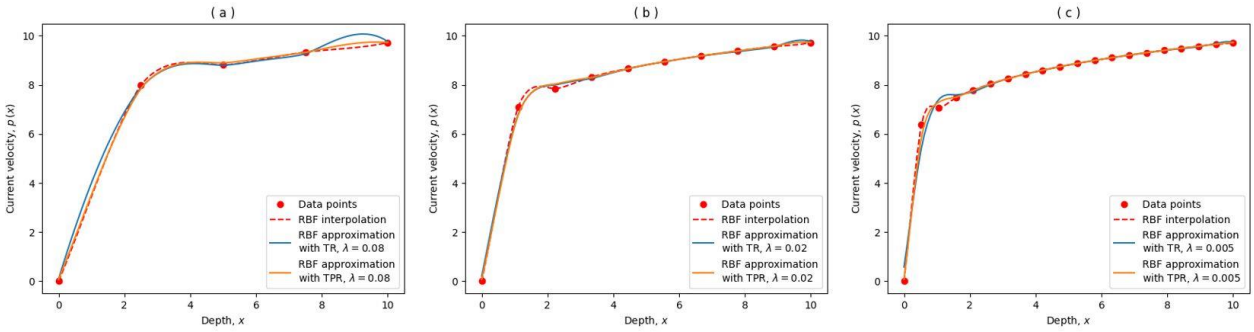

Figure 3.1. Example of power law profile $p(x) = 7x^{1/7}$ approximations on the (a) 5-point, (b) 10-point and (c) 20-point regular grids with thin plate basis.

Note that the approximation in this example is one-dimensional as it depends on variable x only. For multidimensional interpolations and approximations in this paper, regular grids were

additionally rescaled to unit intervals between data points in each dimension to prevent gradient-related distortion of the resulting approximating function.

2.2 Radial basis functions approximation with Tikhonov regularization

The classic approach to address under- or overfitting and to control the interpolant capacity is to extend the hypothesis space by widening the class of functions representing the interpolant. This step was employed in equation (3.1) with the addition of a linear polynomial to the basic RBF interpolant. However, this approach is not universal since the nature of the data is not always known *a priori*.

Therefore, the under- and overfitting issues are addressed through regularization, another powerful tool to control the interpolant capacity. In the process of regularization, problem (3.3) is reformulated in optimization terms. Instead of solving the SLE, it is now required to find such a vector of weights $\mathbf{w}$ that minimizes the following cost function J:

$$J(\mathbf{w}) = \|\mathbf{\Phi w} - \mathbf{F}\|_2^2 \tag{3.4}$$

This is also known as the linear least squares problem. If $\mathbf{w}$ makes cost function $J(\mathbf{w})$ equal to zero, then it is the solution of the initial SLE described in equation (3.3). An objective of regularization is to modify the cost function to regulate properties of the resulting approximation. For example, one typical regularization technique, Tikhonov regularization (TR), changes cost function to

$$J(\mathbf{w}) = \|\mathbf{\Phi w} - \mathbf{F}\|_2^2 + \lambda \mathbf{w}^{\mathrm{T}}\mathbf{w} \tag{3.5}$$

where positive parameter λ multiplied by regularizer $\mathbf{w}^{\mathrm{T}}\mathbf{w}$ provides a compromise between fitting the data and applying weights on fewer features. Although advanced techniques beyond the manual tuning of parameter λ exist (Hutter et al., 2015), our preliminary numerical experiments show that $\lambda = (d+1)/n^{2/d}$ provides a reasonable balance between smoothness and accuracy of the current velocity field, so it is utilized in the approximations applied in Section 4. The minimization problem (3.5) can be solved with matrix calculus, assuming that the cost function gradient is zero (Goodfellow et al., 2016):

$$\mathbf{w} = (\mathbf{\Phi}^{\mathrm{T}}\mathbf{\Phi} + \lambda \mathbf{I})^{-1}\mathbf{\Phi}^{\mathrm{T}}\mathbf{F} \tag{3.6}$$

where **I** is the identity matrix. It can be seen in Fig. 3.1b,c that the TR method somewhat smooths out the overfitting between second, third and fourth data points, however the regularization tends to distribute weights in a way that produces curve kinking, similar to the one between the last data points to the right in Fig. 3.1a,b and the first points to the left in Fig. 3.1c. The fitting issue occurs regardless of value of parameter λ, meaning that another regularization technique must be used.

2.3 Radial basis function approximation with thin plate regularization

Even though TR generally smooths the approximation functions, its performance is limited in regions of high convexity. Therefore, a regularization approach that utilizes the absolute values of second derivatives to restrict their growth is required. One of such approaches, known as thin plate

regularization (TPR), refers to a physical analogy with energy due to bending of a thin plate. It was originally formulated for the function of two variables $f(x, y)$ as follows:

$$\lambda \int_D \left[\left(\frac{\partial^2 f}{\partial x^2} \right)^2 + 2 \left(\frac{\partial^2 f}{\partial x \partial y} \right)^2 + \left(\frac{\partial^2 f}{\partial y^2} \right)^2 \right] dx dy \tag{3.7}$$

where D is the domain of the function and the parameter λ is the so-called rigidity measure. The whole integral in (3.7) is also known as the thin plate energy functional. The expression within the integral is the sum of all possible squared second derivatives, so it can be generalized for an arbitrary multivariate function $f(\mathbf{x})$:

$$\lambda \int_D [\mathbf{e}^{\mathrm{T}} (\mathbf{H}f \odot \mathbf{H}f) \mathbf{e}] \, d\mathbf{x} \tag{3.8}$$

where $\mathbf{H}f$ is the Hessian matrix of $f(\mathbf{x})$, $\mathbf{e}$ is the vector of ones, and $\odot$ is the Hadamard product (the element-wise matrix product). The product of Hessian matrices produces the symmetric matrix of the squared second derivatives and the multiplication by vectors of ones is used to obtain their sum.

If we now substitute function (3.1) into (3.8), a quadratic form of components $\mathbf{w}$ is obtained. It is known that this quadratic form can be presented as the product

$$\lambda \mathbf{w}^{\mathrm{T}} \mathbf{Q} \mathbf{w} \tag{3.9}$$

where $\mathbf{Q}$ is the symmetric matrix of the quadratic form coefficients. The cost function $J(\mathbf{w})$ corresponding to the thin plate regularization then becomes

$$J(\mathbf{w}) = \|\mathbf{\Phi w} - \mathbf{F}\|_2^2 + \lambda \mathbf{w}^{\mathrm{T}} \mathbf{Q} \mathbf{w} \tag{3.10}$$

To minimize (3.10), the cost function gradient is assumed to be zero and solved for $\mathbf{w}$ using matrix calculus:

$$\mathbf{w} = (\mathbf{\Phi}^{\mathrm{T}}\mathbf{\Phi} + \lambda\mathbf{Q})^{-1}\mathbf{\Phi}^{\mathrm{T}}\mathbf{F} \tag{3.11}$$

Elements of the matrix $\mathbf{Q}$ depend on the choice of RBF, which also influences behavior of the approximation. In practice, typical RBF choices have a cubic basis such that $\phi(r) = r^3$ and with the thin plate basis of, $\phi(r) = r^2 \log r$. The thin plate basis was used since it minimizes the thin plate energy functional (3.8), however it does not mean that changing λ does not impact the resulting approximation.

2.4 Constrained optimization

Even though TPR resolves some of the TR fitting issues, the technique does not fit the boundary points well as shown on Fig. 3.1c. For this reason, the TPR approximations were constrained with additional equality conditions that require the values of approximating function at the boundary points to be equal to their values in the initial data set (Dirichlet boundary conditions). Thus, the TPR optimization problem

$$\min_{\mathbf{w}} J(\mathbf{w}), \quad J(\mathbf{w}) = \|\mathbf{\Phi}\mathbf{w} - \mathbf{F}\|_2^2 + \lambda\mathbf{w}^{\mathrm{T}}\mathbf{Q}\mathbf{w} \tag{3.12}$$

becomes

$$\min_{\mathbf{w}\in\mathbb{C}} J(\mathbf{w}), \quad \mathbb{C} = \{\, \mathbf{w} \mid \|\mathbf{\Phi}_{\mathrm{c}}\mathbf{w} - \mathbf{F}_{\mathrm{c}}\|_2^2 = 0 \,\} \tag{3.13}$$

where $\mathbf{\Phi}_{\mathrm{c}}$ and $\mathbf{F}_{\mathrm{c}}$ are composed of the rows of $\mathbf{\Phi}$ and $\mathbf{F}$, respectively, that correspond to the set of constrained points. To solve the constrained problem described in (3.13), it is reduced to an unconstrained optimization problem using the method of Lagrange multipliers. This approach introduces a new cost function called the generalized Lagrangian,

$$L(\mathbf{w},\mu) = \|\mathbf{\Phi w} - \mathbf{F}\|_2^2 + \lambda \mathbf{w}^{\mathrm{T}}\mathbf{Q w} + \mu\|\mathbf{\Phi}_{\mathrm{c}}\mathbf{w} - \mathbf{F}_{\mathrm{c}}\|_2^2 \tag{3.14}$$

solving the unconstrained optimization problem, equivalent to the one formulated in (3.13):

$$\min_{\mathbf{w}} \max_{\mu} L(\mathbf{w},\mu) \tag{3.15}$$

where μ is a scalar parameter. To resolve (3.15), the Lagrangian is minimized with respect to $\mathbf{w}$ requiring $\nabla_{\mathbf{w}} L(\mathbf{w},\mu) = 0$. The solution can be derived using matrix calculus as follows:

$$\mathbf{w}(\mu) = (\mathbf{\Phi}^{\mathrm{T}}\mathbf{\Phi} + \lambda\mathbf{Q} + \mu\mathbf{\Phi}_{\mathrm{c}}^{\mathrm{T}}\mathbf{\Phi}_{\mathrm{c}})^{-1}(\mathbf{\Phi}^{\mathrm{T}}\mathbf{F} + \mu\mathbf{\Phi}_{\mathrm{c}}^{\mathrm{T}}\mathbf{F}_{\mathrm{c}}) \tag{3.16}$$

The maximization of μ is obtained by equating the first derivative of the Lagrangian (3.14) with respect to μ to zero:

$$\frac{\partial L}{\partial \mu} = \|\mathbf{\Phi}_{\mathrm{c}}\mathbf{w} - \mathbf{F}_{\mathrm{c}}\|_2^2 = 0 \tag{3.17}$$

In this process, the value of parameter μ is chosen such that the corresponding $\mathbf{w}(\mu)$ in (3.16) satisfies (3.17). From the numerical standpoint, this could be resolved, for example, by performing a gradient ascent on μ. To apply gradient ascent, step size ε, precision δ and initial value of μ are first chosen. Then, the initial value of $\mathbf{w}$ is calculated with (3.16). While $\|\mathbf{\Phi}_{\mathrm{c}}\mathbf{w} - \mathbf{F}_{\mathrm{c}}\|_2^2 > \delta$ is true, the parameter μ changes to $\mu + \varepsilon(\partial L/\partial\mu)$, and then new value of $\mathbf{w}(\mu)$ is recalculated with (3.16). This iterative process for μ and $\mathbf{w}(\mu)$ continues until $\|\mathbf{\Phi}_{\mathrm{c}}\mathbf{w} - \mathbf{F}_{\mathrm{c}}\|_2^2 \leq \delta$, when the final value of $\mathbf{w}$ is obtained.

The choice of step size ε influences the numerical performance of the gradient ascent since $\mathbf{w}(\mu)$ in (3.16) must be recalculated at each iteration of μ. Note that the set of boundary points for the irregular grid is found with the use of Delaunay triangulation and convex hull algorithms.

Final comparison between the constrained RBF approximation with TPR, the RBF approximation with TR and the RBF interpolation of power-law-like function is shown in Fig. 3.1. The constrained RBF approximation with TPR completely resolves the fitting issue. The constrained approximation also provides good extrapolation for points outside of the domain. However, the values of the approximation function at these points are assumed to be equal to the grid point values at the nearest boundary.

3. Acquisition of the current velocity field data

The approach developed in Section 2 can be utilized to predict structural response of aquaculture installations to environmental loading regimes varying in space and time. Data sets describing the velocity distribution for a chosen marine site can be obtained through numerical prognostic models or by actual field measurements. Both of these approaches are discussed in this section, however, only the field measurements are used in Section 4.

3.1 Numerical models

There are several known ocean dynamic models that can provide environmental data input for a chosen marine aquaculture site. For instance, the *Simulating WAves Nearshore* (SWAN) model, developed at Delft University of Technology, Netherlands, computes random, short-crested wind-generated waves in coastal regions and inland waters (Akpinar et al., 2012; Akpınar et al., 2016; Kutupoğlu et al., 2018; Liang et al., 2019). Another *Finite Volume Community Ocean Model* (FVCOM), developed by University of Massachusetts Dartmouth and Woods Hole Oceanographic

Institution joint efforts, is originally focused on flooding/drying process and the tidal-, buoyancy- and wind-driven circulation in the coastal region featured with complex irregular geometry and steep bottom topography (Chen et al., 2012). While other numerical models exist, FVCOM is of interest in the context of this paper since it is capable of producing discrete current velocity data sets.

FVCOM is an open-source code that consists of momentum, continuity, temperature, salinity and density equations and is closed physically and mathematically using turbulence closure submodels. This mathematical problem is then solved numerically by a discrete flux calculation in integral form of the governing equations over an unstructured triangular grid. This approach combines the advantages of finite-element methods (grid flexibility) and finite-difference methods (numerical efficiency and code simplicity), so the model is suitable for many coastal and interdisciplinary scientific applications (Chen et al., 2009, 2011; Qi et al., 2009). Numerical experiments have been performed to validate the non-hydrostatic FVCOM, including surface standing and solitary waves in idealized flat- and sloping-bottomed channels in homogeneous conditions, the density adjustment problem for lock exchange flow in a flat-bottomed channel, and two-layer internal solitary wave breaking on a sloping shelf (Lai et al., 2010). Benchmark test problems, such as Rossby equatorial soliton, the hydraulic jump, and the three-dimensional barotropic wind-driven basin, were performed to examine the properties of numerical dispersion and damping, the performance of the nonlinear advection scheme for supercritical flow conditions, and the accuracy of the implicit vertical viscosity scheme in barotropic settings, respectively (Huang et al., 2008).

Even though numerical models in general, and FVCOM in particular, are of use in marine science and ocean engineering, there are two limitations with respect to aquaculture operations.

These models may not be applicable or available for all marine sites that are of interest for aquaculture installations, and if they are, the validation process takes years to achieve an acceptable level of accuracy; the numerical models are usually applied on large scales, so obtaining detailed current velocity distribution at locations that are only tens/hundreds of meters away from each other can be challenging. For these reason, standard field current velocity measurements are still preferable for obtaining a reliable environmental data for a given aquaculture site.

3.2 Field measurements. Current velocity acquisition at Wood Island site

In-situ current velocity measurements can be obtained with acoustic Doppler current profilers (ADCP), buoys monitored through special tracking devices and even satellites (Dohan and Maximenko, 2010), etc. The measurements deliver reliable and detailed current/wave information which makes them convenient data source for comprehensive current velocity field approximations. Thus, the multidimensional (in space and time) current velocity approximation technique presented in this paper was investigated and validated with a detailed ADCP current velocity data set obtained at the UNE Wood Island kelp farm research site, Maine, USA. The dataset was collected from May 16 to May 28, 2019. To obtain velocity components of tidal currents at Wood Island site, two ADCPs (west and east) were placed *42 m* away from each other and *20-25 m* away from the kelp grow line. The grow line and the ADCPs were deployed along the major axis of the tidal ellipse (Fig. 3.2). This orientation of the grow line ensured the best performance of claw anchors and minimized obstruction to navigation while wave and turbulence

actions provided sufficient kelp nutrient concentration. The ADCPs used were *1 MHz* acoustic wave and current sensors manufactured by Nortek.

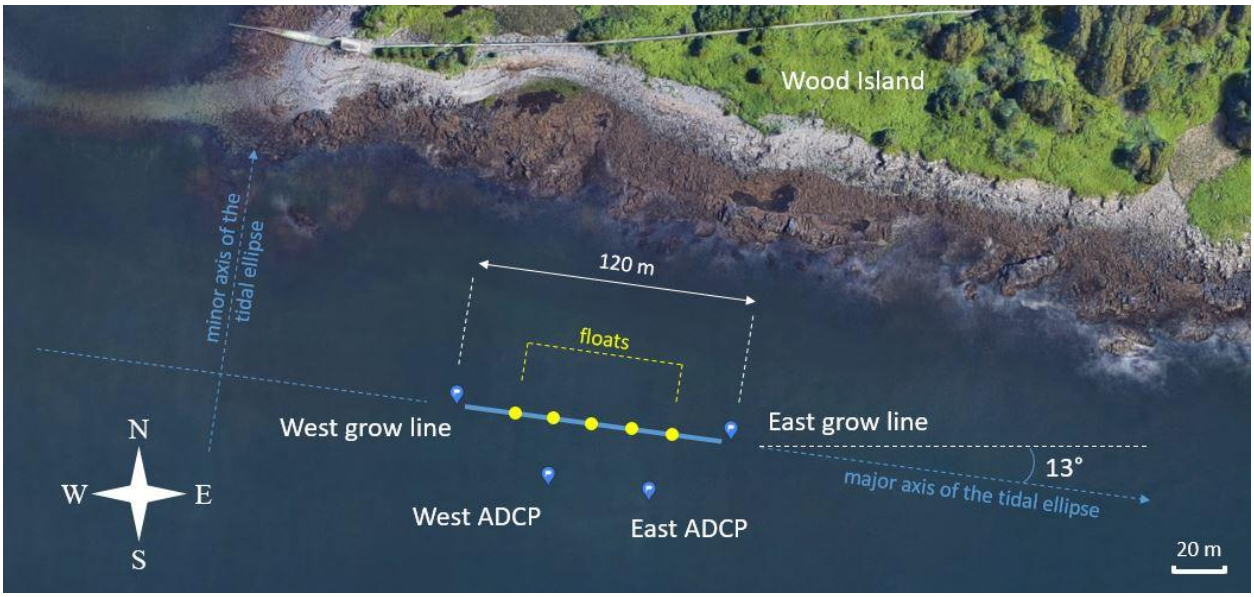

Figure 3.2. Kelp farm deployment at University of New England Wood Island site, Maine, USA. West grow line: 43°27'17.54"N, 70°20'16.69"W; East grow line: 43°27'17.05"N, 70°20'11.45"W; West ADCP: 43°27'16.41"N, 70°20'14.94"W; East ADCP: 43°27'16.20"N, 70°20'13.01"W.

Both ADCPs were installed *0.5 m* up above the bottom, each in a tripod frame with a configuration that incorporates a *0.4 m* blanking distance. The devices collected east-going, north-going and vertical components of current velocity at measurement points within the water column at *0.5 m* depth bins starting from *0.9 m* off the bottom to a maximum of *8.9 m* above the acoustic transducers (Fig. 3.3). The components were then projected on the major and minor axes of tidal ellipse, called major and minor axes hereafter, respectively, and averaged at 15 min time intervals (as *3 min* averages from *0-3, 15-18, 30-33* and *45-48 min* past each hour at *7 Hz* sampling rate).

Even though all three velocity components were measured, vertical component magnitudes were nearly zero during the whole monitoring time.

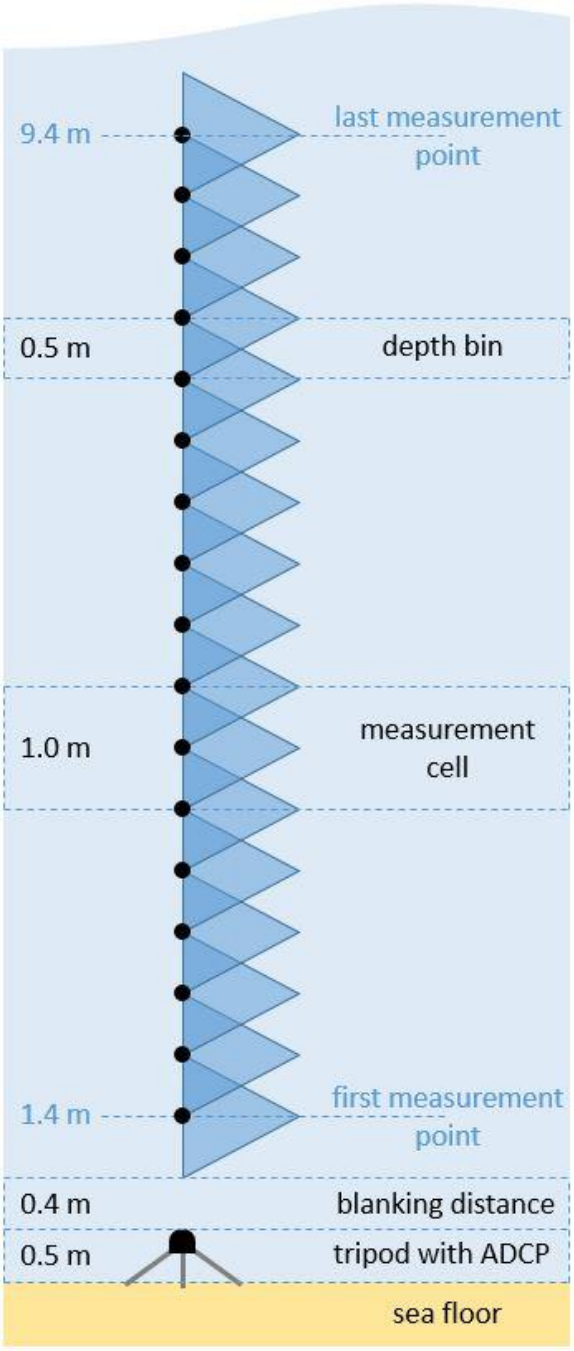

Figure 3.3. Schematics of west/east ADCP deployed at UNE Wood Island site, Maine, USA.

Fig. 3.4 shows three data samples of current profiles collected by the west and east ADCPs on May 16 (Fig. 3.4a), May 20 (Fig. 3.4b) and May 24, 2019 (Fig. 3.4c). The profiles were chosen for further numerical analysis and the velocity field approximations. These profiles were selected because they satisfy most of the following criteria: (1) absolute value of current velocity is high enough relative to other profiles; (2) west and east ADCP profile measurements were significantly different; (3) all other environmental measurements (water depth, wave height, wave period and wave direction) are available for the same time interval. Projection of currents on the major axis dominates in the sample profiles, however the minor axis component can also be high near the neutral water line (Fig. 3.4c). Note that the profile measurements from the west and east ADCPs were taken at slightly different depths due to the difference in sea level elevations that included tides (Table 3.1), so the final value of mean velocity was obtained by averaging the west and east ADCP mean velocities.

In addition to the current velocity profiles, both east and west ADCPs were utilized in wave measuring mode to obtain pressures, velocities, and acoustic surface tracking (AST) characteristics. These parameters were acquired in bursts and processed to obtain time series, statistical, spectral, and directional wave information (Krogstad, 1988; Pedersen and Nylund, 2004; Siegel et al., 2006; Siegel, 2007; Pedersen and Siegel, 2008). The bursts were set to begin following each velocity profile measurement. Dynamic pressures and wave orbital velocities were sampled at *2 Hz* for 1024 counts. AST data were measured at *4 Hz* for 2048 counts, each for a duration of *8 min* and *32 s* to fit between velocity profile acquisitions (each for *512 s*).

The wave datasets were then processed with the instrument software based on the Maximum Likelihood Method (Krogstad, 1988) modified for use with surface tracking (Pedersen and Nylund, 2004) to obtain wave spectral parameters such as the energy-based significant wave height

and peak periods. The software also determined the average height of the top 1/3 waves from each surface-track time series.

Table 3.1. Environmental data samples registered at (a) 16:00 on May 16, (b) 20:00 on May 20, (c) 23:15 on May 24, 2019, GMT-4. Wave directions are degrees from true north.

Date sample		**May 16**	**May 20**	**May 24**
Significant wave height, [m]	West ADCP	0.23	0.32	0.22
	East ADCP	0.27	0.33	0.25
Significant wave period, [s]	West ADCP	11.40	6.10	6.41
	East ADCP	11.13	5.93	6.52
Wave direction, [°]	West ADCP	140.63	135.60	149.95
	East ADCP	122.36	136.39	132.67
Water depth, [m]	West ADCP	7.71	7.18	7.26
	East ADCP	8.44	7.90	7.98
Mean velocity, [m/s]	X-direction	0.18	0.20	0.13
	Y-direction	-0.07	-0.06	-0.05

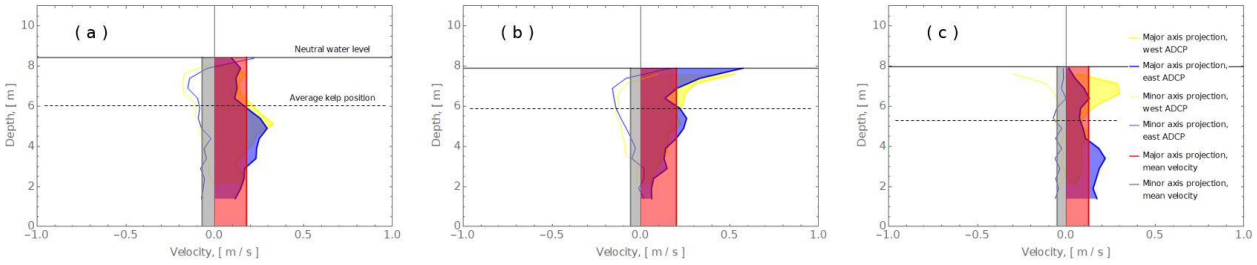

Figure 3.4. Sample current profiles registered at (a) 16:00 on May 16, (b) 20:00 on May 20, (c) 23:15 on May 24, 2019, GMT-4.

Water depth variations, significant wave height (average height of top 1/3 waves), significant wave period and wave propagation direction were obtained and averaged over *15 min* time intervals to synchronize them with the current velocity data, see Fig. 3.5. It can be seen that the significant wave height and significant wave period graphs for west and east ADCPs are almost identical (Fig. 3.5a,b), while the water depth varies due to a *0.7 m* difference in sea floor level (Fig. 3.5d). The wave propagation direction demonstrated overall consistency being about *135*° from true north except for the minor data noise between May 21 and May 24 (Fig. 3.5c). Mean velocity projections on major and minor axes are shown in Fig. 3.5e.

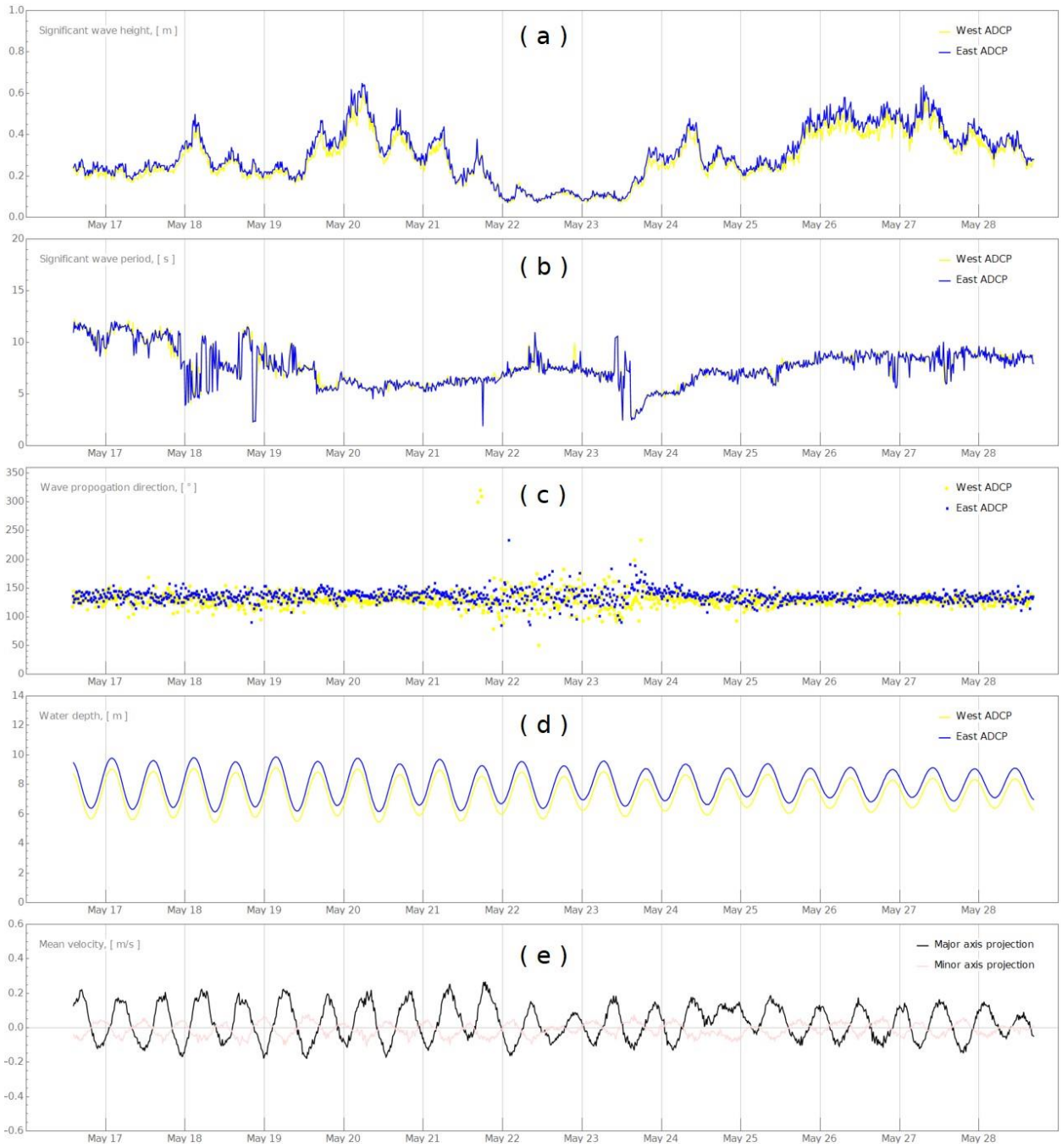

Figure 3.5. Values of (a) significant wave height, (b) significant wave period, (c) wave direction, (d) water depth and (e) mean velocity registered by west and east ADCPs at UNE Wood Island site from May 16 to May 28, 2019. Wave propagation direction are degrees from true north. The west and east ADCP measurements are shown in yellow and blue, respectively.

4. Numerical simulations of the Wood Island kelp farm

4.1 Finite element model

The current velocity field approximation methodology presented in Section 2, was tested on the example of a kelp farm installed at the Wood Island research site in spring 2019. The *120 m* long and *8 m* high kelp farm was supported by two corner floats of *14.5 kg* buoyancy with six intermediate floats of *4.5 kg* buoyancy each (Fig. 3.6). The intermediate floats were equally distributed along the *60 m* grow line in groups of two. Both grow and mooring lines were *1.2 cm* in diameter nylon lines and were attached to *4.5 m* long mooring chain at *20 kg* that provided dampening to prevent snap of mooring lines and and apply horizontal loading on the *30 kg* steel claw anchors. Note that the buoys were attached to the grow line by nylon lines inside of polyvinyl (PVC) pipe to keep the kelp at a depth of *2 m*. The grow line was oriented parallel to the major axis of the tidal ellipse for the best performance of the claw anchors.

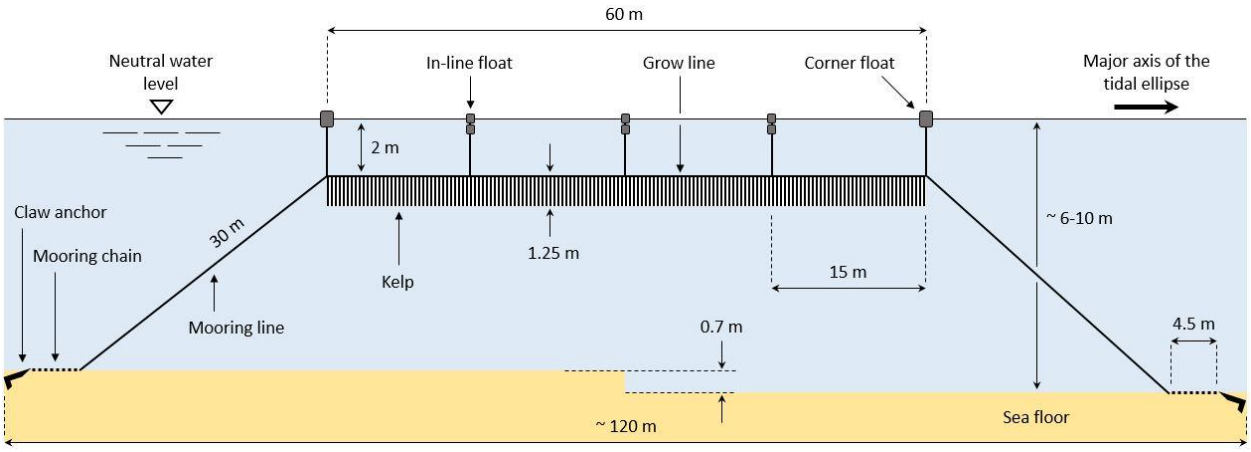

Figure 3.6. Schematics of the Wood Island kelp farm. Not to scale.

To obtain properties of the kelp required for finite element analysis, the Wood Island kelp farm was inspected seven times from May 16 to May 28, 2019. During each of the inspections, the weight, volume, length (blade and stipe) and width (blades) of the kelp were measured at three points along the grow line. The measured data sets were averaged and produced *1.25 m* long kelp that was assumed to be uniformly distributed along the grow line. The kelp was simulated using a technique similar to the "equivalent dropper approach" (Knysh et al., 2020) with the hydrodynamic characteristics (normal and tangential drag coefficients) taken from full-scale physical tests on dense aggregate of kelp blades (Fredriksson et al., 2020). The kelp elements were assigned the normal and tangential drag coefficients of *1.7* and *0.0577*, respectively. For all other components of the farm, the coefficients were set at *1.2* and *0.01*.

Finite element model of the kelp farm was built in *Hydro-FE* software developed from the well-validated *Aqua-FE* program developed at the University of New Hampshire (Gosz et al., 1996; Fredriksson et al., 2000; Tsukrov et al., 2000). The FORTRAN code of *Hydro-FE* uses the commercially available nonlinear finite element solver MSC.Marc with the MSC.Mentat as graphical user interface. Multidimensional current profiles are implemented in *Hydro-FE* by constrained RBF approximation method described in Section 2. In the simulations presented in this paper, the values of significant wave height and period were used to obtain the corresponding JONSWAP wave spectrum with parameters of $\alpha = 0.00035, \gamma = 1, \sigma = 0.07$ when $\omega \leq \omega_p$, and $\sigma = 0.09$ when $\omega > \omega_p$ (Rueda-Bayona et al., 2020). This spectrum was then reproduced in *Hydro-FE* by a finite superposition of linear Airy waves characterized by their height, length and frequencies (Dean and Dalrymple, 1991).

The hydrodynamic forces exerted on the nodes are calculated with Morison equation (Morison et al., 1950; Goodman and Breslin, 1976). The contact between the seafloor and the mooring chains was simulated using techniques that has been previously implemented in *Hydro-FE* (Knysh et al., 2021). All components of the farm (grow line, mooring line, chain, etc.) were modeled with 2-node three-dimensional truss elements, except for the floats that were assumed to be beam elements. The number of elements used for each of the component, as well as the linear mass densities values are provided in Table 3.2.

Table 3.2. Linear density and number of finite elements assigned to the Wood Island kelp farm *Hydro-FE* model.

Kelp farm component	**Linear mass density [kg/m]**	**Number of finite elements**
Mooring/grow lines	0.13	266
Mooring Chains	4.45	16
Kelp (mass per grow line length)	11.27	1005
Buoys	-	8

Numerical simulations were performed with three sample current (Fig. 3.4), wave and depth (Table 3.1) data sets measured on May 16, May 20 and May 24, 2019. The *15 min* simulation analysis time corresponded to *15 min* field measuring intervals described in Section 3. The large strain case, the implicit dynamic single-step Houbolt transient operator and the lumped mass matrices were prescribed to Marc finite element solver in each simulation. The adaptive time steps were utilized and produced about 80,000 time increments in each simulation.

4.2 Simulation results and discussion

Numerical predictions of the longline performance of the farm in this study were compared for four cases that represent different current field approximation strategies (Fig. 3.7). The first case, *mean velocity*, is the simplest approach (Fig. 3.7a). It is typically used when only one measuring device, such as an ADCP or a current meter, is available at the deployment site. The current is then assumed to be uniform with the magnitude equal either to the mean velocity through the depth (for the ADCP data) or to the current at the specific depth (for the current meter data). In this study, the mean velocity from the east ADCP location was used. The second case incorporated *linear interpolation* between the current profiles from the east ADCP (Fig. 3.7b). In the third case, *1D RBF approximation* is applied to the current profile obtained from the east ADCP data set (Fig. 3.7b). In this case, however, the constrained one-dimensional RBF current approximation approach from Section 2 was implemented. The fourth case, the *2D RBF approximation*, is based on both west and east ADCP data sets (Fig. 3.7c). The approximation in the fourth case was performed with the advanced constrained multidimensional RBF technique described in Section 2. Note that the average between wave data sets (wave direction, significant wave height and period) obtained by the west and east ADCPs was used in the *2D RBF approximation* case, while all other cases utilized the wave data set obtained by the east ADCP only.

Fig. 3.8 shows the kelp farm response comparison of the west mooring tension from the four cases. Almost identical west mooring line tensions are obtained for *linear interpolation* and *1D RBF approximation* cases in all three environmental loading scenarios (Fig. 3.8a,b,c) since they are based on the same data sets and must produce similar one-dimensional current profiles. It can be seen that the lowest difference in the predicted tensions is found from the low-magnitude

profiles obtained on May 24, 2019 (Fig. 3.8c), where both major sources of drag, namely upper lines/floats and kelp, are subjected to the currents of about *0.10 m/s* and lower (Fig. 3.4c).

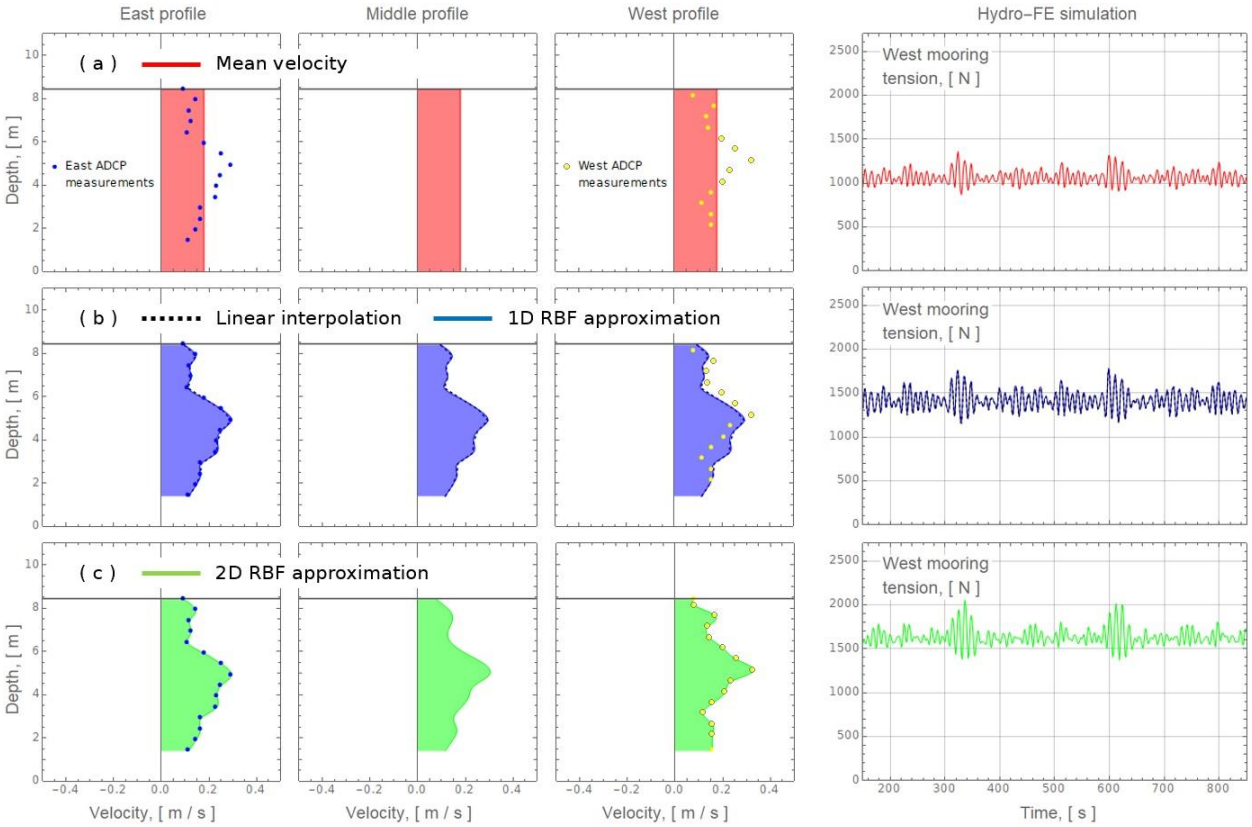

Figure 3.7. Approximation of the current profile by (a) *mean velocity,* (b) *linear interpolation* and *1D RBF approximation*, (c) *2D RBF approximation* approaches used in *Hydro-FE* simulations. The predicted tensions of the west mooring are shown to the right. The East and West current velocity profiles are based on the ADCP measurements at the corresponding locations produced on May 16, 2019. The Middle profile is obtained using the considered approximations.

Similar trends are also observed for the east mooring line tensions (Fig. 3.9), however values are noticeably lower than the west mooring tensions due to the east-dominated currents in all three sample data sets (Fig. 3.4). Fig. 3.9c demonstrates that lowest difference between the west and east

tensions in all four current velocity approximation cases is naturally achieved for low-magnitude profile registered on May 24 (Fig. 3.4c).

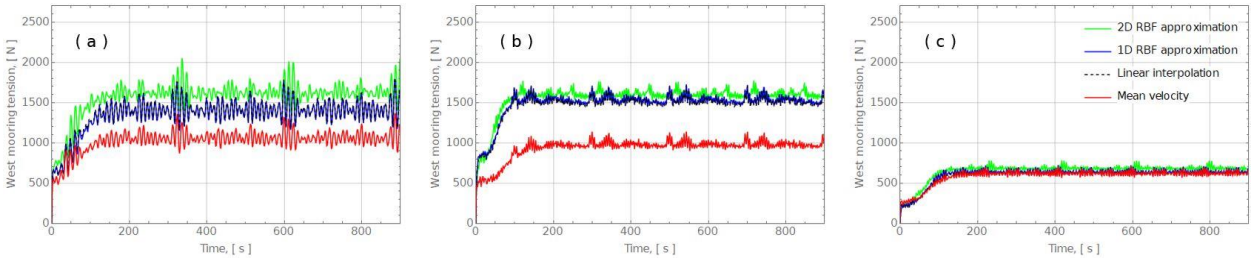

Figure 3.8. West mooring line tensions obtained in *Hydro-FE* simulations using different current approximation techniques. The current and wave parameters are taken from data sets obtained at Wood Island site on (a) May 16, (b) May 20 and (c) May 24, 2019.

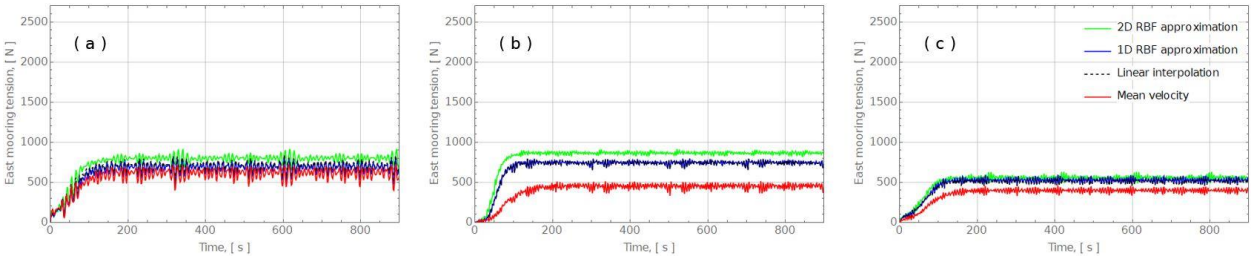

Figure 3.9. East mooring line tensions obtained in *Hydro-FE* simulations using different current approximation techniques. The current and wave parameters are taken from data sets obtained at Wood Island site on (a) May 16, (b) May 20 and (c) May 24, 2019.

More substantial differences in mooring line tensions are observed for high-magnitude velocity profiles observed on May 16 (Fig. 3.4a) and May 20 (Fig. 3.4b). For these datasets, the *mean velocity* case underpredicts both west and east mooring line tensions relative to other approximation techniques since magnitude of mean velocity is slightly lower than the magnitude of current velocity registered at the average kelp depth (Fig. 3.8a, 3.9a) and at the neutral water level (Fig. 3.8b, 3.9b). For example, the *mean velocity* profiles produce west mooring line tensions

that are about 34-38% lower than the tensions obtained in *2D RBF approximation* cases. (Fig. 3.8a,b). This discrepancy range is even higher for east mooring line tensions, being about 22-47% (Fig. 3.9a,b).

The difference between *2D RBF approximation* and *1D RBF approximation* cases are of special interest when selecting the most robust approximation technique. It was found that even a small divergence of about *0.03 m/s* in west and east ADCP current measurements at the average kelp depth (in the major axis direction) can lead to 15% increase in the predicted highest (west, to be exact) mooring line tension (Fig. 3.8a). Even with the close distance of *42 m* between west and east ADCPs at Wood Island site, comparing to the scale of typical large aquaculture installations, utilization of a more accurate *2D RBF approximation* makes substantial difference in evaluating the kelp farm performance. Note that for current measurements on May 20, 2019 (Fig. 3.4b), the increase in mooring tension is only 7% that is attributed to magnitude of current velocity measured by the west ADCP being higher than the magnitude of the current velocity measured by the west ADCP at the depths between average kelp position and neutral water level (Fig. 3.4b).

The total grow line displacement of the Wood Island kelp farm for the four current velocity approximation techniques were also compared in terms of a displacement of the grow line's middle point. Fig. 3.10 shows the overall displacement (including three components) of the grow line middle for the data sets registered on May 16 (Fig. 3.10a), May 20 (Fig. 3.10b) and May 24, 2019 (Fig. 3.10c). It was found that the difference in the displacements between *linear interpolation*, *1D RBF approximation* and *2D RBF approximation* cases is practically negligible being less than 2%. It was also found that the *mean velocity* profile predicts displacements that are substantially lower, similar to what was observed for mooring line tensions. The difference in displacements reaches up to 6-18% depending on the environmental data sets considered.

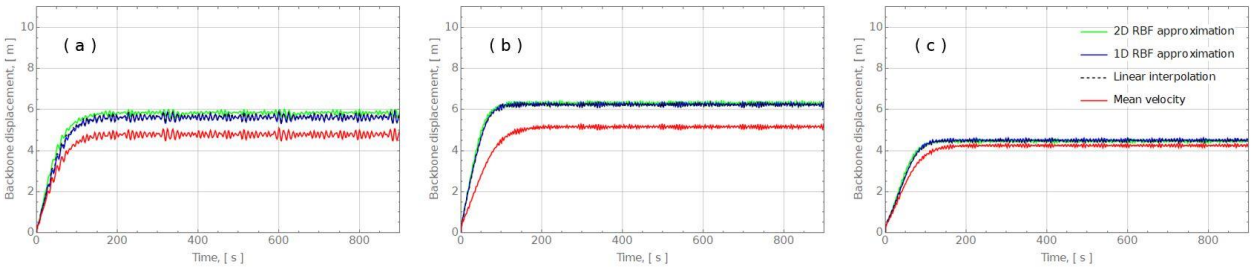

Figure 3.10. Displacement of the grow line middle obtained in *Hydro-FE* simulations using different current approximation techniques. The current and wave parameters are taken from data sets obtained at Wood Island site on (a) May 16, (b) May 20 and (c) May 24, 2019.

6. Conclusions

Distribution of currents at large-scale offshore aquaculture sites is usually available as a set of discrete data points obtained from measurements or ocean dynamic models. This paper proposes an efficient methodology to approximate the discrete multidimensional current velocity data for numerical analysis as applied to ocean deployed aquaculture installations. The current velocities at such marine sites can spatially vary, so applying accurate and smooth current field approximations are essential to estimate the performance of the aquaculture system.

The meshless radial basis function approximation method produces such smooth and accurate approximation of discrete current velocity data obtained from field measurements and works on both regular and irregular grids. However evenly distributed data points in each dimension are still recommended. Numerical experiments showed that possible under- or overfitting of the radial basis function approximation are addressed with a combination of domain rescaling, thin plate regularization and constraining the approximation values at boundary points.

The proposed current approximation method was implemented in *Hydro-FE* software and tested on the example of kelp farm deployed at Wood Island research site in Maine, USA.

Numerical simulations of the farm were performed using field velocity measurements conducted in spring 2019.

It is shown that the difference in the mooring line tensions of the kelp farm can reach up to 34-38% between mean velocity profile and two-dimensional radial basis function approximation, or 15% between one- and two-dimensional radial basis function approximations. The total displacements of the grow line middle turned out to be practically the same for all approximation techniques, except for mean velocity, where the displacements appear to be 6-18% lower. This means that additional measurements combined with the advanced approximation method presented in this paper allows to substantially improve prediction of aquaculture installation performance.

Chapter IV

Floating protective barriers: evaluation of seaworthiness through physical testing, numerical simulations and field deployment

This chapter was published as *Knysh, A., Coyle, J., DeCew, J., Drach, A., Swift, M.R. and Tsukrov, I., 2021. Floating protective barriers: evaluation of seaworthiness through physical testing, numerical simulations and field deployment. Ocean Engineering, 227, p.108707.*

My contribution to the paper was developing the numerical model of the *Triton* barrier and its validation through single-frequency wave tank tests and field deployments. Additionally, I processed extensive experimental data from the wave tank tests, and prepared the first draft of the manuscript for publication.

Abstract

Floating protective barriers provide essential protection to critical governmental, commercial, and private assets that are vulnerable to water-borne intrusion, such as liquefied natural gas terminals, tankers, etc. These barriers require additional evaluation in the case of their deployment at significant water depth in offshore environments. The seaworthiness of the *Triton* barrier design

developed by HALO Maritime Defense Systems (US) was investigated through a combination of field deployment, physical testing and numerical simulations. The full-scale *Triton* barrier, deployed and inspected south-southwest of White Island, Isles of Shoals, New Hampshire, provided important information on its dynamic behavior and the overall structural integrity under monitored environmental conditions. Physical tests of a Froude-scaled barrier model were conducted in Chase Ocean Engineering Laboratory wave tank at the University of New Hampshire to properly measure response of the structure and its mooring to different single-frequency waves directed parallel and normal to the model. Both physical tests and field study load cases were numerically simulated in finite element *Hydro-FE* software. The comparisons indicated a good correspondence between physical tests and numerical models in terms of heave, pitch, roll and force response amplitude operators. Overall, the full-scale *Triton* barrier has demonstrated robust performance during the offshore field deployment.

Keywords: floating barriers, wave response, finite element analysis, physical testing, field deployment.

1. Introduction

Floating protective barriers can be used to protect naval bases, offshore platforms, ports, nuclear power facilities, bridges, dams, refineries and desalination plants and other assets from terrorist attacks in different marine environments. They prevent attacks by a simple boat loaded with explosives which is one of the most popular and dangerous types of the attack due to its relative cheapness and technical simplicity (Hill, 2009). Fig. 4.1 illustrates consequences of a small

suicide boat attack on M/V Limburg, a French-flagged VLCC supertanker, off of the port of Ash Shihr, southeast of Sana'a, Yemen, in October 2002 (Greenberg et al., 2006). The explosion lead to loss of several crewmembers and a spill of over 50,000 barrels of oil (Carafano, 2007). Another well-known example is that of suicide terrorists exploding a motorboat alongside the USS Cole — a Navy Destroyer — as it was refueling in the Yemen port of Aden on October 12, 2000 (Perl and O'Rourke, 2001). The blast ripped a 10-meters-wide hole near the waterline of the Cole, killing 17 American sailors and injuring many more.

Fig. 4.1. The M/V Limburg on fire after being hit by a suicide boat at port in Yemen (Source: Jones, 2006).

In order to effectively prevent such catastrophes, the performance of floating protective barriers of different designs are usually investigated through field studies (DeCew and Rowell, 2013; Kalinski et al., 2014). Although most of the studies have been focused on actual waterborne craft impact testing and corresponding design optimizations which are then proved by U.S. Navy and other military or civilian customers (Nixon et al., 2004, 2005; Bishop, 2013; Osienski et al.,

2017), some numerical investigations have also been conducted since large-scale tests are quite expensive and labor-intensive. For instance, a series of full-scale finite element simulations and the corresponding real impact tests of FOXX barriers were performed by Polish Naval Academy (Kiciński et al., 2019). To the best of the authors' knowledge, there are no other publicly available publications related to either physical or numerical testing of floating protective barriers.

In offshore deployments, in addition to impact protection, the floating barriers and their mooring systems have to be able to withstand high-energy environmental loading conditions without experiencing significant damage or even failure. The purpose of this paper is to present a comprehensive approach to the prediction and evaluation of floating barrier offshore performance using the example of a *Triton* floating barrier manufactured by HALO Maritime Defense Systems, USA (Fig. 4.2).

Fig. 4.2. The *Triton* barrier being towed to the University of New Hampshire offshore research site on January 10, 2018.

The approach includes a combination of full-scale field studies, scaled physical testing and numerical modeling. The four-month-long field deployment of the barrier continued from January to May 2018 near the Isles of Shoals, New Hampshire, USA, and covered a period of the winter storms (Fig. 4.3). The scaled physical testing (1:20) was conducted in the University of New Hampshire (UNH) wave/tow tank utilizing techniques previously developed and validated for various offshore aquaculture installations (Fredriksson et al., 2000; DeCew et al., 2005; Wang et al., 2015). The numerical modeling was performed with the finite element analysis software *Hydro-FE* based on the well-validated *Aqua-FE* program developed at UNH (Gosz et al., 1996; Tsukrov et al., 2000, 2003; Fredriksson et al., 2003) and extensively applied in the marine aquaculture field (DeCew et al., 2010; Wang et al., 2015; Knysh et al., 2020).

The rest of the paper is organized as follows. Section 2.1 is dedicated to the field study organization, description of the research site and data acquisition. Manufacturing of the scaled *Triton* barrier and its mooring, as well as a description of the experimental facilities and instruments, are presented in Section 2.2. Section 2.3 covers development of the numerical model and its basic parameters. The comparisons between single-frequency wave results obtained in physical tests and numerical simulations are given in Section 3. The section also includes comparison between barrier responses to random waves observed in the field study and numerical modeling. The conclusions are presented in Section 4.

Fig. 4.3. Helicopter view of the *Triton* barrier during the North Atlantic storm on March 5, 2018.

2. Methods

2.1 Field study

2.1.1 Description of the barrier system

The investigated *Triton* barrier system consists of four *15 m* units. Each unit is *6 m* high, *3.3 m* wide and stands approximately *3 m* off the water. The units are joined together by dual ethylene propylene diene monomer (EPDM) rubber hinges allowing the segments to contour waves and absorb the loading due to the high-energy marine environment (Fig. 4.4a). Schematics of each unit

can be seen in Fig. 4.4b, which depicts the first unit with the mooring line attachment at the left end. Units consist of two longitudinal pipes connected to transverse and side members with upper and lower pipes, all made of high-density polyethylene (HDPE). Most of the side and transverse members are attached to the longitudinal, upper and lower pipes by butt-fusing Tees which are held in place by pins and tabs. Attachment methods also include hangers strapped around the pipe and eyes through-bolted to the pipe. The stainless steel impact netting is suspended from the upper pipe and attached to the transverse members. The first unit of the barrier deployed in the field study also included an instrument box with accelerometer and data pack powered by a solar panel. The instrument box is attached to the upper pipe that is supported by side members.

The longitudinal pipes of neighboring units are connected by hinges at the waterline and additionally secured by limiter cables that ensure structural integrity even if hinge is damaged. Longitudinal pipes contain closed cell foam flotation whereas the lower pipe is filled with heavy chain ballast providing increased stability. The impact netting of each unit is connected to each other by the net joint and placed between the longitudinal and upper pipes, so it is present along the whole barrier. More information on geometric and mechanical properties of the barrier's components is presented in Sections 2.2 and 2.3.

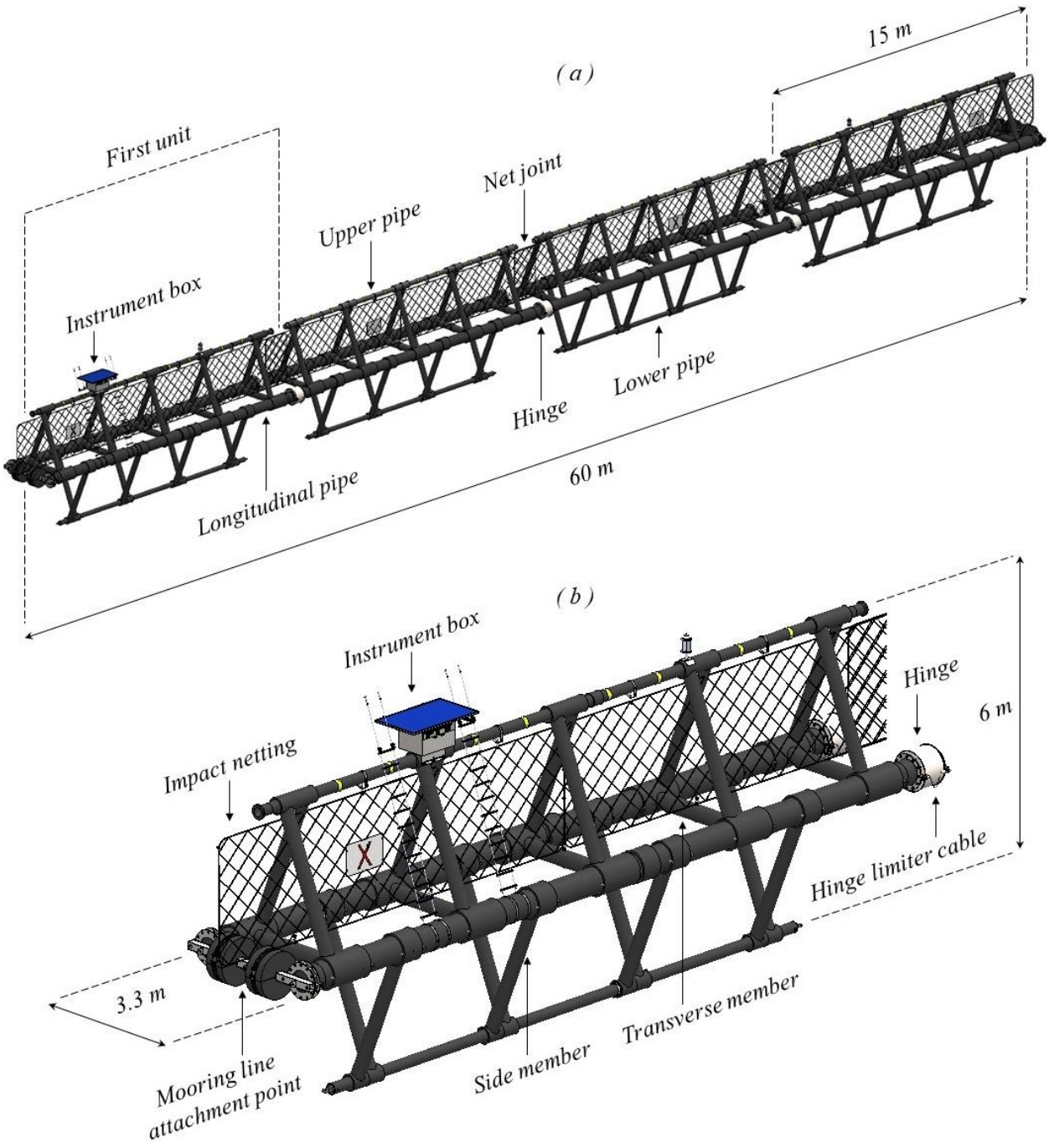

Fig. 4.4. Schematics of the HALO *Triton* barrier investigated in field studies: *(a)* four-unit unit system deployed in North Atlantic; *(b)* instrument box and mooring line attachment.

2.1.2 Offshore deployment site and mooring setup

The four-unit barrier was deployed at the *52 m* deep UNH research site located *2.8 km* south-southwest from White Island, Isles of Shoals, New Hampshire, USA (see Fig. 4.5). It was oriented north-south. The deployment continued from January to May 2018 to cover the period of the winter for which northeast storms typical of the North Atlantic were present. An average tidal range seen at Gosport Harbor at the Isle of Shoals from the National Ocean Service tide charts is *2.6 m* with the tidal current at the UNH research site of roughly *10 cm/sec*.

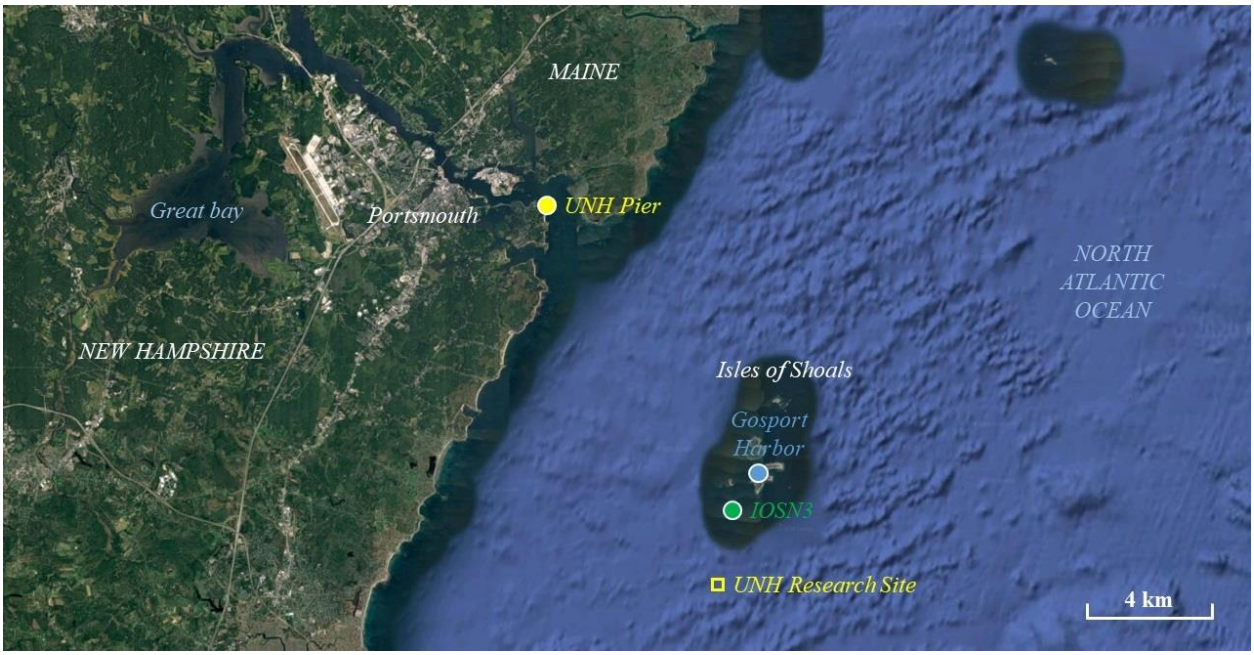

Fig. 4.5. Location of the UNH Pier and the boundaries of UNH research site at the time of deployment. The geographic coordinates of the site corners are (42°56.669′ -70°38.114′), (42°56.669′ -70°37.824′), (42°56.461′ -70°38.114′) and (42°56.461′ -70°37.824′).

The barrier's mooring system was designed based on the seafloor and environmental features of the UNH site. Its schematics is shown in Fig. 4.6. There are two *15 m* short fiber bridles

connecting the barrier to surface buoys of *40 kN* buoyancy. Two *105 m* long fiber lines hang from the buoys and are attached to *2800 kg* stud-link chain, which provides damping and prevents excessive mooring line jerking. The chain is fixed by a *2000 kg* dead weight and secured by drag embedment anchor at its end. More information on geometric and mechanical properties of the mooring components is presented in Section 2.2.

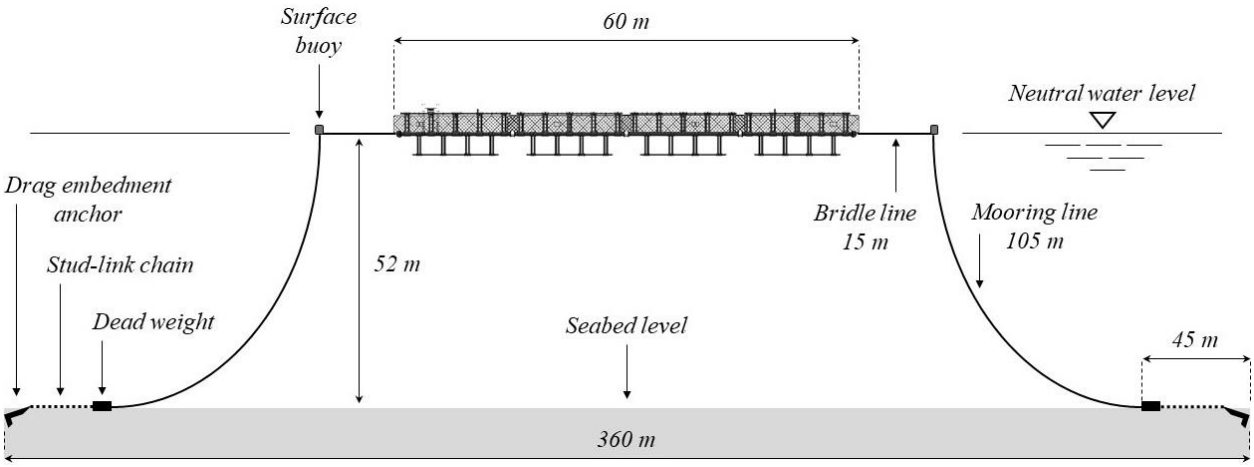

Fig. 4.6. Schematics of the *Triton* barrier mooring setup developed for the UNH offshore site. Not to scale.

2.1.3 Field data acquisition

The *Triton* system was equipped with four Globalstar SmartONE C small onboard global positioning system (GPS) tracking devices, one on each of the four units. These GPS devices allowed for the position of the barrier, while deployed, to be monitored from shore. As each *Triton* unit was equipped with a device, in the event of a separation or mooring failure, each unit could be tracked individually. The barrier's motion during the entire deployment, including deployment

and retrieval, as well as the barrier's movement during its time at the research site were tracked and did not cross expected boundaries.

To measure the gravitational and dynamic accelerations experienced by the barrier, a specifically designed system consisting of a 9-axis accelerometer, gyroscope, and magnetometer was utilized. The system was powered by Arduino ATmega328P microcontroller processor and attached to the upper pipe of the first barrier unit. In order to determine the barrier's heave response to wave forcing, vertical acceleration data was logged hourly in individual files and then analyzed. The wave environment of the UNH offshore site was characterized using a subsurface wave logger made by RBR. This dual channel (temperature and depth, tide and wave logger) device was attached below a taut-moored subsurface buoy at the research site. Each time the instrument was retrieved, its data was downloaded, processed with Ruskin software included with the device, and the battery replaced. The software derived tidal slope, significant wave height, significant wave period, maximum wave height, maximum wave period, average wave height, average wave period, peak period, wave energy per area, average sea pressure, etc.

A secondary source of wave data was the NOAA National Data Buoy Center (NDBC) station 44098 at Jeffrey's Ledge, New Hampshire. The station is a wave-rider buoy located *40 km* east-southeast of the UNH research area in *76.5 m* of water. UNH owns and operates the buoy while Scripps Institution of Oceanography processes and makes the wave data available. The NDBC historical data summaries from station 44098 provided significant wave height, peak period and wave direction. These correspond well to values observed at the test site as long as the waves are from the east. Although both sources of wave information were totally valid, the NDBC data was chosen for the analysis of random waves heave response in this paper.

In addition to wave data, wind data was available from nearby White Island at the Isles of Shoals, where NOAA owns and operates the meteorology station IOSN3. The station is housed within White Island Light House and is less than *2.8 km* north-northeast of the UNH research area as seen in Fig. 4.5. From the station's historical data and climate summaries, wind data was extracted for the months of the barrier's deployment. The average wind speed from the anemometer was corrected from *32.2 m* to *10 m* above sea level, an industry standard, for all wind averages shown. Unlike the most common for UNH site south-east wave direction, the typical north-west wind of *6.5 m/s* was registered during the months of deployment. The wind data was not implemented in the models presented in this paper, however, it is available for future research.

2.1.4 Inspections and observations of the barrier

During and after the *Triton* barrier deployment, the system was visited by UNH and HALO teams at the site using two UNH vessels: the research vessel Gulf Challenger and the Galen J. All of the visits that involved adding instruments, downloading data, making repairs, etc., were made on Galen J. Gulf Challenger, which is a larger vessel, was used for the subsurface wave logger retrieval and for visual inspections with the vessel passing close-by the barrier.

As the deployment period ended, the barrier was towed in to the UNH Pier and looked over by UNH and HALO personnel onshore on June 1-7, 2018 (Fig. 4.7). Although *Triton* barrier did not lose structural integrity and its basic HDPE framework was remarkably sound, some damage was observed in all four units, such as lost pins and fused tabs, rotated or cracked transverse members, longitudinal pipes and side members (Swift et al., 2019).

Fig. 4.7. Triton® barrier units separated and towed in to UNH Pier.

2.2 Physical testing

2.2.1 Scaled physical model of the barrier and mooring

A scaled physical model of the *Triton* barrier system was used to evaluate its performance in a wave environment. The experiments were conducted in the UNH *36.6 m* long, *3.66 m* wide, *2.44 m* deep wave tank. As inertia and gravity forces are the most influential factors that the barrier

experiences, the Froude scaling method was chosen for the test (Wendland, 2005). The scaling factor of 1:20 was selected by using the approximate ratio of the depth of the UNH offshore research site (*52 m*) and the depth of the wave tank (*2.44 m*). With the scaling factor selected, the physical dimensions and weight of the model were calculated. To retain geometric similitude, the diameter and length of each scaled component was first found. Then, the weight of model components was appropriately scaled and calculated based on their geometry.

The full-scale *Triton* barrier is constructed with HDPE pipes that allow the system to be robust, yet compliant to a wave environment. An attempt was made to exactly scale the compliance of the pipes in the model. Many materials were investigated to accomplish the 1:20 Froude scaled flexural rigidity as well as the desired weight of each structural component. However, no appropriate material was discovered since it either gave considerable fabrication issues or just did not exist in the appropriate geometric similitude. In addition, certain components had some additional requirements. Unlike the top member, the bottom member needed to be hollow to allow ballast to be inserted. The main longitudinals had to provide the bulk of the buoyancy, therefore the material selected needed to be buoyant. Hollow pipes were also necessary for the transverse members, so an extra weight could be inserted to retain the correct center of gravity. Thus, while the scaling of other physical parameters was precise, the stiffness of each model unit was higher than desired. However, the units were connected by structurally scaled flexural hinges. Table 4.1 provides the basic full-scale and model-scale parameters of the *Triton* barrier. The rigorously scaled parameters are presented as “Desired model-scale”, the actual choice of components is provided as “Actual model-scale”.

Table 4.1. Basic parameters of full-scale and model-scale components of *Triton* barrier.

Unit structural component		Length *[m]*	Diameter *[m]*	Weight *[kg]*	Material details
Actual full-scale	Upper pipe	15.2	0.22	128.8	DR17 HDPE
	Lower pipe	11.9	0.22	100.5	DR17 HDPE
	Side member	3.1	0.27	41.2	DR17 HDPE
	Transverse member	2.4	0.32	44.5	DR17 HDPE
	Longitudinal pipe	14.9	0.51	678.6	DR17 HDPE
Desired model-scale	Upper pipe	0.76	0.011	0.016	-
	Lower pipe	0.60	0.011	0.013	-
	Side member	0.16	0.014	0.005	-
	Transverse member	0.12	0.016	0.005	-
	Longitudinal pipe	0.75	0.025	0.085	-
Actual model-scale	Upper pipe	0.76	0.010	0.023	PEX
	Lower pipe	0.60	0.010	0.018	PEX
	Side member	0.16	0.013	0.005	balsa wood
	Transverse member	0.12	0.016	0.009	PEX
	Longitudinal pipe	0.75	0.025	0.075	balsa wood

At full-scale, EPDM rubber hinges connecting barrier units to each other allowed them to contour to the wave environment and absorb loads applied to the barrier by wave forcing. At model scale, the rubber tubing that met the scaled flexural rigidity properties was selected. However, it turned out to be much lighter than the desired scaled weight of the hinge. Therefore, steel washers were attached at connections for the hinges which increased the weight to the desired value (Fig. 4.8a). The flexural rigidity of the hinge is a proprietary information of HALO Maritime Defense Systems, so its full-scale and model flexural rigidity cannot be provided here. In addition

to steel washers, four steel end plates were attached to both ends of the model, allowing mooring lines and a load cell to be installed. These plates attached to the barrier model with eye rings provided additional mooring attachment points (Fig. 4.8b). Finally, the collars connecting full-scale horizontal transverse members with the longitudinal pipes were substituted by the cable zip ties as shown in Fig. 4.8. The cable-tie attachments required presence of holes in transverse members for cables to go through, however, the members themselves were kept waterproof to not introduce any additional weight and inertia to the system.

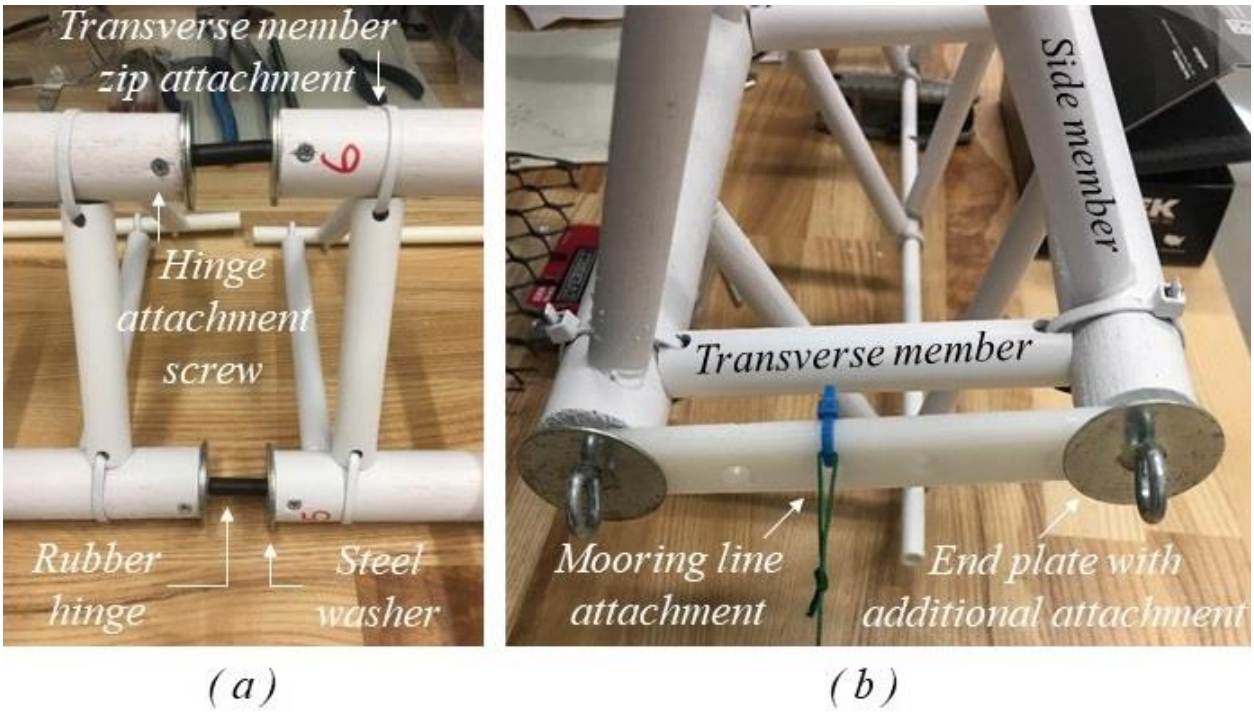

Fig. 4.8. Scaled model components: *(a)* side view on hinges; *(b)* front view on mooring line attachments.

The mooring system was Froude scaled for the anchor, floats, chain, dead weight and lines. The scaled mooring line was *8 mm* monofilament fishing leader, while the bridle lines were made of

braided fishing line. Since the scaled buoys needed to provide up to 5 *N* of buoyancy, simple *4.9 N* pool floats were chosen for this purpose. Both scaled chain and clump weight were constructed of zinc plated jack chain (see Fig. 4.9). The results of Froude scaling for the mooring system are summarized in Table 4.2. The embedment anchors were modeled as fixed points; *4.5 kg* lead weights were used to hold the chain ends stationary on the tank bottom.

Table 4.2. Full-scale and model-scale values used for material selection of the mooring system.

Mooring component	**Full-scale**			**Model-scale**		
	Length ***[m]***	**Weight** ***[kg]***	**Density** ***[kg/m]***	**Length** ***[m]***	**Weight** ***[kg]***	**Density** ***[kg/m]***
Bridle line	15	15.9	1.06	0.75	0.002	0.003
Mooring line	105	111.3	1.06	5.25	0.016	0.003
Chain	50	2775	55.5	2.5	0.34	0.14
Dead weight	-	2000	-	-	0.25	-

Fig. 4.9. Mooring components used for model tank testing.

2.2.2 Facility and instruments

The scaled model was tested in the UNH Chase Ocean Engineering Laboratory wave tank under a variety of wave conditions. The wave tank is capable of generating waves up to a half-meter in height by using a hydraulic wave generator. The movable tow carriage that travels the length of the wave tank allowed adjustable motion camera angles and streaming of data from the load cell to the main host computer. The UNH tank can generate not only single-frequency waves but also random waves, however, most of the conducted tests represented single-frequency scenarios.

Before wave testing, the Futek LSB210 two-pound submersible S-beam load cell was calibrated in tension with known weights. The voltage output was recorded, and a linear calibration line calculated. It was then entered into the LabView software, allowing the load from the voltage output to be determined. The load cell was end mounted on the model to measure mooring force acting on one of the bridle lines.

To capture the model's dynamics, a GOPRO HERO 3+ camera was installed on a pole vertically mounted to the tow carriage. The carriage was then moved into place aligning the camera with the target attached to the top of the model in approximately the same location as the data pack that contained the accelerometer at full-scale (Fig. 4.10).

To quantify the model's dynamics, each video recorded during testing was analyzed using Kinovea motion tracking software. The software always tracked the target central point as well as 1-2 additional points on the target or structure to record heave and pitch/roll motion of the barrier. The black points on the orange target against the white tank background provided enough contrast to allow them to be tracked by the software.

Fig. 4.10. Target used to track model dynamics.

2.2.3 Mooring configuration of the model

The barrier deployment plan included *2224 N* (full-scale) of pretension in the mooring bridle line. It was decided to scale and implement this pretension (*0.28 N* model-scale) by gradually moving away the lead weight until the desired value of tension was achieved. As the effect of tension was of interest, an additional set of tests with the doubled pretension (*4448 N* which corresponds to *0.556 N* model-scale) was also performed.

With the defined pretension, the barrier was oriented parallel (inline test) and perpendicular (sideways tests) to the wave propagation direction, see Fig. 4.11. The sideways orientation required the mooring system setup to be altered due to insufficient wave tank width. To resolve this issue,

two smooth, vertical directional cylinders were utilized. The cylinders made of vertically mounted PVC pipes allowed the scale model and mooring to be installed such that the mooring line was redirected from across the width of the tank, to along the length of the tank, see Fig. 4.11b and Fig. 4.11c.

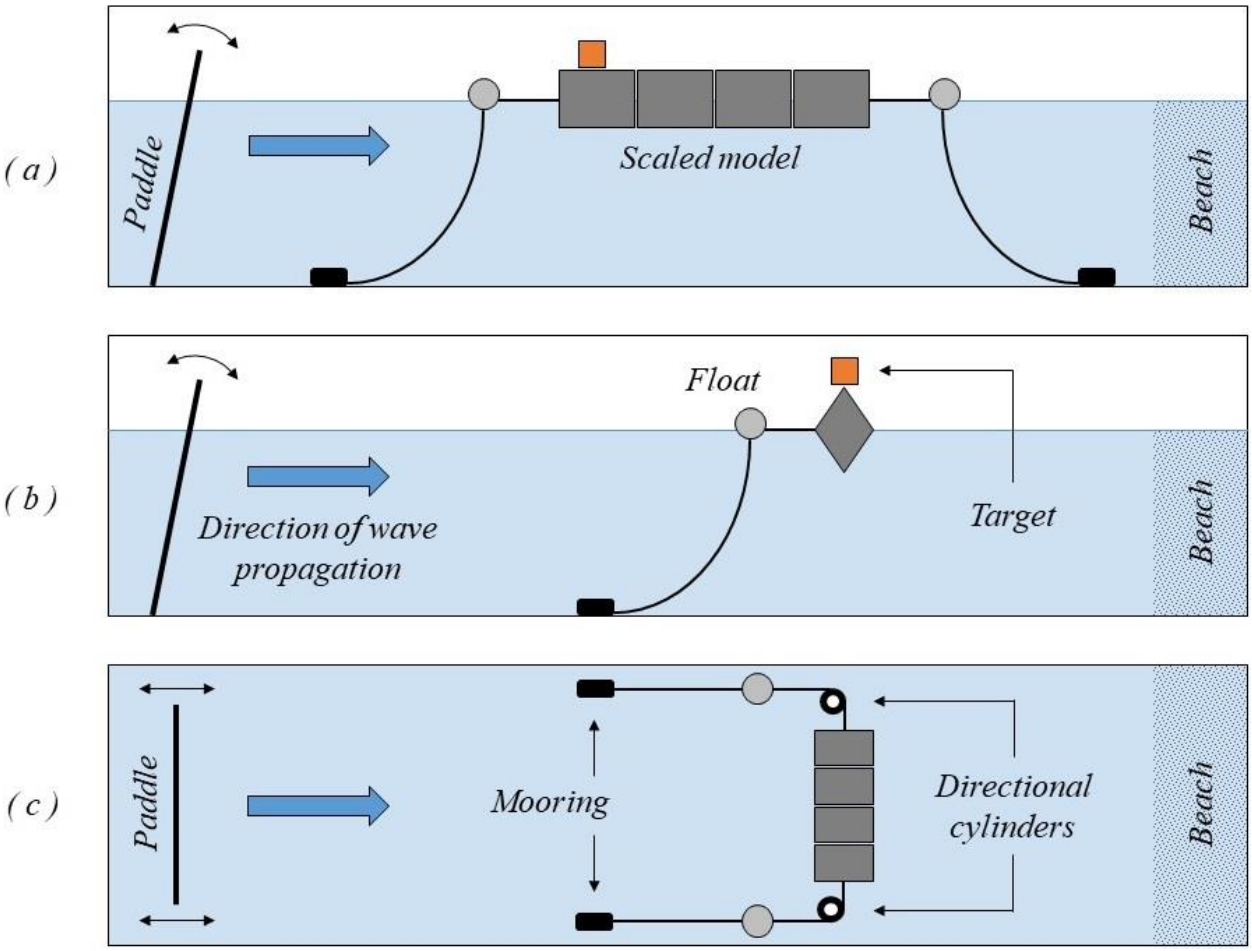

Fig. 4.11. The UNH wave tank experimental setup: *(a)* inline model orientation, side view; *(b)* sideways model orientation, side view; *(c)* sideways model orientation, top view.

2.3 Numerical simulation

2.3.1 Numerical model of the barrier

In this study, the finite element (FE) model of the full-scale barrier was created in *Hydro-FE* software (Fig. 4.12). *Hydro-FE* modernizes the approach previously implemented in the well-validated *Aqua-FE* program developed at the University of New Hampshire (Gosz et al., 1996; Tsukrov et al., 2000; Fredriksson et al., 2003) to analyze partially or completely submerged flexible structures in the marine environment. The code is written in FORTRAN and uses the commercially available nonlinear finite element solver MSC.Marc with the graphical user interface MSC.Mentat. Wave environmental conditions in *Hydro-FE* are implemented using Airy wave theory (Dean and Dalrymple, 1991).

For the *Triton* barrier simulations, the finite element solver was prescribed a large strain case, implicit dynamic transient operator (single-step Houbolt) and lumped mass matrices. The total load case time of *500 s* with the adaptive time stepping resulted in 15,000-20,000 increments per simulation.

As the main structural components, such as longitudinals, hinges, side members, transverse members, upper and lower pipes, are not only the major source of drag and inertia forces but also important in providing structural rigidity, these components were modeled with 2-node three-dimensional beam elements to account for bending moments and torque. At the same time, mooring chain, bridle and mooring lines were modeled with 2-node three-dimensional truss elements to preserve their compliance. Basic material and geometrical properties of the finite elements are given in Table 4.3.

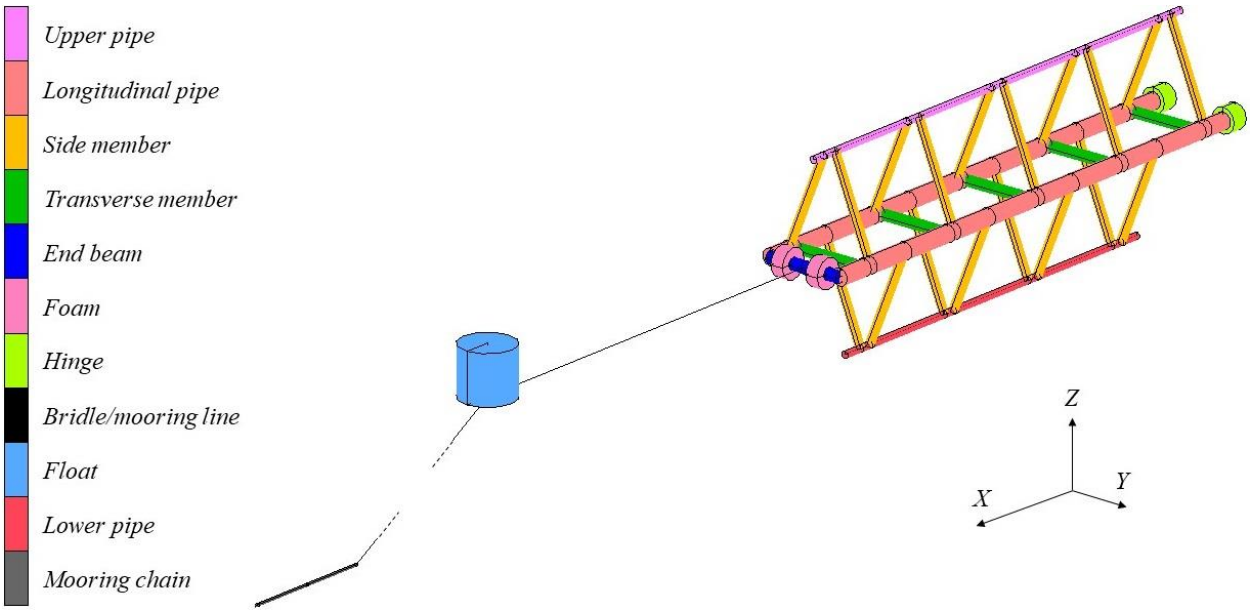

Fig. 4.12. Finite element model of the barrier's unit and mooring system. Not to scale.

Note that most of the finite element parameters correspond to the actual properties of the barrier. However, some of them were recalculated based on reasonable simplifications as follows. The weight of small components that cannot be properly modeled (tabs, bolts, impact net, etc.) was uniformly distributed along the longitudinals, side and transverse members, hinges, upper and lower pipes. The weight of the ballast chain was added to the weight of lower pipes. Material density of floats was averaged across the whole floats' volume, whereas their Young's modulus and Poisson's ratio were selected as generic plastic values, since they do not significantly influence the overall barrier response. The diameter of the mooring chain elements was calculated to keep the chain density and overall weight unchanged.

Table 4.3. Structural and geometrical parameters of the barrier's FE model. Recalculated values are shown with gray background.

Structural component	**Material density** ***[kg / m^3]***	**Young's modulus** ***[GPa]***	**Poisson's ratio** ***[-]***	**Flexural rigidity** ***[MPa-m^4]***	**Cross-section area** ***[m^2]***	**Outer diameter** ***[m]***	**Number of elements** ***[-]***	**Element type**
Longitudinal	962	1.07	0.41	1.37	0.045	0.508	120	2-node, beam
Hinge	n/a	n/a	n/a	n/a	n/a	n/a	6	2-node, beam
Side member	962	1.07	0.41	0.115	0.013	0.273	72	2-node, beam
Transverse member	962	1.07	0.41	0.320	0.027	0.324	20	2-node, beam
Upper pipe	962	1.07	0.41	0.066	0.012	0.219	44	2-node, beam
Lower pipe	4660	1.07	0.41	0.066	0.012	0.219	36	2-node, beam
Bridle/mooring line	1400	8.30	0.28	-	0.0016	0.045	134	2-node, truss
Surface float	421	1.00	0.30	-	2.2	1.676	2	2-node, truss
Mooring chain	7860	205	0.29	-	0.007	0.094	50	2-node, truss

2.3.2 Morison's equation

In order to calculate force exerted by waves on structural components, the Morison's equation approach (Morison et al., 1950) expanded to the case of a moving cylinder (Goodman and Breslin, 1976) was used in this study. According to this approach, there are two vectors associated with each differential section dL of the submerged cylindrical body of outside diameter d_o arbitrarily moving in the water: the local fluid velocity vector $\boldsymbol{u}$ and the body velocity vector $\boldsymbol{v}$. Both of these vectors can be projected on normal (perpendicular to the cylinder axis) and tangential (parallel to the cylinder axis) directions. Then, the normal projection of the force exerted on a differential section dL is

$$d\boldsymbol{F}_n = \rho_w \frac{\partial \boldsymbol{u}_n}{\partial t} dV + C_a \rho_w \left(\frac{\partial \boldsymbol{u}_n}{\partial t} - \frac{\partial \boldsymbol{v}_n}{\partial t} \right) dV + \frac{1}{2} C_d \rho_w |\boldsymbol{u}_n - \boldsymbol{v}_n| (\boldsymbol{u}_n - \boldsymbol{v}_n) dA \tag{4.1}$$

where $\boldsymbol{u}_n$ and $\boldsymbol{v}_n$ are the normal projections of fluid and body velocities associated with section dL, C_a is the added mass coefficient, C_d is the normal drag coefficient, $dV = \frac{1}{4}\pi d_o^2 dL$ is the differential volume of section dL, and $dA = d_o dL$ is the differential normal projected area of section dL. The tangential component of the drag force is taken in the form:

$$d\boldsymbol{F}_t = \frac{\pi}{2} C_t \rho_w |\boldsymbol{u}_t - \boldsymbol{v}_t| (\boldsymbol{u}_t - \boldsymbol{v}_t) dA \tag{4.2}$$

where C_t is the tangential drag coefficient, $\boldsymbol{u}_t$ and $\boldsymbol{v}_t$ are the tangential projections of fluid and body velocities associated with section dL. In this numerical study, all of the barrier components were assumed to be smooth cylinders and assigned normal drag coefficient, tangential drag coefficient and added mass coefficient of $C_{dn} = 1.2$, $C_{dt} = 0.01$, $C_a = 1$, respectively.

The Morison's equation formulation assumes that the hydrodynamic forces acting on the structural components are proportional to their relative velocities and accelerations with respect to

surrounding fluid particles. However, it does not contain any direct way to include interference, shadowing, vortex shedding and other fluid flow effects that usually occur in the marine environment. In the Morison's equation based numerical models of offshore aquaculture installations subjected to currents and waves, these effects are usually included through empirically evaluated shadowing coefficients varying from *0.64* to *0.87* applied to the downstream structural components, see, for example, Huang et al., 2006; Moe-Føre et al., 2015; Zhao et al., 2015. The truss structure considered in this paper doesn't contain high-solidity net panels and is subjected to waves only (no current), so the overall effect from fluid flow disturbances is expected to be much smaller. Based on this reasoning the shadowing coefficients in the numerical models were not introduced.

2.3.3 Response amplitude operator

The barrier motion and mooring line tensions resulting from single-frequency wave forcing were characterized by response amplitude operators (RAOs) common in the field of floating structures design. The heave RAO represented relative vertical motion of the barrier and was defined as

$$RAO_h = \frac{A_m}{A_w} \tag{4.3}$$

where A_m is the amplitude of barrier vertical motion and A_w is the wave amplitude or half of the wave height. Pitch and roll RAOs represented angular motion of the system and were defined as

$$RAO_\theta = \frac{A_\theta}{A_w} \tag{4.4}$$

where A_θ is the corresponding barrier's angular motion amplitude in radians. In order to analyze force factors in the system, force RAO for bridle line tension was calculated as follows:

$$RAO_f = \frac{A_f}{A_w} \tag{4.5}$$

where A_f is the amplitude of bridle line tensions. It should be noted that during the processing of the load cell data, large spikes in tensions were registered at individual points in time. If the values of force in these points were more than three times the standard deviation, they were simply excluded from the data set. The load cell data was than filtered with simple moving average (SMA) technique (Brown and Mac Berthouex, 2002).

To investigate the barrier heave response to a random wave forcing and to make use of field data, the random waves heave response amplitude operator RAO_{hr} were utilized (Sethuraman and Venugopal, 2013):

$$RAO_{hr}(f) = \sqrt{\frac{E(f)}{B(f)}} \tag{4.6}$$

where f is the frequency in hertz, $E(f)$ is the energy density spectrum of the barrier heave motion or response spectrum, $B(f)$ is the Bretschneider or incident wave spectrum. The Bretschneider wave spectrum was calculated as follows

$$B(f) = \frac{5}{16}\frac{H_{1/3}^2}{f_m}\left(\frac{f_m}{f}\right)^5 e^{-\frac{5}{4}\left(\frac{f_m}{f}\right)^4} \tag{4.7}$$

where $H_{1/3}$ is the significant wave height, f_m is the modal (most probable) frequency of any given wave in hertz.

3. Results and discussion

3.1 Free release tests of the scaled physical model

Pitch, roll and heave free-release tests were conducted to determine the natural frequencies of the response modes observed during wave excitations. The units of the barrier were lifted until their main longitudinal pipes were just above water level and then released, as schematically illustrated in Fig. 4.13. The target affixed to the top of the first unit was used to track the motion resulting from the free-release tests. The natural frequencies determined by these tests were used to confirm the choice of parameters in numerical model and obtain an insight into which wave forcing frequencies might excite that particular model response.

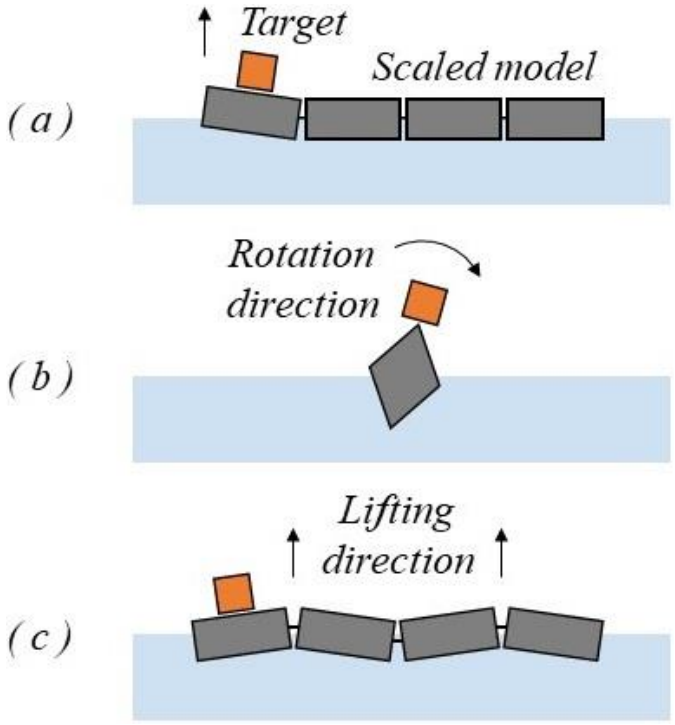

Fig. 13. Schematics of free release tests: *(a)* pitch test;
(b) roll test; *(c)* hobby-horse test.

Table 4.4 contains natural frequencies observed in both physical tests (rescaled to full-scale values) and numerical simulations. The numerical prediction for pitch natural frequency is 16% higher than in the physical test. There are three possible reasons for such a discrepancy: (1) approximations used for scaling rigidity in physical models (Table 4.1), (2) utilization of the averaged mass distributions in numerical models of longitudinal pipes (Table 4.3), and (3) loss of energy due to radiated waves generated during the manual releases. We attribute this discrepancy to the radiated waves energy loss since there is no mechanism in numerical model that takes it into account, which results in higher numerical pitch natural frequency. Roll and hobby-horse release tests demonstrated good correspondence between physical testing and numerical predictions.

Table 4.4. Full-scale natural frequencies obtained from free release tests in wave tank and numerical simulations. Physical model values are rescaled.

Free release test	**Physical model natural frequency** ***[Hz]***	**Numerical model natural frequency** ***[Hz]***
Pitch	0.58	0.68
Roll	0.42	0.43
Hobby-horse	0.65	0.64

3.2 Single-frequency wave testing: physical experiment and numerical simulations

Both physical and numerical single-frequency wave tests were conducted for two model orientations (inline and sideways) and two values of bridle line pretensions (*2224 N* and *4448 N*). Seven wave frequencies and three different wave heights were investigated; however high frequency large waves could not be achieved due to the wave tank physical limitations. A full list of waves successfully produced by the tank and recalculated to full-scale is presented in Table 4.5. Wave frequencies chosen for the single-frequency tests are in the range from *0.1 Hz* to *0.3 Hz* which spans the range for which there is sufficient wave energy to excite a response from the barrier. As the effect of mooring line pretension did not significantly influence neither heave, pitch/roll nor force RAOs, the results for *4448 N* bridle line pretension are not presented in this paper.

Table 4.5. Single-frequency wave testing parameters investigated in UNH wave maker. The values are recalculated to full-scale.

Wave frequency ***[Hz]***	**0.099**	**0.111**	**0.127**	**0.149**	**0.178**	**0.223**	**0.298**
Wave period ***[s]***	**10.101**	**9.009**	**7.874**	**6.711**	**5.617**	**4.484**	**3.355**
Wave height *[m]*	1, 2, 3	1, 2, 3	1, 2, 3	1, 2, 3	1, 2, 3	1, 2	1

The comparison between heave, pitch/roll and force RAOs obtained from physical tests and numerical simulations is shown in Figs. 4.14-4.16. It can be seen in Fig. 4.14 that all numerical inline heave results demonstrated similar behavior: RAO remains around *1* for the lowest wave frequencies (wave length is 11 times longer than barrier unit length) with the slight increase at about *0.18 Hz* and significant decline at *0.22 Hz* and *0.30 Hz* (wave length is about 2 and 1 barrier unit lengths, respectively). Physical testing results follow the same trend with the exception of the high frequency RAO value for the *2 m* wave. For the sideways model orientation, the observed heave RAOs are mostly in the range of *0.95-1.05*. However, three data points with high values of RAO can be seen for tank tests at the low wave frequencies for *2 m* and *3 m* waves. Subsequent investigation of the test records conducted after the tests were completed showed that the issue was caused by the shift in camera placement as the barrier clearly contoured waves with the RAO around *1*. It was decided to include the initial tests results in the figure for consistency.

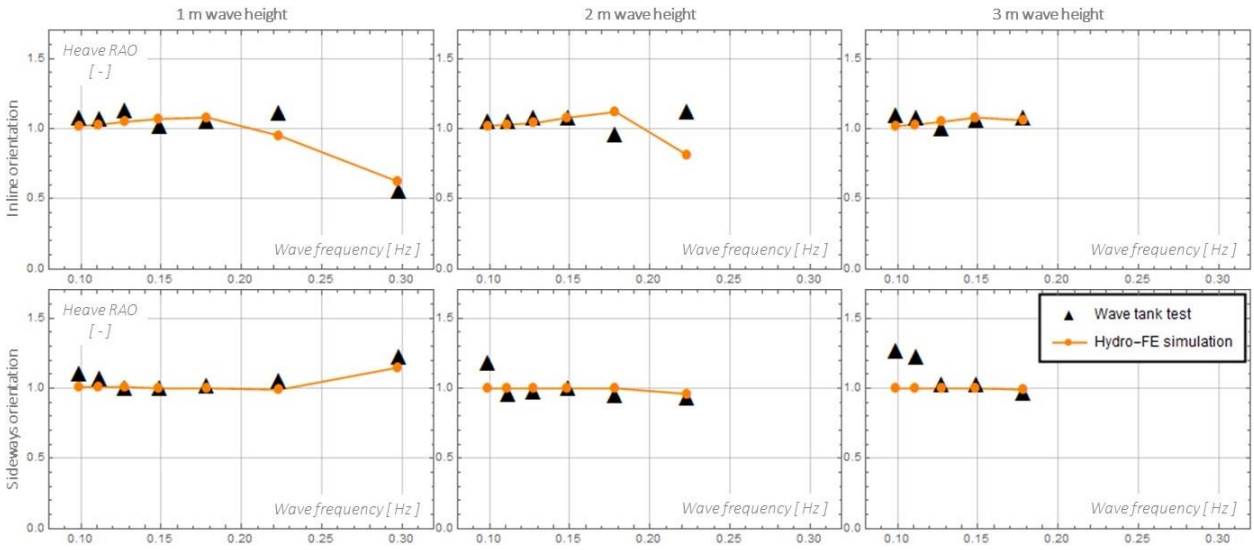

Fig. 4.14. Full-scale heave RAO observed in physical tests and numerical simulations. The upper row of plots represents inline model orientation while the lower one represents sideways orientation. First, second and third columns correspond to *1 m*, *2 m* and *3 m* waves, respectively.

Pitch and roll RAOs showed good agreement between physical and numerical values for both inline and sideways model orientations (Fig. 4.15). The inline (pitch) RAOs reach their peak of about *0.10-0.13 rad/m* and then decay as wave length approaches 1-2 barrier unit lengths. The pitch RAO peaks, however, are not due to a match of driving frequency to natural frequency since the pitch natural frequency is at least double the frequencies at the pitch RAO peaks. Note that pitch RAOs reach their maximum for *1 m* and *2 m* waves at different frequencies. We explain this by the increase in the steepness of the wave slope with the increase of wave height resulting in the change of the RAO peak position. The sideways (roll) results follow the pattern of gradual increase in RAOs with wave frequency. The highest inclination angle amplitude registered among all inline tests is *8.5*°, whereas for sideways tests it is less than *15.5*° (Table 4.6).

Heave RAO results show that the barrier behaves as a wave follower with two exceptions of *1 m* and *2 m* inline waves at the highest frequencies, where heave RAO drops down (excluding one physical test). At these wave frequencies and heights, barrier does not fully contour water surface and faces upcoming waves earlier, thus reducing heave and pitch amplitudes (Fig. 4.15). At the same time, roll RAO consistently grows with wave frequency regardless of incident wave height. We attribute this to the wave slope increase with wave frequency while the barrier width being much smaller than wave lengths. Such behavior can result in a somewhat excessive inclination of the structure (Table 4.6) but does not influence its stability. In all of the performed tests, none have resulted in the barrier's flip or impact with an upcoming wave. All abovementioned considerations are supported by observations in the numerical and physical tests.

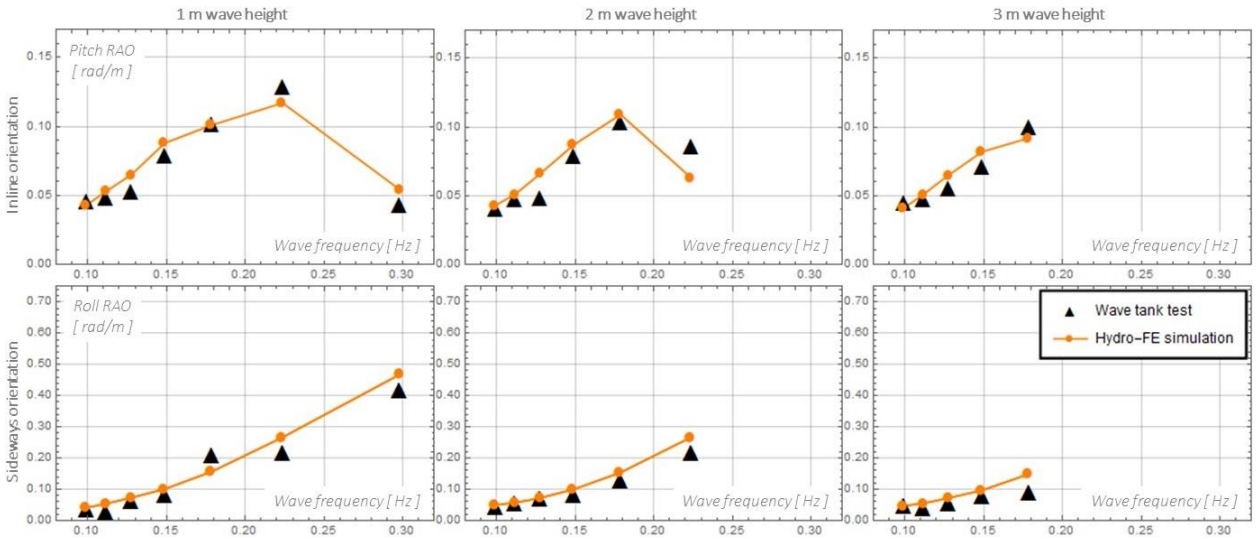

Fig. 4.15. Full-scale pitch and roll RAO observed in physical tests and numerical simulations. The upper row of plots represents inline model orientation while the lower one represents sideways orientation. First, second and third columns correspond to *1 m*, *2 m* and *3 m* waves, respectively.

Table 4.6. The maximum inclination angle amplitude for inline and sideways model orientations among considered wave frequencies.

Frequency *[Hz]*	**0.099**	**0.111**	**0.127**	**0.149**	**0.178**	**0.223**	**0.298**
Inline test	3.60°	4.38°	5.58°	6.87°	8.50°	4.87°	1.58°
Sideways test	3.43°	4.29°	6.01°	8.59°	12.89°	15.47°	13.75°

Fig. 4.16 presents force RAOs obtained from numerical modeling and tank testing. Both numerical and physical test RAOs for the inline model orientation demonstrated a tendency to rise with increase of wave frequency and had a visible plateau from *0.13 Hz* to *0.15 Hz*. The major discrepancy is observed for *1 m* waves where numerically-predicted RAOs are higher than those

from physical tests. In the case of sideways orientation, good correspondence between numerical models and physical tests is observed with the exception of *0.30 Hz 1 m* wave.

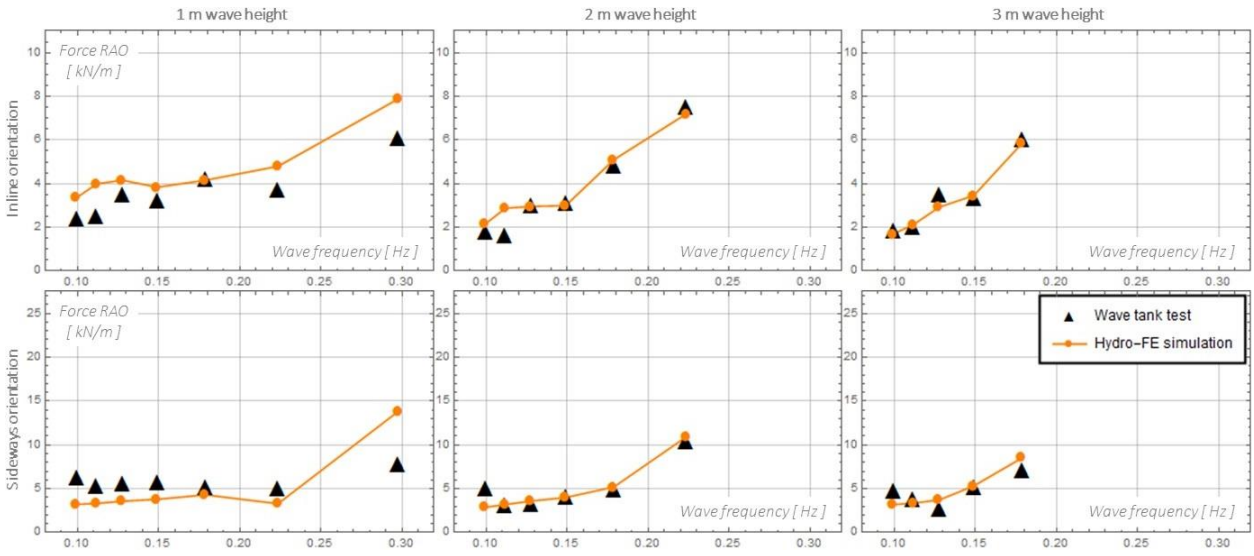

Fig. 4.16. Full-scale force RAO observed in physical tests and numerical simulations. The upper row of plots represents inline model orientation while the lower one represents sideways orientation. First, second and third columns correspond to *1 m*, *2 m* and *3 m* waves respectively.

The force RAO show a pronounced sensitivity to the wave loading frequency: RAO consistently trends upwards with the increase in the wave frequency. We attribute it to the minor mooring line jerking that still occurs due to increasing wave slope and rapid change in the barrier elevation as a result. It is worth noting that the increased RAO at high frequencies is also partially attributed to the deteriorating quality of the measurement signal (increasing signal-to-noise ratio). Even though mooring chain provided reasonable damping to the mooring line, the jerking effect could not be fully eliminated because the chain itself must be heavy enough to secure barrier's position. The maximum tensions of bridle and mooring lines observed in physical and numerical

testing were 42 and 35 times lower than their breaking strength, respectively, as the mooring was intentionally overdesigned in this test field deployment.

3.3 Random waves testing: field study and numerical simulation

In the field study, both the heave response energy density and the wave forcing Bretschneider spectra were obtained for a representative offshore data set recorded from 3:36 am to 4:00 am on April 5, 2018. The NDBC station at Jeffrey's Ledge provided values of the significant wave height (*2.04 m*) and the modal wave frequency (*0.13 Hz*) needed to calculate the Bretschneider wave spectrum. As the energy density spectrum required vertical motion of the barrier as a function of time, the corresponding vertical acceleration data was double integrated over time.

The same approach, in terms of the energy density spectrum, was used for the random waves numerical simulation. However, the Bretschneider wave spectrum considered in the field study was discretized and implemented in *Hydro-FE* as a superposition of 22 single-frequency waves in the frequency range from *0.10 Hz* to *0.30 Hz*. A comparison between incident random waves spectrum, and response spectra from filed study and numerical simulation is shown in Fig. 4.17. Note that the barrier was assumed to be oriented inline with the bridle line pretension of *2224 N*. The correspondence between barrier response spectra is good indicating that *Hydro-FE* captures the essential physics of wave-barrier interaction under random waves conditions in the field. A significant dampening is observed which is attributed to the mooring system configuration: interaction effects of line pretension, shallow angle of the anchor lines and large reserve of "dead weight-chain" portion of the mooring.

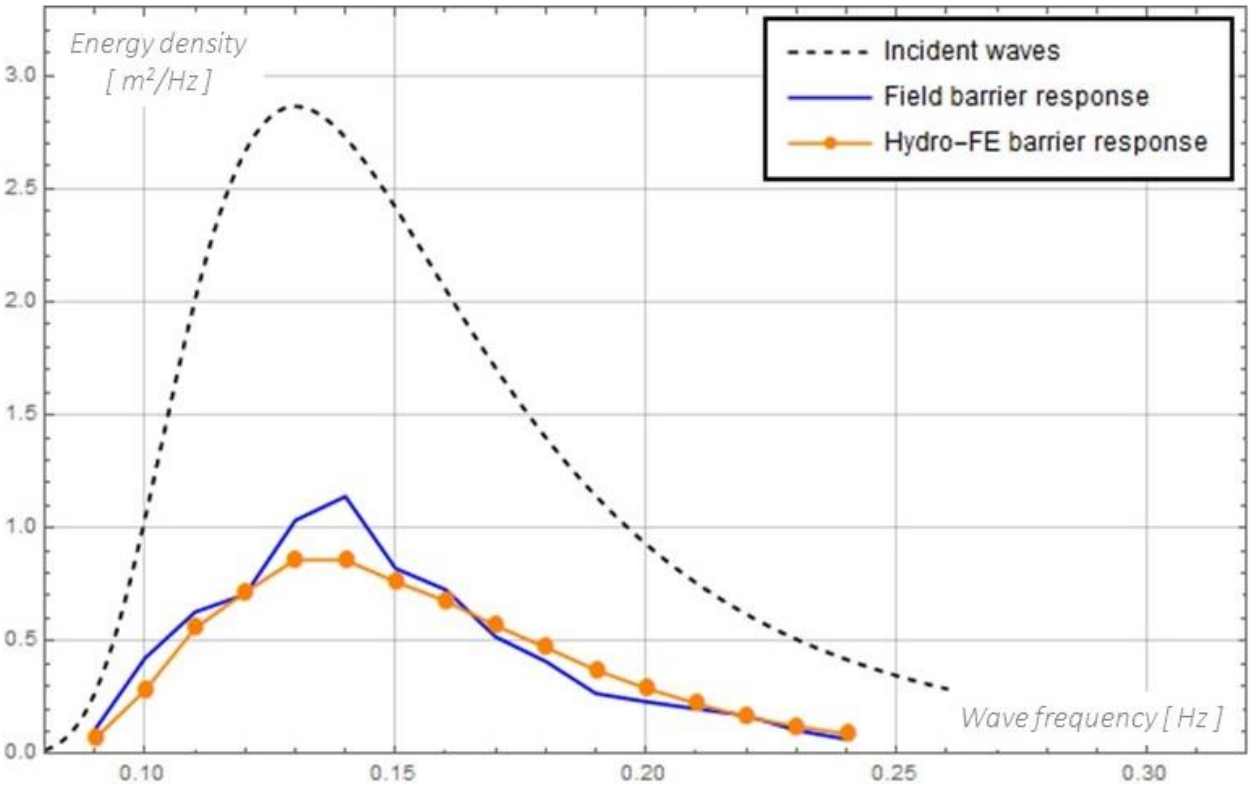

Fig. 4.17. Energy density spectra of random waves and barrier responses in field study and *Hydro-FE* simulation. Random waves significant wave height is *2.04 m* and modal wave frequency is *0.13 Hz*.

The numerical simulations and inspections of the barrier conducted during and after deployment were used to compare its performance with the design requirements. The data showed that (1) the designed hydrostatic and hydrodynamic stability of the barrier was proven to be adequate; (2) the design choice of reducing compliance variations between the structural components (pipe versus hinges) was proven to be well balanced and performed within the operational bounds; (3) the chosen level of barrier pretension provided a good balance between minimizing the barrier surface movement ("watch circle") and alleviating end effects (snapping and oversubmerging); (4) the designed ratio of buoyancy and ballast delivered a good balance of wave following and dampening. Overall system was designed for *10 m* significant wave height

with the period of *12 s* and has demonstrated robust performance in the operational and storm field conditions.

4. Conclusions

This paper presents a comprehensive approach to predicting and evaluating the seaworthiness of floating protective barriers and their mooring systems for deployment in high-energy offshore environments. Good correspondence between the Froude-scaled physical models, numerical simulation results and field test data has been observed.

Numerical models built in the *Hydro-FE* finite element analysis software demonstrated their ability to reproduce most of the results observed in physical testing (with the exception of three outlier data points) and full-scale field data. Based on the modeling effort, it is recommended that mechanical and inertial contribution of small structural components of the barriers is included in the larger structural elements by assigning equivalent effective values to their density, geometric parameters and stiffness.

Successful utilization of the scaled physical models included selection of some approximate values for diameter and weight of several components due to unavailability of exactly scaled parts. The biggest challenge was implementation of the mooring system in the case of sideways tests when the direction of wave propagation was perpendicular to the barrier and the width of the tank prevented exact modeling. This challenge was overcome by a specially-built mooring arrangement utilizing smooth, vertical directional cylinders to redirect the mooring bridle along the length of the tank.

Field tests demonstrated seaworthiness and robustness of the *Triton* floating barrier developed by HALO Maritime Defense Systems and provided an abundant data to develop the best deployment and inspection practices and to evaluate performance of individual barrier components, and overall system stability. The studies allowed successful validating of the numerical model and engineering approach using physical model and field data. The approach was proven to provide a good predictive capability for designing and optimizing floating barrier systems.

Appendix A

Table A.1. Fair weather maximum values of mooring tension T, horizontal displacement d_x, velocity v, acceleration a and its vertical projection a_z, and projections of relative velocity v_{rx}, v_{rz}. Mooring tension is the maximum predicted near the fixed anchors. Displacement, velocity and acceleration are maximum values predicted for droppers. The x-direction is in the direction of wave and current, and the z-direction is upwards.

Yellow dropper	$T[kN]$	$d_x[m]$	$v[m/s]$	$v_{rx}[m/s]$	$v_{rz}[m/s]$	$a[m/s^2]$	$a_z[m/s^2]$
2-point mooring	2.49	7.16	0.07	0.17	0.06	0.11	0.05
4-point mooring	1.85	2.73	0.07	0.18	0.04	0.12	0.03
4-point mooring [W]	2.09	2.48	0.06	0.17	0.02	0.10	0.02
4-point mooring [VL]	1.62	1.95	0.07	0.19	0.04	0.13	0.07

Blue dropper	$T[kN]$	$d_x[m]$	$v[m/s]$	$v_{rx}[m/s]$	$v_{rz}[m/s]$	$a[m/s^2]$	$a_z[m/s^2]$
2-point mooring	2.57	6.95	0.06	0.17	0.02	0.10	0.04
4-point mooring	1.89	2.65	0.07	0.17	0.04	0.12	0.03
4-point mooring [W]	2.14	2.41	0.06	0.17	0.02	0.10	0.02
4-point mooring [VL]	1.60	2.18	0.06	0.18	0.01	0.10	0.06

Green dropper	$T[kN]$	$d_x[m]$	$v[m/s]$	$v_{rx}[m/s]$	$v_{rz}[m/s]$	$a\ [m/s^2]$	$a_z[m/s^2]$
2-point mooring	3.95	8.42	0.05	0.17	0.04	0.08	0.02
4-point mooring	3.08	3.38	0.05	0.17	0.03	0.09	0.01
4-point mooring [W]	3.30	3.18	0.06	0.18	0.02	0.10	0.01
4-point mooring [VL]	2.77	2.61	0.08	0.17	0.06	0.12	0.05

Table A.2. Storm conditions maximum values of mooring tension T, horizontal displacement d_x, velocity v, acceleration a and its vertical projection a_z, and projections of relative velocity v_{rx}, v_{rz}. Mooring tension is the maximum predicted near the fixed anchors. Displacement, velocity and acceleration are maximum values predicted for droppers. The x-direction is in the direction of wave and current, and the z-direction is upwards.

Yellow dropper	$T\,[kN]$	$d_x[m]$	$v[m/s]$	$v_{rx}[m/s]$	$v_{rz}[m/s]$	$a[m/s^2]$	$a_z[m/s^2]$
2-point mooring	3.92	18.16	1.36	0.40	0.46	0.95	0.95
4-point mooring	4.08	9.75	1.45	0.49	0.42	1.03	0.94
4-point mooring [W]	3.35	8.67	1.26	0.42	0.57	0.92	0.63
4-point mooring [VL]	3.00	6.51	1.41	0.51	0.82	1.39	1.07

Blue dropper	$T[kN]$	$d_x[m]$	$v[m/s]$	$v_{rx}[m/s]$	$v_{rz}[m/s]$	$a[m/s^2]$	$a_z[m/s^2]$
2-point mooring	3.65	17.87	1.33	0.37	0.73	0.92	0.78
4-point mooring	3.71	9.60	1.39	0.44	0.50	1.01	0.83
4-point mooring [W]	3.35	8.50	1.22	0.39	0.61	0.91	0.59
4-point Mooring [VL]	2.89	6.83	1.38	0.47	0.83	1.12	0.98

Green dropper	$T[kN]$	$d_x[m]$	$v[m/s]$	$v_{rx}[m/s]$	$v_{rz}[m/s]$	$a[m/s^2]$	$a_z[m/s^2]$
2-point mooring	7.84	22.87	1.32	0.52	0.29	0.99	0.81
4-point mooring	8.23	13.75	1.45	0.56	0.26	1.11	0.93
4-point mooring [W]	6.32	14.12	1.27	0.56	0.44	0.95	0.64
4-point mooring [VL]	5.18	9.91	1.48	0.66	0.89	1.29	1.15

References

Akpinar, A., van Vledder, G.P., Kömürcü, M.I., Özger, M., 2012. Evaluation of the numerical wave model (SWAN) for wave simulation in the Black Sea. Cont. Shelf Res. 50–51, 80–99.

Akpınar, A., Bingölbali, B., Van Vledder, G.P., 2016. Wind and wave characteristics in the Black Sea based on the SWAN wave model forced with the CFSR winds. Ocean Eng. 126, 276–298.

Asche, F., Cojocaru, A.L., Roth, B., 2018. The development of large scale aquaculture production: A comparison of the supply chains for chicken and salmon. Aquaculture 493, 446–455.

Augyte, S., Yarish, C., Redmond, S., Kim, J.K., 2017. Cultivation of a morphologically distinct strain of the sugar kelp, Saccharina latissima forma angustissima, from coastal Maine, USA, with implications for ecosystem services. J. Appl. Phycol. 29, 1967–1976.

Bansal, R.K., 2010. A textbook of strength of materials. Laxmi Publications.

Berstad, A.J., Heimstad, L.F., 2019. Analysis of Flexible Net Structures in Marine Environment. Marine 2019.

Berstad, A.J., Walaunet, J., Heimstad, L.F., 2012. Loads From Currents and Waves on Net Structures. 31st International Conference on Ocean, Offshore and Arctic Engineering, p. 10.

Bi, C.W., Chen, Q.P., Zhao, Y.P., Su, H., Wang, X.Y., 2020. Experimental investigation on the hydrodynamic performance of plane nets fouled by hydroids in waves. Ocean Eng. 213, 107839.

Bishop, J., 2013. Security barrier system. EP2627964B1.

Brown, L., Mac Berthouex, P., 2002. Statistics for Environmental Engineers, Second Edition, Statistics for Environmental Engineers, Second Edition.

Buck, B.H., 2007. Experimental trials on the feasibility of offshore seed production of the mussel Mytilus edulis in the German Bight: Installation, technical requirements and environmental conditions. Helgol. Mar. Res. 61, 87–101.

Buck, B.H., Buchholz, C.M., 2005. Response of offshore cultivated Laminaria saccharina to hydrodynamic forcing in the North Sea. Aquaculture 250, 674–691.

Buck, B.H., Langan, R., 2017. Aquaculture Perspective of Multi-Use Sites in the Open Ocean.

Carafano, J.J., 2007. Small Boats , Big Worries : Thwarting Terrorist Attacks from the Sea. Backgrounder 8.

Chen, C., Beardsley, R.C., Cowles, G., Qi, J., Lai, Z., Gao, G., Stuebe, D., Xu, Q., Xue, P., Ge, J., Ji, R., Hu, S., Tian, R., Huang, H., Wu, L., Lin, H., 2012. An Unstructured-Grid, Finite-Volume Community Ocean Model: FVCOM user manual. Sea Grant College Program, Massachusetts Institute of Technology.

Chen, C., Gao, G., Qi, J., Proshutinsky, A., Beardsley, R.C., Kowalik, Z., Lin, H., Cowles, G., 2009. A new high-resolution unstructured grid finite volume Arctic Ocean model (AO-FVCOM): An application for tidal studies. J. Geophys. Res. 114, 1–20.

Chen, C., Huang, H., Beardsley, R.C., Xu, Q., Limeburner, R., Cowles, G.W., Sun, Y., Qi, J., Lin, H., 2011. Tidal dynamics in the Gulf of Maine and New England Shelf: An application of FVCOM. J. Geophys. Res. Ocean. 116, 1–14.

Cheney, D., Langan, R., Heasman, K., Friedman, B., Davis, J., 2010. Shellfish Culture in the Open Ocean: Lessons Learned for Offshore Expansion. Mar. Technol. Soc. J. 44, 55–67.

Choo, Y.-I., Casarella, M.J., 1971. Hydrodynamic Resistance of Towed Cables. J. Hydronautics.

Cranford, P.J., Duarte, P., Robinson, S.M.C., Fernández-Reiriz, M.J., Labarta, U., 2014. Suspended particulate matter depletion and flow modification inside mussel (Mytilus galloprovincialis) culture rafts in the Ría de Betanzos, Spain. J. Exp. Mar. Bio. Ecol.

Danioux, C., Bompais, X., Paquotte, P., Loste, C., 2000. Offshore mollusc production in the Mediterranean basin. Mediterr. offshore Maric. 140, 115–140.

Dean, R.G., Dalrymple, R.A., 1991. Water wave mechanics for engineers and scientists, Engineering.

DeCew, J., Fredriksson, D.W., Bugrov, L., Swift, M.R., Eroshkin, O., Celikkol, B., 2005. A case study of a modified gravity type cage and mooring system using numerical and physical models. IEEE J. Ocean. Eng. 30, 47–58.

DeCew, J., Rowell, M., 2013. Hydrodynamic Analysis of the HMDS Guardian System and Sentry Buoy. Technical report.

DeCew, J., Tsukrov, I., Risso, A., Swift, M.R., Celikkol, B., 2010. Modeling of dynamic behavior of a single-point moored submersible fish cage under currents. Aquac. Eng. 43, 38–45.

Dewhurst, T., 2016. Dynamics of a Submersible Mussel Raft, PhD Thesis. Univ. New Hampsh.

Dewhurst, T., Hallowell, S.T., Newell, C., 2019. Dynamics of an array of submersible mussel rafts in waves and current. Proc. Int. Conf. Offshore Mech. Arct. Eng. - OMAE 7A-2019.

Dohan, K., Maximenko, N., 2010. Monitoring ocean currents with satellite sensors. Oceanography 23, 94–103.

Drapeau, A., Comeau, L.A., Landry, T., Stryhn, H., Davidson, J., 2006. Association between longline design and mussel productivity in Prince Edward Island, Canada. Aquaculture.

Fairbanks, L., 2016. Moving mussels offshore? Perceptions of offshore aquaculture policy and expansion in New England. Ocean Coast. Manag. 130, 1–12.

Fredriksson, D.W., DeCew, J.C., Tsukrov, I., Swift, M.R., Irish, J.D., 2007. Development of large fish farm numerical modeling techniques with in situ mooring tension comparisons. Aquac. Eng. 36, 137–148.

Fredriksson, D.W., Dewhurst, T., Drach, A., Beaver, W., St. Gelais, A.T., Johndrow, K., Costa-Pierce, B.A., 2020. Hydrodynamic characteristics of a full-scale kelp model for aquaculture applications. Aquac. Eng. 90, 102086.

Fredriksson, D.W., Steppe, C.N., Wallendorf, L., Sweeney, S., Kriebel, D., 2010. Biological and hydrodynamic design considerations for vertically oriented oyster grow out structures. Aquac. Eng. 42, 57–69.

Fredriksson, D.W., Swift, M.R., Irish, J.D., Tsukrov, I., Celikkol, B., 2003. Fish cage and mooring system dynamics using physical and numerical models with field measurements. Aquac. Eng.

Fredriksson, D.W., Swift, M.R., Muller, E., Baldwin, K., Celikkol, B., 2000. Open ocean aquaculture engineering: System design and physical modeling. Mar. Technol. Soc. J.

Gagnon, M., Bergeron, P., 2017. Observations of the loading and motion of a submerged mussel longline at an open ocean site. Aquac. Eng. 78, 114–129.

Gansel, L.C., Plew, D.R., Endresen, P.C., Olsen, A.I., Misimi, E., Guenther, J., Jensen, Ø., 2015. Drag of Clean and Fouled Net Panels--Measurements and Parameterization of Fouling. PLoS One 10, e0131051.

Gentry, R.R., Lester, S.E., Kappel, C. V., White, C., Bell, T.W., Stevens, J., Gaines, S.D., 2017. Offshore aquaculture: Spatial planning principles for sustainable development. Ecol. Evol. 7, 733–743.

Goodfellow, I., Bengio, Y., Courville, A., 2016. Deep learning, MIT press.

Goodman, T., Breslin, J., 1976. Statics and dynamics of anchoring cables in waves. J. Hydronautics 10, 113–120.

Gosz, M., Kestler, K., Swift, M.R., Celikkol, B., 1996. Finite Element Modeling of Submerged Aquaculture Net-Pen Systems. Open Ocean Aquac. Proc. Int. Conf 8–10.

Greenberg, M., Chalk, P., Willis, H., Khilko, I., Ortiz, D., 2006. Maritime Terrorism: Risk and Liability, Maritime Terrorism: Risk and Liability. Rand Corporation.

Henry, P.Y.T., 2014. Bending properties of a macroalga: Adaptation of Peirce's cantilever test for in situ measurements of Laminaria digitata (Laminariaceae). Am. J. Bot. 101, 1050–1055.

Hill, B.P., 2009. Maritime terrorism and the small boat attack threat to the United States: a proposed response. Naval Postgraduate School, Monterey, California.

Hoerner, S., 1965. Fluid-Dynamic Drag. Publ. by author.

Holmström, K., 2008. An adaptive radial basis algorithm (ARBF) for expensive black-box global optimization. J. Glob. Optim. 41, 447–464.

Huang, C.C., Tang, H.J., Liu, J.Y., 2006. Dynamical analysis of net cage structures for marine aquaculture: Numerical simulation and model testing. Aquac. Eng.

Huang, H., Chen, C., Cowles, G.W., Winant, C.D., Beardsley, R.C., Hedstrom, K.S., Haidvogel, D.B., 2008. FVCOM validation experiments: Comparisons with ROMS for three idealized barotropic test problems. J. Geophys. Res. Ocean. 113, 1–14.

Hutter, F., Lücke, J., Schmidt-Thieme, L., 2015. Beyond Manual Tuning of Hyperparameters. KI - Kunstl. Intelligenz 29, 329–337.

Jiang, H., Liu, Z. and Gao, K., 2017. Numerical simulation on rock fragmentation by discontinuous water-jet using coupled SPH/FEA method. Powder Technology, 312, pp.248-259.

Jones, S., 2006. Maritime security: a practical guide. Nautical Institute.

Kalinski, M.E., Bryson, L.S., Krumenacher, A.D., Phillips, B.T., Ethington, Z., Webster, B.T., 2014. Existing technologies for deterring and defeating waterside attack of dams. Int. J. Crit. Infrastructures.

Karayücel, S., Çelik, M.Y., Karayücel, I., Öztürk, R., Eyüboğlu, B., 2015. Effects of stocking density on survival, growth and biochemical composition of cultured mussels (Mytilus galloprovincialis, Lamarck 1819) from an offshore submerged longline system. Aquac. Res.

Kiciński, R., Jurczak, W., Jabłońska, M., 2019. Technical Aspect concerning Vessels Halt Safety upon Terrorist Hazard. J. Konbin.

Kim, J.K., Kraemer, G.P., Yarish, C., 2015. Use of sugar kelp aquaculture in Long Island Sound and the Bronx River Estuary for nutrient extraction. Mar. Ecol. Prog. Ser. 531, 155–166.

Klebert, P., Lader, P., Gansel, L., Oppedal, F., 2013. Hydrodynamic interactions on net panel and aquaculture fish cages: A review. Ocean Eng. 58, 260–274.

Klebert, P., Patursson, Ø., Endresen, P.C., Rundtop, P., Birkevold, J., Rasmussen, H.W., 2015. Three-dimensional deformation of a large circular flexible sea cage in high currents: Field experiment and modeling. Ocean Eng. 104, 511–520.

Knysh, A., Coyle, J., Decew, J., Drach, A., Swift, M.R., Tsukrov, I., 2021. Floating protective barriers : Evaluation of seaworthiness through physical testing , numerical simulations and field deployment. Ocean Eng. 108707.

Knysh, A., Drach, A., Fredriksson, D., Dewhurst, T., Tsukrov, I., 2022. Methodology for multidimensional approximation of current velocity fields around offshore aquaculture installations. Aquac. Eng. 99, 102284.

Knysh, A., Tsukrov, I., Chambers, M., Swift, M.R., Sullivan, C., Drach, A., 2020. Numerical modeling of submerged mussel longlines with protective sleeves. Aquac. Eng.

Kristiansen, T., Faltinsen, O.M., 2012. Modelling of current loads on aquaculture net cages. J. Fluids Struct. 34, 218–235.

Krogstad, H.E., 1988. Maximum likelihood estimation of ocean wave spectra from general arrays of wave gauges. Model. Identif. Control.

Kutupoğlu, V., Çakmak, R.E., Akpınar, A., van Vledder, G.P., 2018. Setup and evaluation of a SWAN wind wave model for the Sea of Marmara. Ocean Eng. 165, 450–464.

Lai, Z., Chen, C., Cowles, G.W., Beardsley, R.C., 2010. A nonhydrostatic version of FVCOM: 1. Validation experiments. J. Geophys. Res. Ocean. 115, 1–23.

Landmann, J., Ongsiek, T., Goseberg, N., Heasman, K., Buck, B., Paffenholz, J.-A., Hildebrandt, A., 2019. Physical Modelling of Blue Mussel Dropper Lines for the Development of Surrogates and Hydrodynamic Coefficients. J. Mar. Sci. Eng.

Langan, R., 2013. Mussel Culture, Open Ocean Innovations. Sustain. Food Prod. 1229–1239.

Lauzon-Guay, J.S., Barbeau, M.A., Watmough, J., Hamilton, D.J., 2006. Model for growth and survival of mussels Mytilus edulis reared in Prince Edward Island, Canada. Mar. Ecol. Prog. Ser.

Lee, C.W., Kim, Y.B., Lee, G.H., Choe, M.Y., Lee, M.K., Koo, K.Y., 2008. Dynamic simulation of a fish cage system subjected to currents and waves. Ocean Eng.

Lee, C.W., Lee, J., Park, S., 2015. Dynamic behavior and deformation analysis of the fish cage system using mass-spring model. China Ocean Eng.

Lewis, M., Neill, S.P., Robins, P., Hashemi, M.R., Ward, S., 2017. Characteristics of the velocity profile at tidal-stream energy sites. Renew. Energy 114, 258–272.

Li, Y.C., Zhao, Y.P., Gui, F.K., Teng, B., 2006. Numerical simulation of the hydrodynamic behaviour of submerged plane nets in current. Ocean Eng.

Liang, B., Gao, H., Shao, Z., 2019. Characteristics of global waves based on the third-generation wave model SWAN. Mar. Struct. 64, 35–53.

Lin, J., Li, C., Zhang, S., 2016. Hydrodynamic effect of a large offshore mussel suspended aquaculture farm. Aquaculture.

López, J., Hurtado, C.F., Gómez, A., Zamora, V., Queirolo, D., Gutiérrez, A., Ciencias, E. De, Ciencias, F. De, Universidad, P., Valparaíso, C. De, 2017. Stress analysis of a submersible longline culture system through dynamic simulation. Lat. Am. J. Aquat. Res. 45, 25–32.

Majdisova, Z., Skala, V., 2017. Radial basis function approximations: comparison and applications. Appl. Math. Model. 51, 728–743.

Moe-Føre, H., Endresen, P.C., Aarsæther, K.G., Jensen, J., Føre, M., Kristiansen, D., Fredheim, A., Lader, P., Reite, K.J., 2015. Structural analysis of aquaculture nets: Comparison and validation of different numerical modeling approaches. J. Offshore Mech. Arct. Eng.

Morison, J.R., Johnson, J.W., Schaaf, S.A., 1950. The Force Exerted by Surface Waves on Piles. J. Pet. Technol. 2, 149–154.

Nguyen, T.X., Winger, P.D., 2016. Numerical Modeling - A Comparison of Different Methods for Simulating Bottom Trawls. Fish. Technol. 53, 9–29.

Nixon, L., Slaughter, S., Taylor, R., Seelig, W., 2005. Near shore port security barrier. US6843197B1.

Nixon, L., Slaughter, S., Taylor, R., Seelig, W., 2004. Port security barrier system. US6681709B1.

Osienski, M., DeCew, J., Sherwin, T., Rines, E., 2017. Open water marine barrier systems. WO2018057842A1.

Pedersen, T., Nylund, S., 2004. Wave height measurements using acoustic surface tracking. USA-Baltic Int. Symp. 1234–1241.

Pedersen, T., Siegel, E., 2008. Wave measurements from a subsurface buoy. Sea Tech 42, 17–20.

Perl, R., O'Rourke, R., 2001. Terrorist Attack on USS Cole: Background and Issues for Congress, Congressional Research Service.

Plew, D.R., 2005. The Hydrodynamic Effects of Long-line Mussel Farms. Univ. Canterbury 356p.

Plew, D.R., Enright, M.P., Nokes, R.I., Dumas, J.K., 2009. Effect of mussel bio-pumping on the drag on and flow around a mussel crop rope. Aquac. Eng. 40, 55–61.

Plew, D.R., Stevens, C.L., Spigel, R.H., Hartstein, N.D., 2005. Hydrodynamic implications of large offshore mussel farms. IEEE J. Ocean. Eng. 30, 95–108.

Pribadi, A.B.K., Donatini, L., Lataire, E., 2019. Numerical modelling of a mussel line system by means of lumped-mass approach. J. Mar. Sci. Eng. 7.

Qi, J., Chen, C., Beardsley, R.C., Perrie, W., Cowles, G.W., Lai, Z., 2009. An unstructured-grid finite-volume surface wave model (FVCOM-SWAVE): Implementation, validations and applications. Ocean Model. 28, 153–166.

Raman-Nair, W., Colbourne, B., 2003. Dynamics of a mussel longline system. Aquac. Eng. 27, 191–212.

Raman-Nair, W., Colbourne, B., Gagnon, M., Bergeron, P., 2008. Numerical model of a mussel longline system: Coupled dynamics. Ocean Eng. 35, 1372–1380.

Reite, K.-J., Føre, M., Aarsæther, K.G., Jensen, J., Rundtop, P., Kyllingstad, L.T., Endresen, P.C., Kristiansen, D., Johansen, V., Fredheim, A., 2014. FHSIM — Time Domain Simulation of Marine Systems, in: Volume 8A: Ocean Engineering. American Society of Mechanical Engineers.

Rominger, J.T., Nepf, H.M., 2014. Effects of blade flexural rigidity on drag force and mass transfer rates in model blades. Limnol. Oceanogr. 59, 2028–2041.

Rueda-Bayona, J.G., Guzmán, A., Silva, R., 2020. Genetic algorithms to determine JONSWAP spectra parameters. Ocean Dyn. 70, 561–571.

Sethuraman, L., Venugopal, V., 2013. Hydrodynamic response of a stepped-spar floating wind turbine: Numerical modelling and tank testing. Renew. Energy.

Siegel, E., 2007. New methods for subsurface wave measurements at offshore locations. Ocean News Tech 13, 2–3.

Siegel, E., Pedersen, T., Maatje, J., 2006. Real-Time Directional Wave Measurements. Sea Tech 47, 10–14.

Smith, T.M., Livezey, R.E., Shen, S.S., 1998. An Improved Method for Analyzing Sparse and Irregularly Distributed SST Data on a Regular Grid: The Tropical Pacific Ocean. J. Clim. 11, 1717–1729.

Stevens, C., Plew, D., Hartstein, N., Fredriksson, D., 2008. The physics of open-water shellfish aquaculture. Aquac. Eng. 38, 145–160.

Stevens, C.L., Plew, D.R., Smith, M.J., Fredriksson, D.W., 2007. Hydrodynamic Forcing of Long-Line Mussel Farms: Observations. J. Waterw. Port, Coastal, Ocean Eng.

St-Gelais, A.T., Fredriksson, D.W., Dewhurst, T., Miller-Hope, Z.S., Costa-Pierce, B.A., Johndrow, K., 2022. Engineering a low-cost kelp aquaculture system for community-scale seaweed farming at nearshore exposed sites via user-focused design process. Front. Sustain. Food Syst 6.

Swift, M.R., Coyle, J.S., Baldwin, K., Celikkol, B., Tsukrov, I., 2019. Environmental testing of the HALO Triton barrier at the University of New Hampshire offshore test site. Newton.

Swift, M.R., Fredriksson, D.W., Unrein, A., Fullerton, B., Patursson, O., Baldwin, K., 2006. Drag force acting on biofouled net panels. Aquac. Eng. 35, 292–299.

Thierry, N.N.B., Tang, H., Xu, L., Hu, F., 2019. Effect of mesh size, twine material and trawl gear accessories on the bottom trawls hydrodynamic performance. Int. J. Fish. Aquat. Res. 4, 01–09.

Tsarau, A., Kristiansen, D., 2019. Application of FhSim for the analysis of environmental loads on a complete fish-farm system, in: 8th International Conference on Computational Methods in Marine Engineering, MARINE 2019. International Center for Numerical Methods in Engineering, pp. 271–284.

Tsukrov, I., Drach, A., DeCew, J., Swift, M.R., Celikkol, B., Baldwin, K.C., 2011. Experimental Studies and Numerical Modeling of Copper Nets in Marine Environment.

Tsukrov, I., Eroshkin, O., Fredriksson, D., Swift, M.R., Celikkol, B., 2003. Finite element modeling of net panels using a consistent net element. Ocean Eng. 30, 251–270.

Tsukrov, I.I., Ozbay, M., Swift, M.R., Celikkol, B., Fredriksson, D.W., Baldwin, K., 2000. Open Ocean Aquaculture Engineering: Numerical Modeling. Mar. Technol. Soc. J. 34, 29–40.

Vettori, D., Nikora, V., 2017. Morphological and mechanical properties of blades of Saccharina latissima. Estuar. Coast. Shelf Sci. 196, 1–9.

Wang, X.X., Swift, M.R., Dewhurst, T., Tsukrov, I., Celikkol, B., Newell, C., 2015. Dynamics of submersible mussel rafts in waves and current. China Ocean Eng. 29, 431–444.

Wendland, H., 2005. Scattered data approximation. World Scientific.

Winthereig-Rasmussen, H., Simonsen, K., Patursson, Ø., 2016. Flow through fish farming sea cages: Comparing computational fluid dynamics simulations with scaled and full-scale experimental data. Ocean Eng. 124, 21–31.

Xu, Z., Qin, H., Li, P., Liu, R., 2020. Computational fluid dynamics approaches to drag and wake of a long-line mussel dropper under tidal current. Sci. Prog. 103, 1–25.

Zhan, J.M., Jia, X.P., Li, Y.S., Sun, M.G., Guo, G.X., Hu, Y.Z., 2006. Analytical and experimental investigation of drag on nets of fish cages. Aquac. Eng. 35, 91–101.

Zhao, Y., Yang, H., Bi, C., Chen, Q., Dong, G., Cui, Y., 2019. Hydrodynamic responses of longline aquaculture facility with lantern nets in waves. Aquac. Eng. 86, 101996.

Zhao, Y.P., Li, Y.C., Dong, G.H., Gui, F.K., Teng, B., 2007. A numerical study on dynamic properties of the gravity cage in combined wave-current flow. Ocean Eng.

Zhao, Y.P., Wang, X.X., Decew, J., Tsukrov, I., Bai, X.D., Bi, C.W., 2015. Comparative study of two approaches to model the offshore fish cages. China Ocean Eng. 29, 459–472.